الجمهورية الجزائرية الديمقراطية الشعبية
Republique Algerienne Democratique et Populaire
وزارة التعليم العالي و البحث العلمي
Ministere de l’Enseignement Superieur et de la Recherche Scientifique
جامـعة الشهيد حمة لخضر –الوادي
Universite Echahid Hamma Lakhdar d’El-Oued

Faculté de la Technologie كلية التكنولوجيا

Département de Génie Mécanique قسم الهندسة الميكانيكية

Ref : ……… المرجع: ……….

En Vue de l’Obtention du Diplôme de DOCTORAT LMD

Filière : Génie mécanique
Option : Energétique

Thème:

Procédé de dépôt de matériaux nanostructurales à l’aide d’énergie solaire

Présenté par :

Mr. Bedreddine MAAOUI

Soutenue: 25/11/2021.
Devant le Jury Composé de:

Mr : Boubaker BEN HAOUA	**Professeur**	**UHL El-Oued**	**Président**
Mr : Said LAKEL	**Professeur**	**UMK Biskra**	**Examinateur**
Mr: Mohamed Sadek MAHBOUB	**Professeur**	**UHL El-Oued**	**Examinateur**
Mr: Azzeddine BEGGAS	**MCA**	**UHL El-Oued**	**Examinateur**
Mr : Yacine AOUN	**MCA**	**UHL El-Oued**	**Encadreur**
Mr : Said BEN RAMACHE	**Professeur**	**UMK Biskra**	**Co- Encadreur**

Année Universitaire: 2020/2021

Acknowledgments

Firstly, many thanks to **ALLAH** for his grace and help, who let me finishing my thesis research.

Secondly, I would like to express my sincere gratitude to my advisor **Dr. Yacine AOUN** for the continuous support of my thesis study and research, for his patience, motivation, enthusiasm, and immense knowledge. His guidance helped me in all the time of research and writing of this thesis.

A big thank you to **Pr. Said BENRAMACHE** , Co-Supervisor of my thesis, Professor at Mohamed Khider University of Biskra for his support and advice, encouraged me, and helped me to carry out this work.

I address my thanks to **Pr. Boubaker BEN HAOUA**, of El-Oued University, **Pr. Said LAKEL**, of Biskra University, **Pr. Mohamed Sadek MAHBOUB** , of El-Oued University, and **Dr. Azzeddine BEGGAS** of El-Oued University, for their acceptance to judge this modest work.

I would like to extend my special thanks to **Pr. Boubaker BEN HAOUA** for his considerable help, and **Dr. Mebrouk GHOUGALI** For helping me especially at the beginning of this research.

Last but not the least, I would like to thank my family: my parents, I cannot forget my wife, my son **YAHYA** and all my friends for their help and advising.

Bedreddine MAAOUI

DEDICATION

I would like to dedicate this work to:

My family

To my friends

Table of content

Chapter I: State Of The Art: Solar Heating and Thin Films

Chapter II: Elaboration Technique and Characterization Methods

Chapter III: Results of ZnO Thin Films

Chapter IV: Results of NiO Thin Films

Chapter V: Results of SnO_2 Thin Films

General Concusion

References

List of tables

List of figures

Abstract

Abstract

In this thesis, solar energy was used to prepare thin films by heating substrate. ZnO, NiO and SnO_2 thin films were elaborated by spray pyrolysis technique and solar heat. ZnO samples were prepared at various substrate temperature, deposition rate and dopant ratio, whereas NiO and SnO_2 layers were fabricated with different precursor concentration and deposition rate, respectively. The structural, optical and electrical proprieties were studied for all samples.

As results for ZnO thin films at different substrate temperature, the XRD patterns showed that the structural of all films is polycrystalline, the crystallite size increased greatly from 9.96 to 15.19 nm by increasing of deposition temperature from 350 to 450 °C. The transmission of films prepared at 350°C exceeded 90%. For the effect of deposition rate, the obtained ZnO thin films are polycrystalline, an increase in the XRD intensity of the peaks has been noted. An average transmission of about 85% in the visible region was observed; whereas the estimated band gap energy decreased from 3.30 to 3.28eV. The resistivity decreased from 1.19 to 0.01(Ω cm). Regarding the effect of dopant, ZnO was doped by nickel (0, 1, 2, 3, and 6 at %), polycrystalline Ni-doped ZnO thin films were indicated. However, α-$Ni(OH)_2$ and β-$Ni(OH)_2$ were observed at 6 and 3 at % Ni, respectively. All thin films have a high optical transmission in the visible region of about 85%. The optical band gap energy increased from 3.26 eV for 0% to 3.34 eV for 1 at %, and further decreased to 3.27 eV for 6 at % Ni. The thin film deposited with 3 at % Ni has the lowest value of Urbach energy of 0.091eV. The electrical conductivity of the Ni-doped ZnO films increased greatly from 0.016 $(\Omega\ cm)^{-1}$ for 0% Ni to 0.042 $(\Omega\ cm)^{-1}$ for 3 at % Ni.

For NiO result of thin films prepared at different concentration (0.05, 0.10 and 0.15 $mol.l^{-1}$). Polycrystalline NiO films with a cubic structure were observed at all sprayed films having as minimum crystallite size of 11.97nm was attained at 0.1 $mol.l^{-1}$ concentration. However, α-Ni $(OH)_2$ was observed at 0.15 $mol.l^{-1}$. The band gap energy varied from 3.54 to 3.76eV with low transmittance. The electrical conductivity of NiO film deposited at 0.15 $mol.l^{-1}$ was 0.169 $(\Omega.cm)^{-1}$.

For SnO_2, the characterization results of elaborated thin films at different deposition rates (5, 10 and 15ml) showed a polycrystalline structure with maximum crystallite size 35.3 nm for 10ml. The transmittance of prepared samples was about 60 % and the optical band gap energy increased from 3.2 eV for 5ml to 3.6 eV for 15ml. The electrical conductivity was increased from 0.01 $(\Omega.cm)^{-1}$ to 0.06 $(\Omega.cm)^{-1}$.

Keywords: spray pyrolysis, solar heating, ZnO, NiO, SnO_2, thin films, Ni doping, NiO concentration

Résumé

Dans cette thèse, l'énergie solaire a été utilisée pour préparer des couches minces par chauffage du substrat. Les couches minces ZnO, NiO et SnO_2 ont été élaborées par spray pyrolyse et de chauffage solaire. Les échantillons de ZnO ont été préparés à diverses températures de substrat, taux de dépôt et rapport de dopage, tandis que les couches NiO et SnO_2 ont été fabriquées avec des concentrations et des taux de dépôt de précurseurs différents, respectivement. Les propriétés structurelles, optiques et électriques ont été étudiées pour tous les échantillons.

Comme résultats pour les films minces ZnO à différentes températures de substrat, les modèles XRD ont montré que la structure de tous les films est polycristalline, la taille de la cristallite a augmenté considérablement de 9,96 à 15,19 nm en augmentant la température de dépôt de 350 à 450 °C. La transmission des films préparés à 350 dépassait 90 %. Pour l'effet du taux de dépôt, les couches minces de ZnO obtenues sont polycristallines, une augmentation de l'intensité XRD des pics a été notée. Une transmission moyenne d'environ 85 % dans la région visible a été observée, tandis que l'énergie estimée de la bande interdite est passée de 3,30 à 3,28 eV. La résistivité est passée de 1,19 à 0,01 (Ω cm). En ce qui concerne l'effet du dopant, le ZnO a été dopé par du nickel (0, 1, 2, 3, et 6 at %), des couches minces polycristallines de ZnO dopé par du Ni ont été indiquées. Cependant, α-$Ni(OH)_2$ et β-$Ni(OH)_2$ ont été observés à 6 et 3 at % Ni, respectivement. Tous les films minces ont une transmission optique élevée dans la région visible d'environ 85%. L'énergie de la bande interdite a augmenté de 3,26 eV pour 0 % à 3,34 eV pour 1 % et a encore diminué à 3,27 eV pour 6 % Ni. La couche mince déposée avec 3 at % Ni a la valeur la plus basse de l'énergie Urbach de 0.091eV. La conductivité électrique des films ZnO dopée par Nickel a considérablement augmenté de 0,016 $(\Omega\ cm)^{-1}$ pour 0 % Ni à 0,042 $(\Omega\ cm)^{-1}$ pour 3 at% Ni.

Pour le résultat des films minces de NiO préparés à différentes concentrations (0,05, 0,10 et 0,15 $mol.l^{-1}$). Des films NiO polycristallins à structure cubique ont été observés sur tous les films pulvérisés, ayant une taille cristalline minimale de 11,97 nm à une concentration de 0,1 $mol.l^{-1}$. Cependant, α-Ni $(OH)_2$ a été observé à 0,15 $mol.l^{-1}$. L'énergie la bande interdite variait de 3,54 à 3,76eV avec une faible transmission. La conductivité électrique du film NiO déposé à 0,15 $mol.l^{-1}$ était de 0,169 $(\Omega.cm)^{-1}$.

Pour le SnO_2, les résultats de caractérisation des couches minces élaborées à différents taux de dépôt (5, 10 et 15ml) ont montré une structure polycristalline avec une taille maximale de cristallite de 35,3 nm pour 10ml. La transmission des échantillons préparés était d'environ 60 % et l'énergie de l'intervalle de la bande interdite est passée de 3,2 eV pour 5 ml à 3,6 eV pour 15 ml. La conductivité électrique a été augmentée de 0,01 $(\Omega.cm)^{-1}$ à 0,06 $(\Omega.cm)^{-1}$.

Mots-clés : spray pyrolyse, chauffage solaire, ZnO, NiO, SnO_2, couche minces, dopage par nickel, concentration de NiO.

ملخص

في هذه الاطروحة، استخدمت الطاقة الشمسية لتسخين المسند من أجل تحضير أغشية رقيقة. أنتجت أغشية من أكاسيد الزنك، النيكل والقصدير بتقنية الانحلال الحراري بالرش والتسخين الشمسي. حضرت عينات أكسيد الزنك بالتغيير في درجات حرارة المسند، كمية التدفق ونسبة التطعيم، في حين شكلت طبقات أكسيد النيكل والقصدير بتراكيز مختلفة للمحلول الابتدائي ومعدل التطعيم متغير، على التوالي. تم دراسة الخصائص البنيوية، البصرية والكهربائية لجميع العينات.

بالنسبة لنتائج أغشية أكسيد الزنك المحضرة عند درجات حرارة مسند مختلفة، أظهرت أنماط حيود الأشعة السينية أن بنية جميع الأغشية متعدد التبلور، زاد حجم البلورات بشكل كبير من 9.96 إلى 15.19 نانومتر بزيادة درجة حرارة المسند من 350 إلى 450 درجة مئوية. شفافية الأفلام عند 350 درجة مئوية تجاوز 90%. أما تأثير كمية التدفق، فإن أغشية أكسيد الزنك المحصل عليها متعددة التبلور، مع زيادة في شدة القمم. متوسط الشفافية بلغ حوالي 85% في المنطقة المرئية، وانخفضت طاقة الفجوة من 3.30 إلى 3.28eV. المقاومة الكهربائية تراجعت من 1.19 إلى 0.01 (اوم. سم). فيما يتعلق بتأثير التطعيم، طعم أكسيد الزنك بواسطة النيكل (0، 1، 2، 3، 6 ذرة %)، وجدت أغشية رقيقة متعددة البلورات، لوحظ $\alpha\text{-Ni (OH)}_2$ و $\beta\text{-Ni (OH)}_2$ عند 6 و 3 ذرة Ni%، على التوالي. جميع الأغشية الرقيقة لها شفافية عالية في المنطقة المرئية قدرت بحوالي 85%. زادت طاقة فجوة النطاق البصري من 3.26eV لـ 0 %إلى eV 3.34 لـ 1 %، وانخفضت أيضًا إلىeV 3.27 لـ 6 ذرة Ni%. الطبقة الرقيقة المودعة عند 3 Ni % لها أقل قيمة لطاقة Urbach تبلغ 0.091 eV. زادت الناقلية الكهربائية لأغشية الزنك المطعمة بالنيكل بشكل كبير من 0.0160 عند 0% إلى 0.0423 (اوم. سم)$^{-1}$عند 3 Ni%. بخصوص نتائج أغشية النيكل الرقيقة المحضرة بتراكيز مختلفة (0.05، 0.10، 0.15 مول / لتر). لوحظت أغشية النيكل متعددة البلورات، ذات بنية مكعبة في جميع الأغشية التي تم رشها مع الحد الأدنى من حجم البلورات 11.97 نانومترعند 0.1 مول / لتر. ومع ذلك، لوحظ $\alpha\text{-Ni (OH)}_2$ عند 0.15 مول / لتر. تراوحت طاقة فجوة النطاق من 3.54 إلى eV 3.76. كانت الناقلية الكهربائية لرقيقة النيكل المودعة عند 0.15 مول / لتر 0.169 (اوم. سم)$^{-1}$.

أظهرت نتائج خصائص أغشية القصدير الرقيقة المنتجة بكميات ترسيب مختلفة (5 , 10 و15 مل)، بنية متعددة البلورات مع أقصى حجم بلوري 35.3 نانومتر عند 10 مل. بلغت نفاذية الضوئية للعينات المحضرة حوالي 60 %، وزادت طاقة فجوة النطاق البصري منeV 3.2 لكمية 5 مل إلىeV 3.6 لكمية 15 مل. زادت الناقلية الكهربائية من 0.01 إلى 0.06 (اوم. سم)$^{-1}$.

الكلمات المفتاحية :الانحلال الحراري بالرش، التسخين الشمسي، أكسيد الزنك، أكسيد النيكل، أكسيد القصدير، شرائح رقيقة، تطعيم بالنيكل، تركيز أكسيد النيكل.

General Introduction

General introduction

Solar energy is obtained by capturing heat and light from the Sun, it is classified among the renewable energies, which can be used directly by humans for lighting (windows, skylights)[1], heating and cooking (solar water heater, solar oven)[2, 3]. Recently is used to produce nanostructured thin films serving as substrates heater [4, 5].

Nowadays, nanomaterials have large area in industrial sector, because of their interesting structural and opto-electrical properties which cannot be found in normal bulk materials. They are widely used in different applications such as solar cells, light emitting diodes (LED), laser diodes and acoustic–optical devices, etc[6, 7].

Among nanostructured three oxides are used in this work, firstly Zinc Oxide (ZnO) which is an inorganic compound used in a number of manufacturing processes. It can be found in rubbers, plastics, ceramics, glass, cement, lubricants, paints, ointments, adhesives, sealants, pigments, foods, and batteries[8]. This oxide, under thin films forms, can be elaborate at temperature above 300°C. The second oxide is Nickel Oxide (NiO) which is an important material for use in device applications such as gas sensors, dye sensitized photocathodes and electrodes in alkaline batteries[9]. Also, it can be deposited at temperature more than 300°C. The third oxide is Tin dioxide (SnO_2) films which have a high transparency and a good electrical conductivity; various other beneficial properties like high reflectivity for infrared light, high mechanical hardness and good environmental stability are evoked by this oxide. The later needs temperature highest than those previous oxides to be prepared as thin film. This needed temperature is more than 400°C.

Nanostructured can be prepared by various physical and chemical methods like reactive evaporation, pulsed laser deposition (PLD), magnetron sputtering technique, sol–gel process, and spray pyrolysis[10]. From these methods, spray deposition technique with solar heating is used in this work to elaborate nanostructured thin films of (ZnO), (NiO), and (SnO_2).

Research aims and objectives

The objective of this thesis is the use of solar energy (solar dish systems) for heating substrates, and deposition of three oxides (ZnO, NiO and SnO_2) at different conditions such as substrate temperature, deposition rate, doping ratio and precursor concentration. In order to achieve the main characteristic properties of prepared thin films, such as structural, optical and electrical characterization. Those properties will be examined using X-ray diffraction (XRD) to investigate structural properties such as the crystalline quality and nature of the layers, grain size, dislocation density, and strain. UV-visible spectrophotometer will be used to analyse the optical characteristics such as the spectrum of the transmittance and the optical gap energy whereas the four probes method will be used to measure the electrical conductivity of the prepared samples.

Structure of the dissertation

This work comprises five chapters:

The first chapter contains a theoretical presentation of the solar energy and solar dish systems and its applications, which among them is the elaboration of thin films. Then, we talk about thin films and its applications, some proprieties of (ZnO, NiO and SnO_2) oxides, as well as brief description of some deposition techniques of thin films.

The second chapter is devoted to the presentation of the technique of deposition per spray pyrolysis and using solar energy as source of heat. Thereafter, we interested in structural, optical and electric methods of characterization used in this work.

The third chapter includes the elaboration and the study of the effect of deposition parameters such as the substrate temperature, the deposition rate, dopant ratio on the physico-chemical and optoelectronics properties of the prepared metallic oxides ZnO thin films.

The fourth chapter undertake the effect of Ni concentration on the structural, optical and electrical properties of NiO samples prepared by spray pyrolysis technique.

The fifth chapter talks about the effect of deposition rate on the structural, optical and electrical properties of SnO_2 samples prepared by spray pyrolysis technique.

In the three chapters, it will be interpreted carefully. The Characterization results of all thin metal oxides prepared using spray pyrolysis and solar heating technology.

Finally, we conclude by summarizing our results and estimating our experimental work

Chapter I

Stat of Art: Solar Heating and Thin Films

I.1 Introduction

The nuclear fusions in the sun produce a vast amount of energy, emitting in all directions a solar energy or a solar radiation. The amount of solar energy reaching the earth is significant, despite the considerable distance between the sun and the earth. At any one time, the earth receives the energy of 180 10^6 GW from the sun[11]. The solar radiation is the primary natural energy source for earth and in a long way. The geographical location of Algeria allows it to hold one of the highest solar potentials in the world which is estimated to be around 13.9 TWh per year. The sunshine exposure of this country is equivalent to 2,500 KWh/m^2 per year. And varies from 4.66 kWh/m^2 per day in the north to 7.26 kWh/m^2 per day in the south[12]. There are lot of ways in which this solar energy can be used to produce electricity, such as photovoltaics and solar thermal systems (solar powered Stirling engine). Other uses of the solar energy include; cooking, water heating, irrigation, water desalination and distillation.

It can also use solar energy in the elaboration of thin films, this latter has wide range of applications such as electronics, optical communications, and biosystems

This chapter provides a generality about solar energy and the uses of this free and green energy, it gives a new insight into nanostructured thin films. It presents a definition and an overview on the application of thin films, basic information about some metal oxides, and brief introduction on the methods of deposition of these nanostructures. Finally, the chapter discusses the method of spray pyrolysis wish use for deposition of thin films.

I.2 The Sun and solar radiation

Our solar system's sun is the only star at its core. The earth, along with the other planets, orbits the sun. Via photosynthesis, all life on earth is support by the energy emitted from the sun in the form of solar radiation; this energy also drives the earth’s climate and weather. The sun is composed of 74% hydrogen, 25% helium[13], and trace quantities of heavier elements. The color of the sun is white, which appears yellow because of atmospheric scattering. The energy generated by the sun is produced by nuclear fusion of hydrogen nuclei to helium.

The sun is a sphere of intensely hot gaseous matter with a diameter of $1.39*10^9$ m .Its distance from the earth is about $1.5 *10^8$ km, so, the thermal radiation reaches the earth after 8 min and 20 s from leaving the sun, because it has the speed of light in vacuum (about 300,000 km/s). The sun has an effective blackbody temperature of 5760 K. Its central region temperature is much higher. Effectively, the sun is a continuous fusion reactor in which hydrogen is turned into helium. The total energy emitted by the sun is 3.8 *10^{20} MW[14], which equals 63 MW/m^2 of the sun's surface[15]. This energy radiates in all directions and only a tiny fraction of it reaches the earth, which is equal to 1.7* 10^{14} kW[16]; in on the other hand, the world energy demand for 1 year (about 900 EJ) can be collected only by using 84 min of the solar radiation falling on earth. The earth orbits on its axis every 24 h [17], completes a revolution around the sun in a period of approximately 365.25 days, and follows an ellipse at one of the foci, as shown in Figure 1.

From hour to hour and day to day the sun changes its position in the sky. It is common knowledge that the sun is lower in the sky in the winter than in summer. The relative motions of the sun and earth are systematic and thus predictable. Indeed, once a year, the earth moves around the sun in elliptical orbit. At the same time, the earth rotates yearly around the sun, it also orbits about its axis every 24 hours, which makes an angle of 23.45° to the plane of the elliptic. These rotations form the earth's orbital plane and the sun's equator, as shown in Figure 1. [18] .in the table1: we present Some facts on the Sun

Table 1 : Some facts on the Sun[19]

Mean distance from the Earth:	149 600 000 km (the astronomic unit, AU)
Diameter	1 392 000 km (10^9 *that of the Earth)
Volume	1 300 000 * that of the Earth
Mass	1.993 x 10^{27} kg (332 000 times that of the Earth)
Density (at its centre)	>105 kg m^{-3} (over 100 times that of water)
Pressure (at its centre)	over 1 billion atmospheres
Temperature (at its centre)	about 15 000 000 K
Temperature (at the surface)	6 000 K
Energy radiation	3.8 x 10^{26} W
The Earth receives	1.7 x 10^{18} W

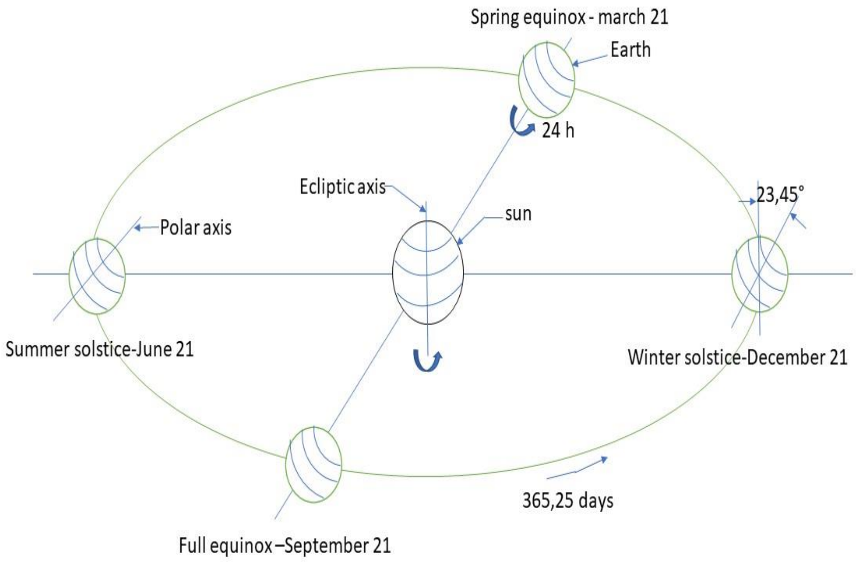

Figure 1 : Annual motion of the earth about the sun[20].

I.3 Solar Energy Potential in Algeria:

Algeria has one of the largest solar potentials due to its geographical position. Indeed, based on satellite data, the German Aerospace Center (DLR) concluded that Algeria has the highest solar capacity in the Mediterranean basin: 169,440 TWh per year[21]. Sunshine period is over 2000 hours a year in almost all of the region[22] and can exceed 3900 hours in the Highlands and the Sahara[23]. For most of the national territory, the regular energy collected on a horizontal surface is about 5 kWh[24], 1700 kWh / m^2 / year for the North[25], and 2650 KWh / m^2 / year for the South[26]. Because of the plentiful sunlight, the climatic conditions in Algeria are ideal for the production of solar energy. especially in the Sahara region, such as the place where we do our experience (university Eloued).

Table 2 : solar potential in Algeria[27].

Areas	**coastal area**	**high plains**	**sahara**
Surface (%)	4	10	86
Area (km^2)	95269	238174	2048298
Mean daily sunshine duration (h)	7.26	8.22	9,59
Average duration of sunshine (h/year)	2650	3000	3500
Received average energy ($KWh/m^2/year$)	1700	1900	2650
Solar daily energy density (KWh/m^2)	4.66	5.21	7.26

I.4 Site Characteristics

The centre of wilaya of El Oued is located 510 km South-East of Algiers; the capital of Algeria. It has a hot desert climate. Winters are mild, with average temperatures around 11 °C in January. Summers are very hot with average temperatures around 32 °C, average maxima around 40 °C and the hottest days approaching 50 °C. Rainfall is light and sporadic, and summers are particularly dry . The geographic position of El Oued is 33°21’ N Latitude and Longitude of 6°5’ E. The location of El Oued in Algeria is shown in figure 2, which represents also the Annual Global Horizontal Irradiation (GHI) of the whole country[28].

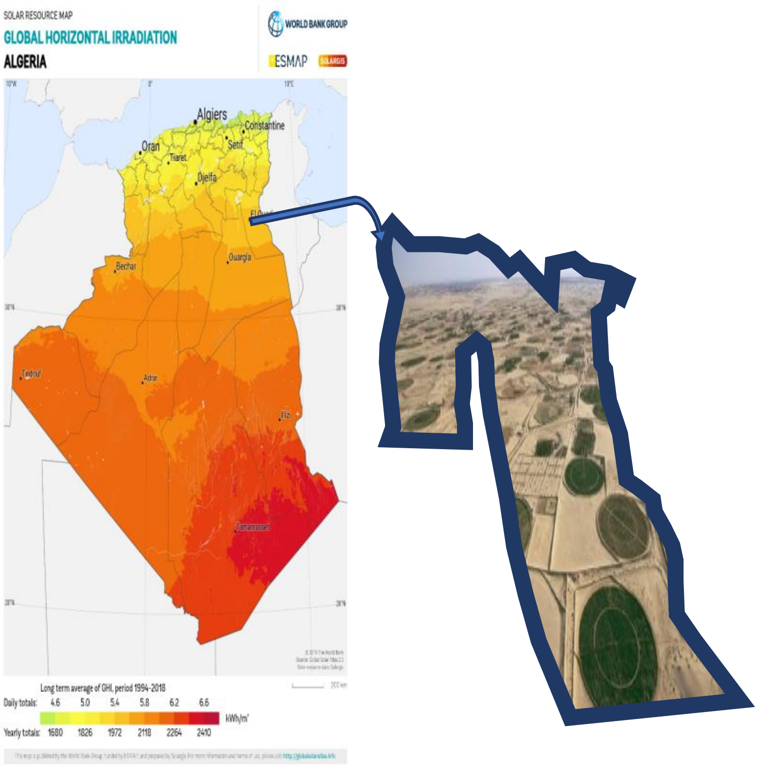

Figure 2 : the Annual Global Horizontal Irradiation (GHI) in Algeria[28].

I.5 some applications of Solar Energy

There are two categories of technologies that harness solar energy, Solar Photovoltaics and Solar Thermal

I.5.1 photovoltaic energy conversion

Photovoltaic (PV) modules are solid-state systems that directly transform sunlight, the world's most plentiful energy supply, into electricity without the use of heat engines or moving machinery. It produces energy without emitting any greenhouse gases or other kind of gases and operates virtually silently. Photovoltaic systems are flexible and can be installed in almost any capacity, from milliwatts to megawatts. Photovoltaic systems are very dependable and need relatively little maintenance. They can also be set up as stand-alone systems.

Figure 3 : the photovoltaic power plant on Bir Sebâa Nord (BRN) in the wilaya of Ouargla[29]

I.5.2 Solar dish systems

The parabolic solar dish is one of the most important methods that use the sun heat as a source of energy, it tracks the sun direction to focus the heat on the receiver.

The applications of the solar dish include electricity generating, cooking, water heating, and irrigation. Efficient solar dishes are characterized by reasonable weight, hardiness against wind deflection, low construction cost, reflectors with high reflation coefficient and with material treated for withstanding temperature and moisture variations. Solar dish systems have a wide range of applications.

The main application of the solar dishes is to generate electrical power ranging from kW to MW. Where the largest benefit and potential market from the solar dish units when are connected to the grid in the power plants facilities. In order to achieve the requested demand from the customers such as peak hours, we can add solar dish units more to the utility grid as requested.

There are a lot of applications of solar dish system such as :

I.5.2.1 electrical generation

The solar-powered Stirling engine illustrated in Figure 4 employs mirrored parabolic to focus and concentrate sunlight onto a receiver situated at the concentrator's focal point. The receiver is intended to convert the absorbed solar energy to the engine's operating fluid (hydrogen in most cases). The absorbed thermal power is then converted into mechanical work by the Stirling engine, which compresses the working fluid when it is cold and expands it when it is heated. To generate electricity, linear motion is turned into rotary motion for drive alternator , To improve performance, these systems must be installed with a dual tracking solar mechanism that holds the reflector of the device always normal to the solar radiation.

Figure 4 : Maricopa Solar Plant[30]

I.5.2.2 cooking

Cooking is a common need for people all over the world. Solar cookers have long been proposed as an interesting alternative to the world's problems associated with cooking fuels demand. Most of the world's solar energy technology is focused on designing solar cookers for residential use. Solar cookers are an environmentally friendly and cost-effective system for harnessing so Solar Thermal (CSP = Concentrated Solar Power) technologies that can be used in the field of cooking. Typically, reflector was used to concentrate solar radiation and converted it into heat. This heat energy was concentrated on a small area which is called the focal point. Finally, from that heat of focal point can easily prepare food or boil water for those underprivileged populations.

Figure 5 : Parabolic Solar Cooker[31]

I.5.2.3 water heating

One of the most widely known solar thermal applications is the solar water heating system. Which uses natural solar thermal technology, where sunlight is converted into heat through collector, this heat transforms to water by using absorber tank.

Figure 6 : Solar water heater[32]

I.5.2.4 Elaboration of thin films

One of the most recent applications of solar energy is the production of thin films, in which the reflecting dish is used to produce heat by focusing sunlight on a glass plate and spraying the solution to be applied on the surface. In this case, the electric heater is replaced with a more ecologically friendly alternative[5].

I.6 Definition of thin film

A thin film is a layer of material ranging from fractions of a nanometer (monolayer) to several micrometers in thickness. Many of the electronic semiconductor devices are the main applications benefiting from thin film construction. The semiconducting material, in thin film form is of particular interest because it has a various number of applications viz.

Thin film plays an important role in the nanotechnology and nanoscience development. Solar cell is an important application of thin film technology from the point in view of global energy crunch, which converts the energy of the solar radiation into useful and constructive electrical energy.

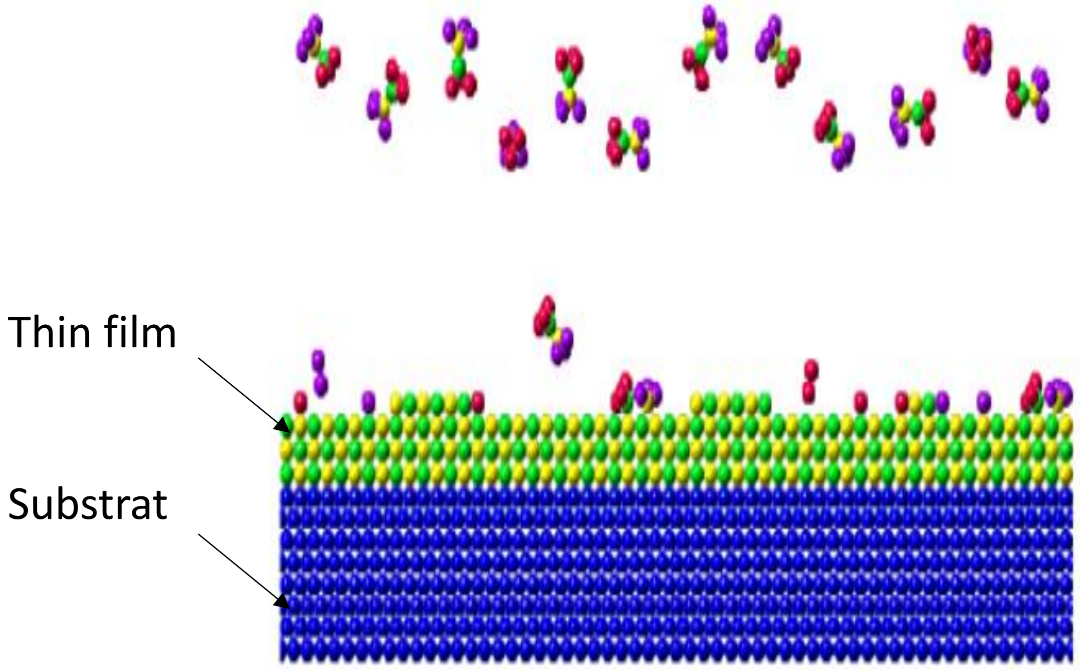

Figure 7 : Thin layer deposition on the substrate.[33]

I.7 Zinc oxide (ZnO)Properties

I.7.1 Basic informations

ZnO is an oxide compound that occurs naturally as the rare mineral zincite and crystallises artificially as solid form "ZnO bulk ". Manganese impurities usually colour zincite red or orange[34]. Figure 8 and 9 shown zincite and synthetic zinc oxide crystal photographs respectively .

Figure 8 : Photographs of orange zincite crystal.

Figure 9 : Photographs of synthetic zinc oxide crystal[35]

The majority of commercially available ZnO is synthesised as a white powder that is practically insoluble in water but soluble in some alcohol solution, such as ethanol and methanol.

I.7.2 Structural properties

Zinc oxide is an II-VI compound semiconductor with a large bandgap. It may have three crystal structures: the uncommon cubic rocksalt, cubic zincblende, and hexagonal wurtzite[36]. These are depicted in figure 10, a, b, and c, respectively. Theoretically, the wurtzite configuration is a more energetically favourable ZnO structure than the rock salt and zinc blende structures. Only growth on cubic substrates will stabilise the zinc blende ZnO structure, while the rocksalt NaCl-type structure is only observed at relatively high pressures (10GPa).

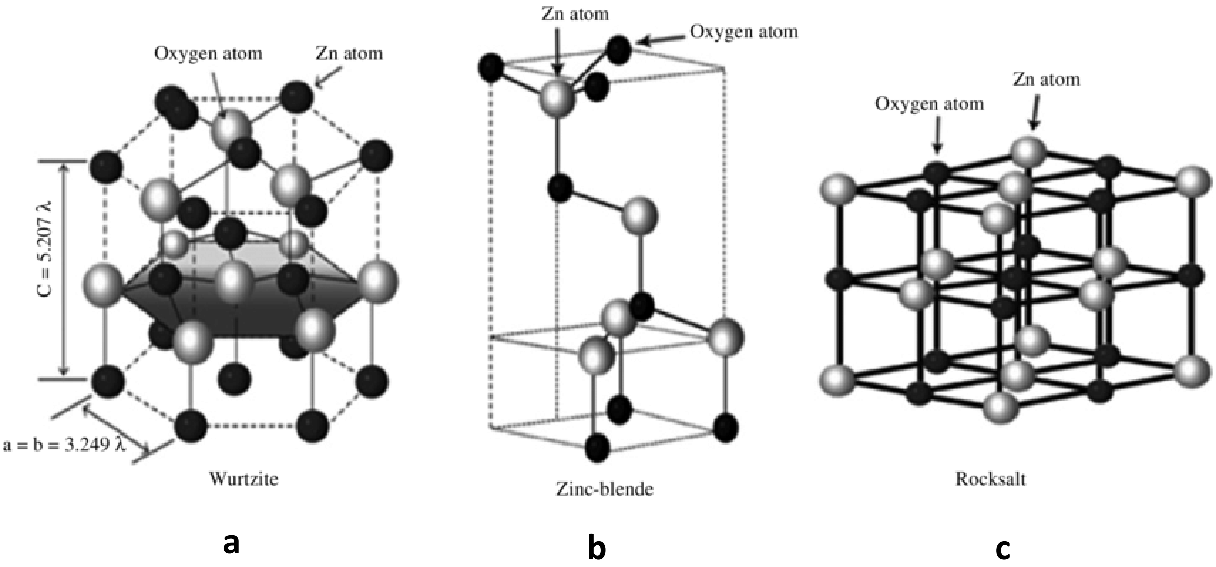

Figure 10 : : Crystal structures of ZnO (a) Hexagonal wurtzite, (b) cubic zinc blende and (c) cubic rocksalt, O atoms are shown as white large spheres, Zn atoms are small black spheres[37]

ZnO crystallises similarly to the majority of group II-VI binary compound semiconductors. The zinc atom is surrounded by four oxygen atoms at the corners of a tetrahedron, and vice versa[38]. Zn^{2+} and O^{2-} planes alternately form along the c-axis of a ZnO crystal. Only growth on cubic substrates can stabilise the zinc-blende ZnO structure, while the rocksalt structure can be obtained at comparatively high pressures[39]. The most frequently found structure in ZnO thin films is wurtzite. In Figure 11, a schematic representation of the ZnO wurtzite crystal structure is seen.

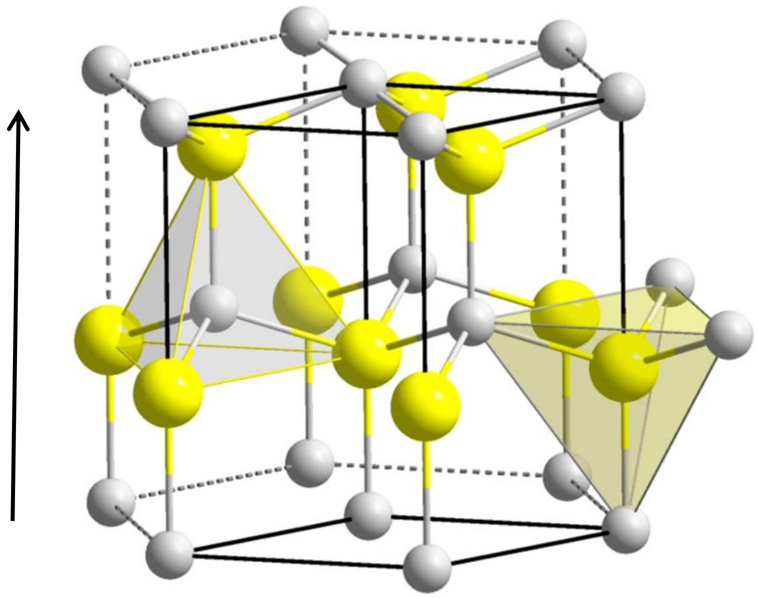

Figure 11 : ZnO wurtzite lattice: small circles is zinc atoms, big is oxygen atoms[40]

Each sublattice in the wurtzite structure has four atoms per unit cell, and each atom of one kind (group II) is surrounded by four atoms of the other kind (group VI), which are coordinated at the edges of a tetrahedron. In a real ZnO crystal, where the wurtzite structure can deviate from the ideal arrangement, and by varying the u parameter, which is known as the length of the bond parallel to the c axis, in units of c; or the c/a ratio.

I.7.3 Optical Properties

The majority of ZnO film applications are evidently related to its optical properties. Since the band gap energy of ZnO at room temperature is 3.37 eV[41], it has good transmission in both the visible and near ultraviolet–visible wavelength ranges. ZnO has a high exciton binding energy (60 meV) and luminesces in the ultraviolet (UV) region (around 380 nm)[42], making it a potential future candidate for UV and blue-light emitting applications. Because of the high exciton binding energy, excitonic recombination can occur above room temperature, and optically pumped lasing has been observed in epitaxial or polycrystalline ZnO thin films.

I.7.4 Electrical properties

zinc oxide has a direct band gap (Eg 3.37 eV). is interesting for a variety of optoelectronic applications. The oxygen 2p levels form the top of the valence band, while the Zn 4s levels form the bottom of the conduction band. Zinc oxide is typically n-type, with p-type activity being incredibly difficult to achieve[43]. There will be defects and accidentally added impurities in any semiconductor, and the most common defects in ZnO are zinc and oxygen vacancies (V_{Zn} and V_O, respectively), since the formation energy for V_{Zn} and V_O is lowest for O-rich and Zn-rich conditions, respectively. Zinc vacancies are a type of vacancy that occurs in the metal zinc

I.7.5 Applications of ZnO

Each ZnO property has its own set of applications. Starting with ZnO's band gap, it is capable of forming clusters of ZnO nanocrystals and ZnO nanowires.

Synthesis of P–N homojunctions has also been documented in some literatures due to its band gap. Many fine optical devices can be made dependent on the free-exciton binding energy of ZnO, which is 60 meV, since a high exciton binding energy allows ZnO to be stable at room temperature and above. ZnO crystals and thin films display second- and third-order nonlinear optical behaviour, making them suitable for use in nonlinear optical applications. In general, the benefit of tuning the physical properties of these oxides, such as zinc oxide, becomes the driving force behind the creation of smart application devices. The electrical, optical, magnetic, and chemical properties of cations with mixed valence states and anions with deficiencies can be very well tuned by permuting and combining the two basic structural characteristics they possess (vacancies). The figure below, Fig.12, summarises the different implementations of ZnO

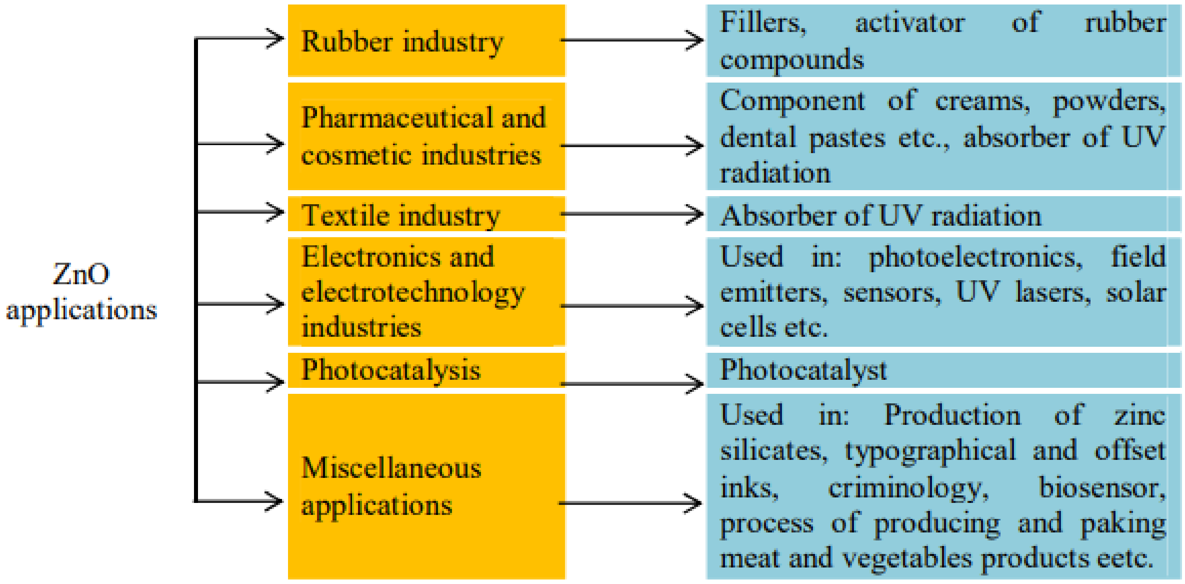

Figure 12 : Schematic representation the applications of ZnO

.

I.8 Nickel oxide (NiO) Properties

I.8.1 Basic informations

The chemical compound with the formula NiO is nickel (II) oxide, which is the most common nickel oxide and it is known as a simple metal oxide. Several million kilogrammes of varying content are processed annually, primarily as an intermediate in the manufacture of nickel alloys. Bunsenite, a mineralogical type of NiO, is very rare. Other nickel (III) oxides, such as Ni_2O_3 and NiO_2, have been proposed.

Nickel Oxide (NiO) It is possible to prepare it in a variety of ways. As nickel powder is heated above 400 °C, it reacts with oxygen to form NiO. Green nickel oxide is produced in some commercial processes by heating a mixture of nickel powder and water at 1000 °C; the rate of this reaction can be improved by the addition of NiO.

Figure 13 : Hydrated nickel chloride[44].

NiO Adopts the NaCl structure, with octahedral Ni^{+2} and O^{-2} sites[45]. The conceptually simple structure is commonly known as the rock salt structure. Like many other binary metal oxides, NiO is often non-stoichiometric, meaning that the $Ni:O$ ratio deviates from $1:1$. In nickel oxide, this non-stoichiometry is accompanied by a color change.

With the stoichiometrically correct NiO being green (figure 13)and the non-stoichiometric NiO being black(figure 14)[46].

Figure 14 : Black nickel oxide powder

I.8.2 Structural properties

Nickel oxide (NiO) crystallizes in a cubic structure of the $NaCl$ type(rocksalt) shown in the figure 15. It has an elementary mesh with parameters a = 4.117 Å, separated by an angle of 90°. It belongs to the space group$Fm3m$, in which the nickel atoms are in an octahedral coordination with six oxygen atoms, with a density of 6.67g / cm^3. [47]

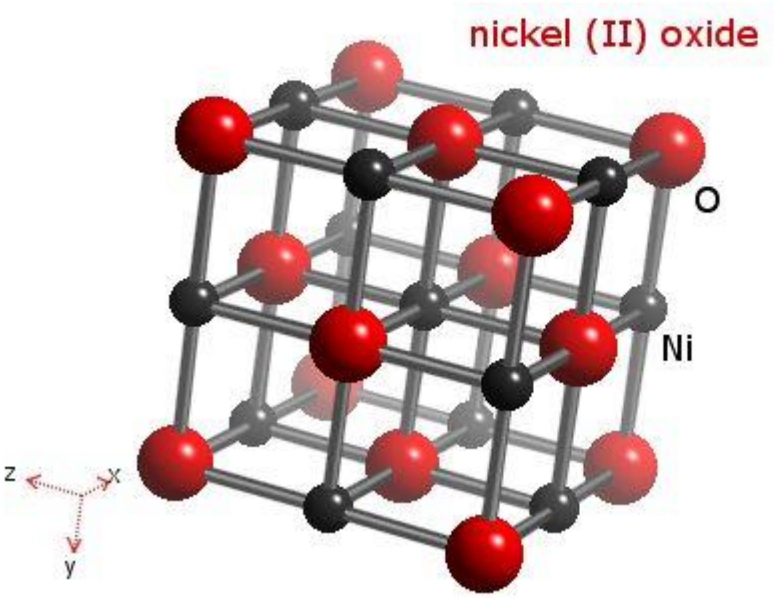

Figure 15 : Crystallographic structure of nickel oxide[48]

I.8.3 Optical properties of Nickel Oxide

The element nickel oxide is green due to heavy absorption of violet (2.75 – 2.95 eV) and red 1.75 eV in the clear conductive oxides (TCO) which have high conductivity and lighting gap energy directly[49]. In the presence of excess oxygen, especially when Ni is oxidised by directly oxygen or doping with Li+, the high absorption coefficient of the green spectrum (1.75 – 2.75 eV) expands and NiO occurs as black. The band gap of NiO thin films varies between 3.6 and 4 eV depending on the deposition technique[50]. Various optical experiments, such as photoemission or inverse photoemission trials, have been conducted to better explain the electrical composition of NiO. Theoretical calculations about optical spectra have also been reported.

I.8.4 Electrical Properties of Nickel Oxide

Nickel oxide electrical properties have been investigated extensively by many researchers. Morin and van Houten [51]have discussed the electronic structure of this oxide and have shown that NiO has no 3d band but full, localized $3d^8$ levels (Ni^+ levels) and empty $3d^9$ levels (Ni^+levels). According to van Houten the $3d^9$ levels are situated 5.4 eV above the $3d^8$levels which lie about 5.3 eV above the filled O^{2-} band. The energy difference between the Ni^{2+} and Ni^+ levels is too high for pure stoichiornetric NiO to behave like an intrinsic semiconductor at room temperatures, and as electron moved between the full localized $3d^8$ levels is not possible, pure NiO is an insulator at ambient temperature with electrical conductivity of $\sigma<10^{-13}\Omega^{-1}.cm^{-1}$ (Figure 16)

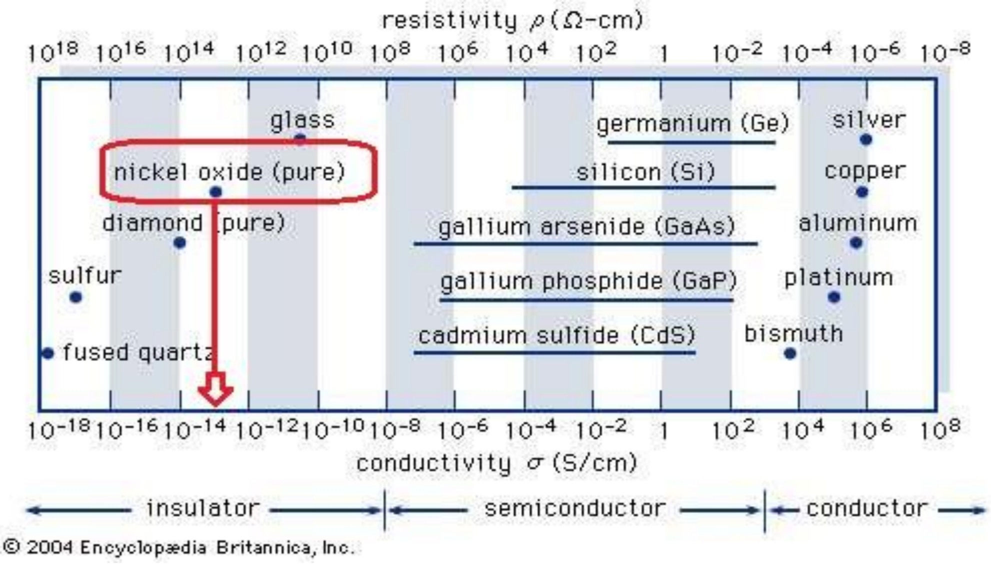

Figure 16 : Typical range of conductivities for insulators, semiconductors, and conductors[44].

Table 3 : Some electrical properties of NiO[44].

Conductivity$\boldsymbol{\sigma}$ $(\boldsymbol{\Omega}.\mathbf{Cm})^{-1}$	≤ 0.1
Mobility $\boldsymbol{\mu}$ $(\boldsymbol{cm^2 / V.S})$	0.1^{-1}
Electronic densities$\boldsymbol{N}$ $(\boldsymbol{cm^3})$	$10^{18} - 10^{19}$
Prohibited band energy$\boldsymbol{Eg}$ $(\boldsymbol{eV})$	$3.6eV - 4eV$
Dielectric constant	11.9

I.8.5 Applications of NiO

Nickel oxide has a range of applications such as:

- In preparation of nickel cermet for the anode layer of solid oxide fuel cells
- In lithium nickel oxide cathodes for lithium ion microbatteries
- In electrochromic coatings, plastics and textiles
- In nanowires, nanofibers and specific alloy and catalyst applications
- As a catalyst and as anti-ferromagnetic layers
- In light weight structural components in aerospace
- Adhesive and coloring agents for enamels
- In active optical filters
- In ceramic structures
- In automotive rear-view mirrors with adjustable reflectance
- In cathode materials for alkaline batteries
- Electro chromic materials
- Energy efficient smart windows
- P-type transparent conductive films
- Materials for gas or temperature sensors, such as CO sensor, H_2 sensor, and formaldehyde sensors
- As a counter electrodes

I.9 Tin oxide (SnO_2) Properties

I.9.1 Basic informations

Tin oxide (SnO_2), also known as stannic oxide(figure17), is a widely applied and studied as ceramic material[52]. SnO_2 belongs to the important class of transparent conductor oxide materials; it was the first to be TCO marketed that combine high optical transparency in the visible range of the electromagnetic spectrum and very good electrical conductivity[53]. Tin oxide thin films are n-type semiconductors. They have a high band gap of Eg = 3.6 - 4.2 eV[54], when suitably doped can be used both as n-type semiconductor.

Figure 17 : Tin oxide (stannic oxide)

I.9.2 Crystalline structure

Tin oxide has a single stable phase at ambient pressure, called cassiterite and adopts a square mesh rutile. Its space group is P4/mnm and it can crystallizes in the tetragonal form [55]. The unit cell has the parameters : a = b = 0.475 nm and c = 0.318 nm and contains six atoms[56]. Each tin ion, Sn^{4+} is at the center of an almost regular octahedron formed by six ions oxygen, O^{2-}, while each O^{2-} is surrounded by three-Sn^{4+} situated at the vertices of a triangle isosceles. The ionic radii of the cation Sn_{4+} and the anion O^{2-} have the values respectively 0.071 and 0.14 nm[57]. A schematic representation of a unit cell oxide tin is reported in Figure 18.

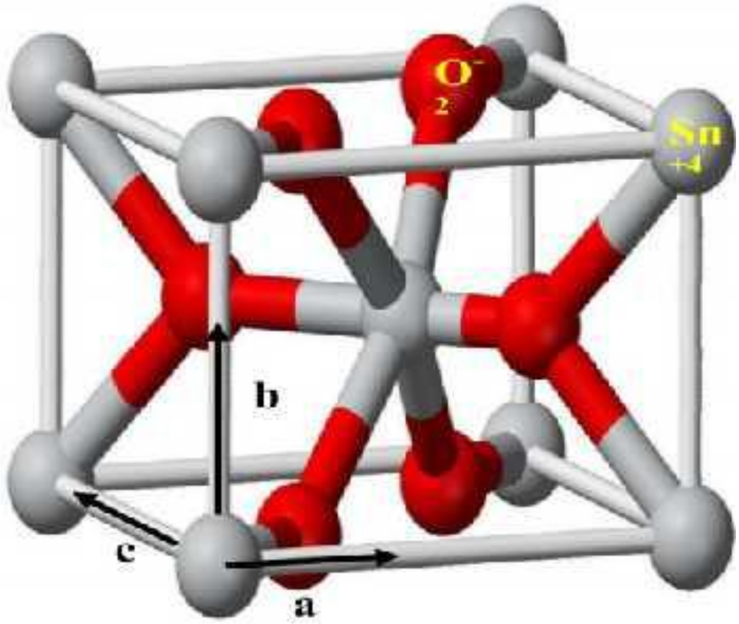

Figure 18 : Unit cell of SnO_2 in the rutile structure[58].

I.9.3 Optical properties

SnO_2 transparent conducting thin films are n-type semiconductors with a direct optical band gap about 3.6 – 4.2 eV[54]. It has a high reflection of solar radiation in the range of infrared and strong absorption in the ultraviolet range, while it has a transmission of the order of 85% in the visible range and it becomes opaque beyond of 1200 nm[59]. This reduction in optical transmission is due to the strong increase of absorption caused by the presence of free electrons; as it will be seen in chapter V.

I.10 Electrical properties

Tin oxide (SnO_2), close to perfectly stoichiometry condition, have low free carrier concentration and high resistivity ($\rho \sim 10^8\ \Omega$ .cm), which is similar to insulation. However, nonstoichiometric forms of these oxide films have high free carrier concentration between 10^{18} and 10^{20} cm^{-3}[60]. In other words, during crystal growth, there is an oxygen vacancy in the structure and therefore the formula for thin film form of this material is SnO_2^{-x}, where x is the deviation from stoichiometry. Indeed, the electrical conduction in this material results from existence of defects in the crystal, generally, either oxygen vacancies or interstitial atoms, which may act as donor. It is possible to increase the free electron concentration or n-type conductivity in SnO_2 film, two important donors for tin oxides are F and Sb, which can increase the n-type electrical conductivity to several orders. F^{1-} substitutes $O^{2-}$with a free electron injected in Bc and Sb^{5+} substitutes Sn^{4+} so that an extra electron enters the lattice.

I.10.1 Applications of SnO_2

Some of the applications of tin oxide are given below:

- Tin oxide nanoparticles' magnetic properties are used in magnetic data storage and magnetic resonance imaging.
- As catalysts, anti-static coatings, and energy-saving coatings
- In solar cells, as electrodes and anti-reflection coatings
- In the production of gas sensors, optoelectronic instruments, and resistors
- Development of liquid crystal displays.

I.11 Thin Film Deposition Techniques

Since the properties of thin films are highly sensitive to the method of preparation, several techniques for depositing thin films of metals, alloys, ceramics, polymers, and superconductors on a range of substrate materials have been developed (depending on the desired film properties). Each approach has advantages and disadvantages, and no single technique can deposit thin films that cover all desirable aspects such as equipment expense, deposition conditions, and the quality of the substrate material, among others.

Thin film deposition can be divided into two main processes: chemical deposition and physical deposition[61]. Chemical methods include gas phase deposition techniques and solution techniques. Precursor solutions are used in gas phase processes such as chemical vapour deposition (CVD) [62]and atomic layer epitaxy (ALE)[63], as well as spray pyrolysis[64], sol-gel[65], spin-coating[66], and dip-coating[67].

Physical methods include physical vapour deposition (PVD)[68], laser ablation[69], molecular beam epitaxy[70], and sputtering[71].

Many criteria should be considered when deciding on a deposition technique, including:

- The nature of the substrate on which the film would be deposited
- • Film thickness expected.
- The film's structure required.
- The use of thin layer.

Controlling the properties of the resulting films requires careful selection of the required deposition procedure. Figure 19 illustrates the grouping of methods:

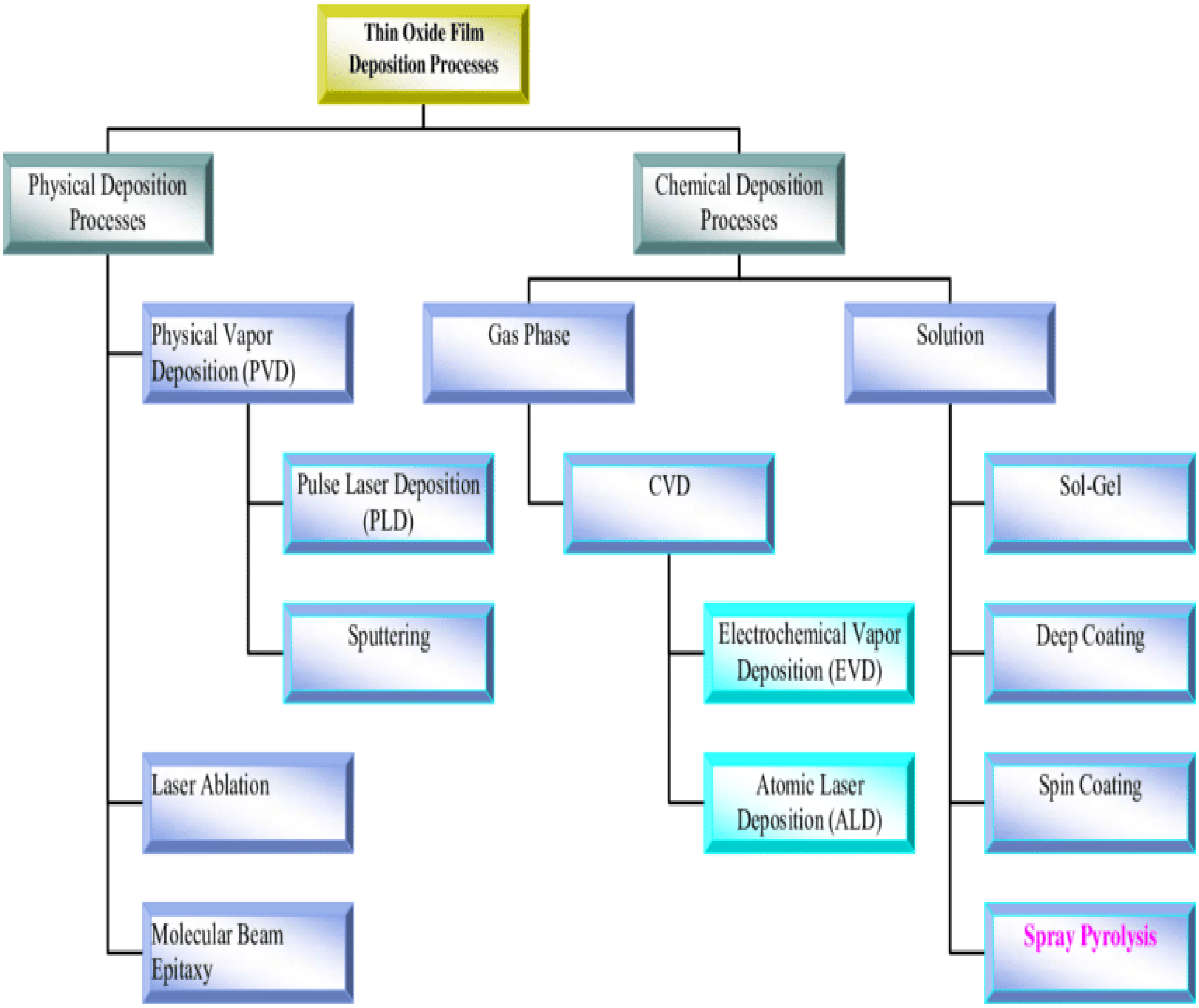

Figure 19 : The classification of deposition methods.

I.11.1 Physical vapor deposition

Physical vapour deposition (PVD) processes (Figure 20) involve vaporising atoms or molecules of a precursor from a solid or liquid source, transporting them as a vapour into a vortex or low-pressure gaseous atmosphere, and condensing them on a substrate. PVD processes will deposit films made of elemental, alloy, and composite materials, as well as some polymeric materials.

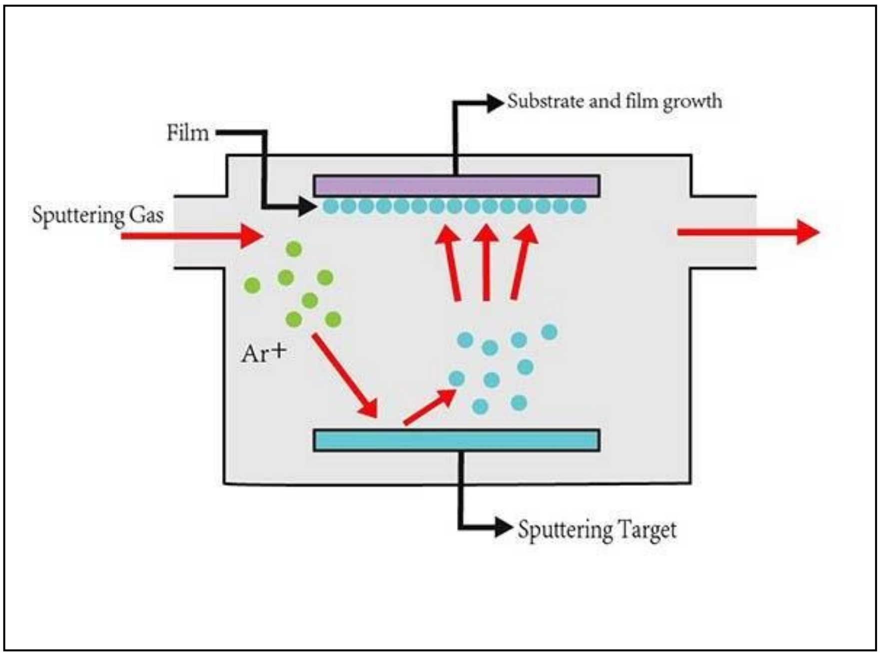

Figure 20 : Physical vapour deposition method[72].

Thermal evaporation and sputtering are the two most frequent PVD methods[73].

Sputtering is a plasma-assisted technique for producing vapour from a source target by bombarding it with accelerated gaseous ions (typically Argon)[74]. Thermal evaporation is a deposition process that relies on the vaporisation of the source material by the use of suitable heating methods in vacuum[75].

I.11.2 Chemical vapor deposition (CVD)

CVD is an effective method for manufacturing thin films of semiconductor materials. The chemical vapour deposition technique entails the reaction of one or more gaseous species interacting on a rigid surface (substrate). Usually, a substance in its solid state is vaporised and diluted with an organic reactant, which will aid the material's surface mobility.

As seen in figure 21, the chemical mixture is transferred to the heated surface and decomposes, allowing the substance on the heated surface to migrate to the expanding film. The decomposition process's nature varies depending on the composition of the volatile transporting species[76]. To prevent the accumulation of powdery deposits, which can result in haziness in the films, the decomposition conditions should be such that the reaction happens only at or near the substrate surface and not in the gaseous state. This process involves volatile and stable precursors. To mention a handful, CVD precursors include halides, hydrides, metal organic compounds, alkyls, alkoxides, carbonyls, dialylimides, and diketonates[77]. Chemical vapour deposition is a technique used to deposit thin films of solid material in a variety of applications such as the fabrication of novel powder[78], fibre[79], preforms of ceramic composites[80], corrosion and wear resistant coatings[81], and synthetic diamond[82]. It is the most commonly used method of IC microfabrication for the wafer's oxide and nitride layers[83].

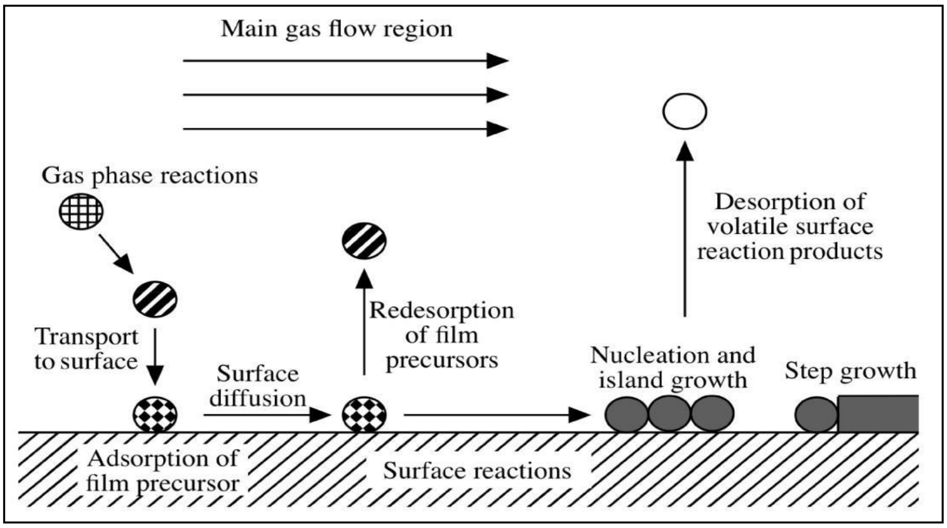

Figure 21 : Steps of chemical vapor deposition technique[77]

I.11.3 Spray Pyrolysis

Spray pyrolysis is a method used to produce thin and thick films[84], ceramic coatings[85] and powders in science[86]. Spray pyrolysis, in contrast to many other film deposition methods, is a very basic and cost-effective processing procedure (especially with regard to equipment costs)[87]. It provides an incredibly simple method for producing films of any composition. Spray pyrolysis does not necessitate the use of high-quality substrates or chemicals. The process has been used for dense film deposition, porous film deposition, and powder processing. Using this flexible technique, even multi-layered films can be easily created. The glass industry and the manufacture of solar cells has used spray pyrolysis for many decades[88].

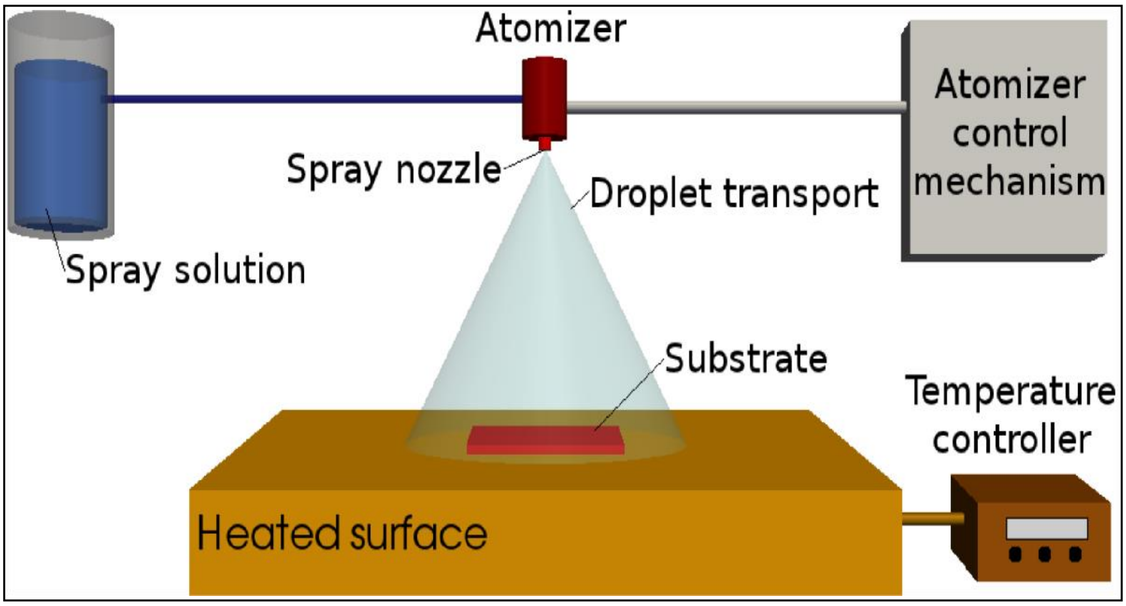

Figure 22 : General schematic of a spray pyrolysis deposition process[89].

The size of the droplet depends on the atomization process[90]; aerosol[91] and ultrasonic spraying generate larger[92] and smaller initial droplets[93], respectively.

When a metallic compound immersed in a liquid mixture is poured onto a preheated layer, it undergoes pyrolytic decomposition. The doping method in CSP is very simple; by adjusting the concentration of the dopant in the solution, the percentage of doping in the sample can be varied. One significant disadvantage of this method is that it cannot be used to deposit very thin films. Another limitation is the substrate selection, which is important since this is a high-temperature procedure.

The main benefits of spray pyrolysis are that the coatings are more stable than vacuum deposited coatings, a wider range of precursors can be used, and the technique can be used at a reduced cost than CVD or vacuum deposition.

The coatings are not similar in thickness, which is a drawback. The process of CVD entails vaporising the precursors and directing the resulting gases onto a hot substrate.

I.11.3.1 Advantages of Spray Pyrolysis Technique

The following are the key benefits of spray pyrolysis over other related techniques:

- Spray pyrolysis is inexpensive and simple to conduct.
- Coated substrates with complex geometries are possible.
- Spray pyrolysis deposition produces coatings that are relatively uniform and of high quality.
- Manufacturing does not necessitate high temperatures (up to 500 °C).
- Spray pyrolysis-deposited films can be replicated.

I.11.3.2 Spray pyrolysis by solar heating

Spray pyrolysis has been used to deposit a lot of variety of thin films; these films were applied in various devices. It is observed that often deposited thin films properties related on the preparation parameters.

The spray pyrolysis equipment consists of precursor solution, substrate heater, an atomizer and temperature controller. The electrical substrate heater is usually used in spray pyrolysis technique, but recently solar heating has been used as an alternative to electric heating, as we have relied on this mode in our work.

The Solar heating use a reflector to focus solar radiation onto a receptor, where it is transformed into heat. This heat energy was focused on a small area known as the focal point, and substrates were mounted in this focal point to heat at the desired temperature. This method has many advantages over the traded one which used in particular electrical energy.

The main advantages are:

- ➢ use solar energy, which is considered renewable, green and free energy (economic way)
- ➢ this technique more safety that the traditional one, in many ways:
    - no problems electric (electric shock, melting electrical trac and socked)
    - working in the new method is outside so we are away from bottlenecks, also we avoid the influence of the interaction of chemical products with each other
- ➢ the work in this method is not related to others friends such as space limitations, use of devices or electricity (work outside)

- the energy conversion in this technique faster than the conversion of electrical to thermal energy (the substrate temperature rises quickly so allow the work faster and more perfect)
- the energy used in the solar spray pyrolysis method clean and can be supplied without environmental pollution

The only disadvantage of this method that we cannot work in cloudy weather and at night.

I.12 Conclusion

In this chapter, we talked about the sun and some of its dimensions, the energy that the sun provides to the earth, and its advantages. Algeria's fortune with this energy, we shed light on the Eloued city and the splendor of its green Sahara. then we turn to specific applications of solar energy, after that we defined the thin film. also, we explained some applications of this layer followed by a presentation of bibliographic study of zinc, tin and nickel oxides, which illustrate the structural, optical and electrical properties. At the end of the chapter, we finished by an explanation of thin film preparation techniques and we focused on the method of spraying pyrolysis. In the next chapter we will study our technique of elaboration, which is based on solar energy as a source of heat and we will dwell on characterization methods

Chapter II

Elaboration Technique and Characterization Methods

II.1 Introduction

Spray pyrolysis entails atomizing a precursor solution to create an aerosol, which is directed to a heated substrate to produce a thin layer. This technique is used in wide areas of surface applications to create a thin film with strong properties. The spray pyrolysis process has many benefits, including low cost, requires basic deposition machines, fast fabrication of large-area films, and the ability to perform molecular doping. Especially, are suitable for the fabrication of oxide thin films. This chapter first gives a brief overview of the Experimental tools of a homemade SPT system and describes the experimental parameters. The second part discusses the specific characterization techniques used to determine the structural, optical, and electrical properties of each layer.

II.2 Elaboration technique

II.2.1 Experimental montage used

The schematic experimental of the solar spray pyrolysis method is shown below in figure 23, the main component in this system is the solar concentrator which replace the electrical substrate heater. our technique consists also of atomizer and solution-carrying bottle, air compressor and pressure gauge, multimeter and thermocouple.

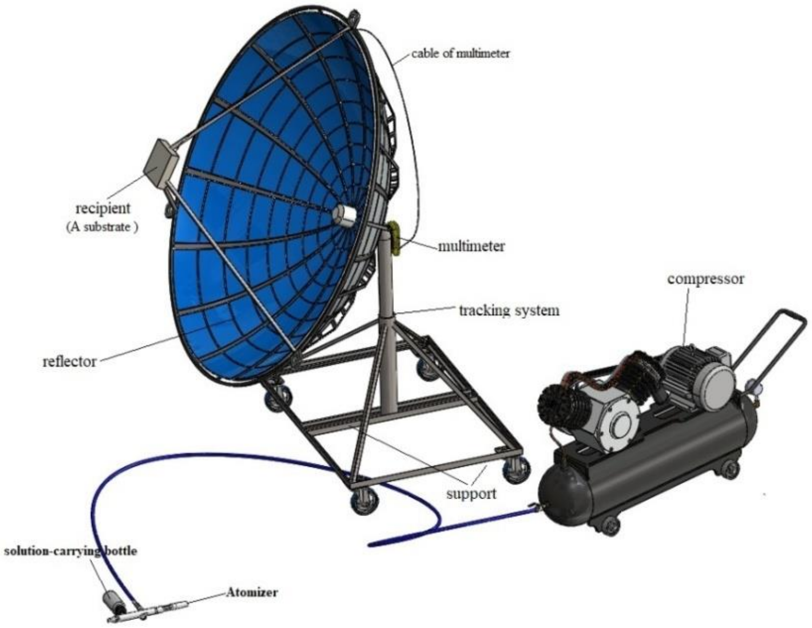

Figure 23 : Full experimental system assembly. .(Designed by Solidworks)

II.2.1.1 The solar concentrator

The solar concentrator is composed of the following elements:

II.2.1.1.1 Reflector

Our experimental device's reflector is a parabolic concentrator with an opening diameter of 2.2 metres[5]. It has a reflecting coating on its inner surface (a hundred small surfaces of mirrors). Which reflect sunlight on the face of a receiver located at the concentrator's focal point. To ensure solar follow-up, the concentrator is installed on a directional support with two axes. (See figure 24).

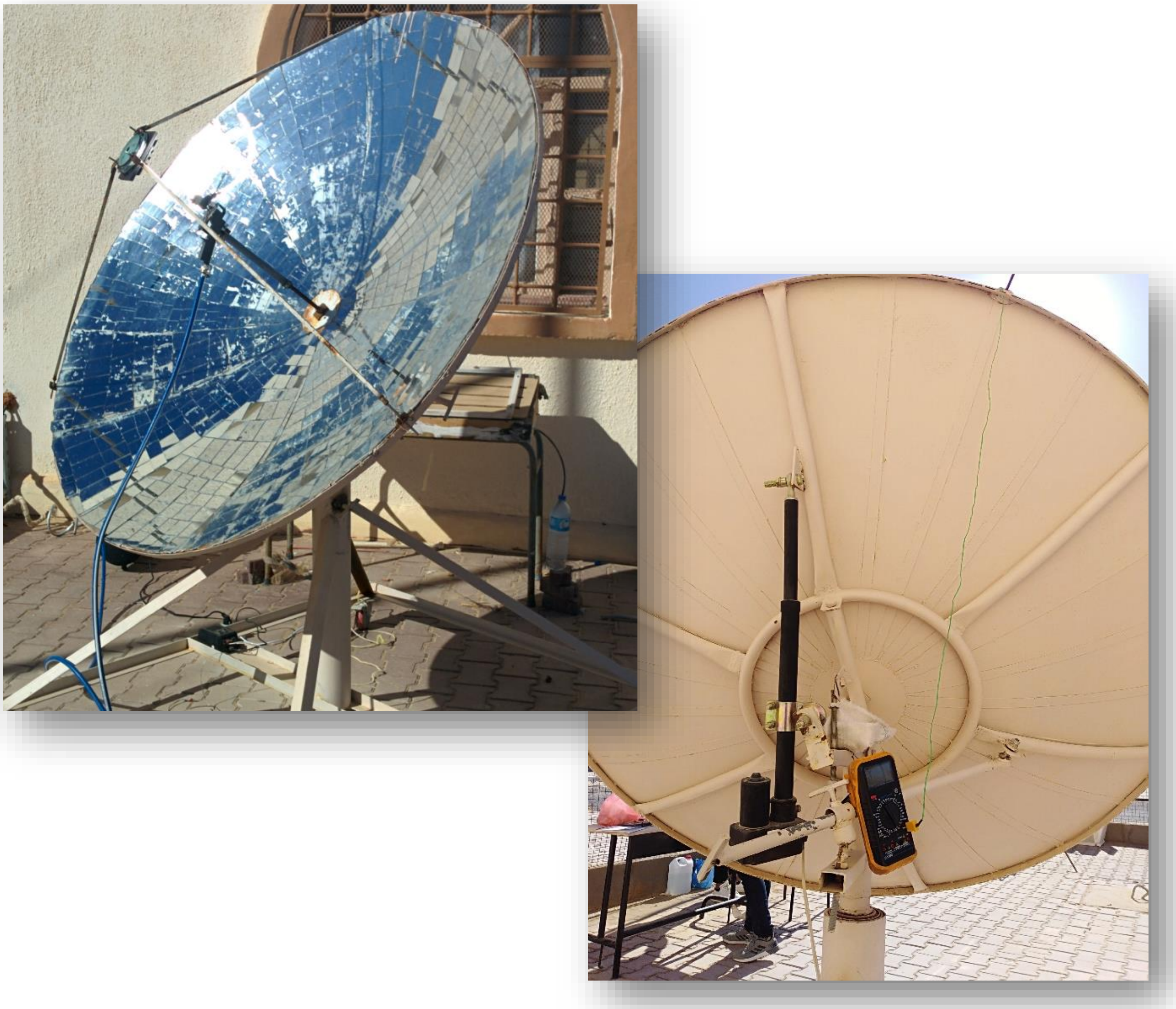

Figure 24:satellite reflector dish.

II.2.1.1.2 Receiver

The receiver of a solar dish system is the interface between the concentrator and the substrate holder. it absorbs a large part or the radiation reflected by the concentrator dish and converts it into heat (Figure 25).

Figure 25: receiver (substrate holder).

II.2.1.2 Atomizer and solution-carrying bottle

the atomizer is an element which transforms the carrying bottle solution into droplets. It is placed on an adjustable support to control the distance between it and the substrates, (Figure26).

Figure 26: the atomizer with the solution-carrying bottle.

II.2.1.3 Air compressor

An air compressor is a pneumatic system that transforms power (via an electric motor) into potential energy and stores it in pressurised air in a large capacity air tank(figure 27).

Figure 27 : Air compressor used

II.2.2 The used measure instruments

In this work, we use many instruments such as pressure gauge and multimeter which are used to measure the air pressure at the output of the compressor tank and the temperature of the substrate during the deposition of oxides.

II.2.2.1 Pressure gauge

A pressure gauge (figure 28) is fixed to the pressure tank's outtake, which records the pressure of the air as it is supplied from the tank. There is a bypass control valve that can maintain output pressure. where Compressed air is routed to the atomizer via a pipe

Figure 28: the pressure gauge 0-12Bar / 0-170PSI

II.2.2.2 Thermocouple

Type K thermocouple, commonly referred to as Chromel/Alumel, is the most commonly used thermocouple currently. Type K thermocouples are designed primarily for general temperature measurements in the most common atmospheres. The maximum continuous operating temperature is approximately 1100°C, although oxidation above 800°C causes the sensor to drift and it gradually moves out of its tolerance class. However, it can be used short-term up to 1200°C (figure 29).

Figure 29 : type K thermocouple

II.2.2.3 Multimeter

The temperature on the substrate's surface is determined using a multimeter (VCA61A - LCD) via a thermocouple.

Befor starting elaboration of thins, the parabolic concentrator was tested to see the temperature which could be reached, after a few seconds where the concentrator is facing the sun, the multimeter which connects to the receiver via the thermocouple gives a close temperature from 1000 °C (Figure 30).

Figure 30: multimeter and thermocouple.

II.2.3 Empirical details

II.2.3.1 Preparation of the precursor solution and deposition condition

In this experimental study three oxides are deposited (ZnO, NiO and SnO_2).

For ZnO, we will be deposited three series and select different deposition parameters effect that share one or more conditions. In NiO, since it has properties similar to ZnO, we had chosen another parameter effect

As for SnO_2, we will choose a common parameter effect with ZnO to see the substrate temperature effect

The conditions for preparation and deposition of these layers are illustrated below.

Zinc oxides

To prepare the ZnO solution in 100 ml of water, 0.1M of Zinc acetate dihydrate ($Zn(CH_3COO)_2$, $2H_2O$) was used. The solution was mounted on the heater at 60 °C; in this configuration, drops of HCl can be applied to the solution as a stabiliser when heating. After this operation, the solutions become transparent.

ZnO thin films were sprayed on the heated glass substrates at various parameters:

- included undoped-ZnO thin films, investigating with various values of substrate temperature from 350, to 450°C with 50°C of step, at pressure 2 bar and 11ml of precursor for each layer.
- included undoped-ZnO thin films, investigating with various values of deposition rate7,11 and 13 ml, at pressure 2 bar and glass substrate temperature at 450°C.
- included Ni-doped ZnO thin films, investigating with various Ni content (0, 1, 2, 3, and 6 at %), at pressure 2 bar and glass substrate temperature at 450°C and 10ml of precursor for each layer.

Nickel oxide

NiO solution was prepared by dissolving (0.05, 0.10 and 0.15 $mol.l^{-1}$) from the industrial powder of Nickel nitrate hexahydrate $Ni(NO_3)_2.6H_2O$ in the solvent containing equal volumes absolute H_2O, then have added drops of hydrochloric acid HCl stabilized (97.7% purity) as a stabilize the solution. The mixture solution was stirred and heated in increasing temperature between 25–50 °C for 3 h to yield a clear and transparent solution.

NiO thin films were sprayed on the heated glass substrates at 450°C with various concentrations and 2 bar of solution pressure and 10 ml of precursor for each layer.

Tin oxides

The prepared solutions SnO_2 have been dissolved of 0.1 M of the Tin(II) chloride dihydrate $SnCl_4.2H_2O$ in the absolute H_2O, HCl was used as a stabilization solution of SnO_2. The solution was stirred and heated at 40 °C to obtain high transparent solution. The prepared precursor deposited at various deposition rate (5, 10 and 15 ml) and pressure 2 bar, on heated glass substrates at 450°C.

II.2.3.2 Preparation of substrates

The type of glass substrates used in this work is (CITOPLUS-REF-0302-0004), which are an optical microscope slides in size of (75×25×1 mm^3), this type is used for their availability, low price, and suitable for films properties (figure 31).

The substrates were washed ultrasonically for five minutes in acetone, followed by deionized water for the same amount of time at room temperature, and finally dried.

Figure 31 : substrate glass

II.2.3.3 Deposition steps of thin films

the deposition of thin films with spray pyrolysis technique powered by solar energy started by preparation of substrate where this latter was washed ultrasonically for five minutes in acetone, followed by deionized water for the same amount of time at room temperature, and finally dried; after that the substrate placed in its holder at the focal point of the concentrator.

the precursor was prepared at required condition and placed at bottle, which placed on an adjustable support to control the distance between it and the substrates; the precursor transform to droplet with the help of air pressure which can be adjusted through the tap built into the compressor with the pressure gauge.

The concentrator was turned using controlled tracking system which is a technique that tracks the sun in two different axes using two pivot points to rotate. Solar tracker system in this type usually has both horizontal and vertical axes.

Once the concentrator was turned face the sun, the temperature of the substrate measured by the multimeter and thermocouple raised into the desired temperature, when the spray was started and it was be in harmony with the substrate temperature. Since the temperature will be reduced after a period of spraying, spraying is done sporadically, allowing the solar heater to adjust the temperature; among the advantages of this heat mode compared by electrical one is the wait time, where desired temperature is quickly returned, so time of the deposition is less compared to the electrical heating.

II.3 Characterization techniques

The techniques used for the characterization of the thin layers produced are:

- X-ray diffraction (DRX): for the study of structural properties.
- The UV-Visible spectrophotometer: for the study of optical properties.
- The four-point technique: for the study of electrical properties.

II.3.1 Structural characterization

II.3.1.1 X-ray diffraction (XRD)

- **Introduction**

X-ray diffraction crystallography for powder samples is well-established and widely used in the field of materials characterization to obtain information on the atomic scale structure of various substances in a variety of states. Of course, there have been numerous advances in this field, since the discovery of X-ray diffraction from crystals in 1912 by Max von Laue and in 1913 byW.L. Bragg andW.H. Bragg[94]. The origin of crystallography is traced to the study for the external appearance of natural minerals and a large amount of data have been systematized by applying geometry and group theory. Then, crystallography becomes a valuable method for the general consideration of how crystals can be built from small units, corresponding to the infinite repetition of identical structural units in space.

- **Energy dispersive X-Ray Diffraction**

X-Ray diffraction is used for the investigation of crystalline materials. All crystalline materials have one thing in common: their components (atoms, ions or molecules) are arranged in a regular manner. This is a necessary requirement for XRD as diffraction can only occur, if X-rays are scattered by a periodic array of particles with long-range order (Figure 32).

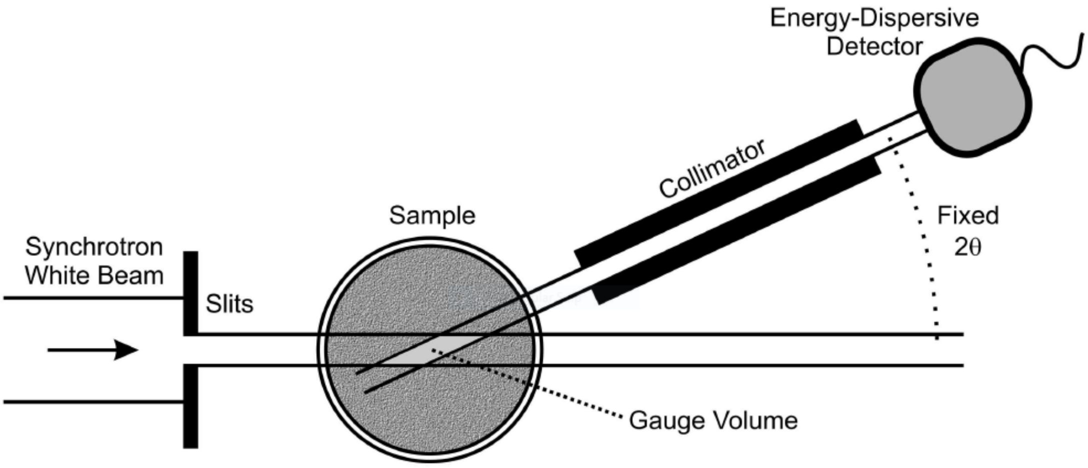

Figure 32: Diagrammatic representation of the energy dispersive diffraction (EDD) method. The energy discriminating detector at fixed scattering angle determines the wavelength of each detected photon and thus the interplanar spacing d of the diffracting lattice planes[44].

The propagation velocity $\boldsymbol{c}$ of electromagnetic wave (photon velocity) as a function of frequency $\boldsymbol{\upsilon}$ and wavelength $\boldsymbol{\lambda}$ is given by the relation:

$$c = v\lambda(ms^{-1}) \qquad \text{(II.1)}$$

The light velocity in the vacuum is an universal constant given by c =299792458 ms^{-1} $\approx (3 \times 10^8 \mathrm{m.s}^{-1})$[95]. Each photon has an energy E, proportional to its frequency,

$$E = hv = \frac{hc}{\lambda} \qquad \text{(II.2)}$$

Where h is the Planck constant (6,62607 x 10^{-34} J s) [96]with an energy E expressed in keV, and

wavelength λ in nm, the obtained relation is:

$$E(kev) = \frac{1.240}{\lambda(nm)} \qquad \text{(II.3)}$$

The momentum p is given by mv, which is the product of the mass m, and its velocity v. The De Broglie relation for material wave relates wavelength to momentum.

$$\lambda = \frac{h}{p} = \frac{h}{mv} \tag{II.4}$$

The resulting diffracted X-rays therefore have a various optical path length to travel. The path length's magnitude only depends on the distance between the crystal planes and the X-ray beam's incident angle. This is summarized in Bragg – Equation (Figure 33)

$$n\lambda = 2\,d\sin\theta \tag{II.5}$$

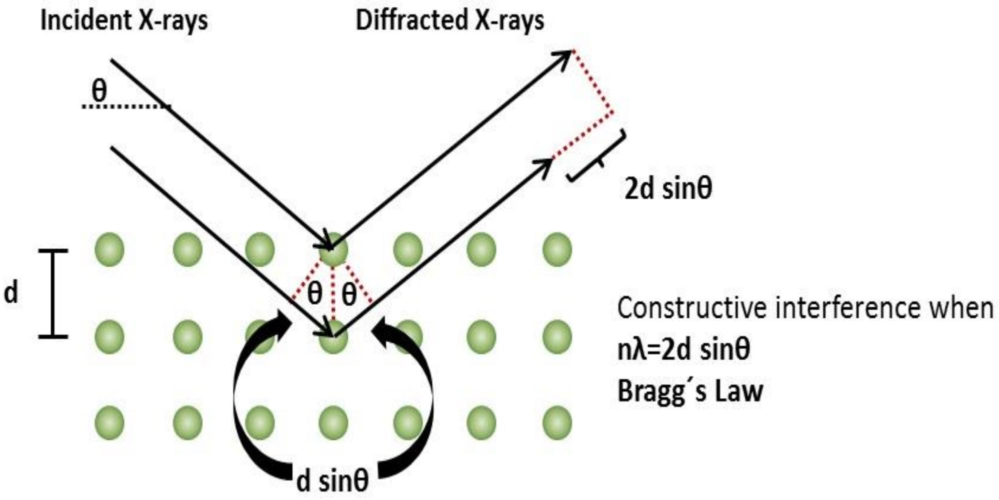

Figure 33: Schematic representation of Bragg equation[97]

➢ Obtainable information from a diffractogram

- **Qualitative Analysis**

Every crystalline material has its own diffractogram. This can be seen as the sample's fingerprint. The material is identified after comparison between the obtained data and databases.

- **Quantitative Analysis**

If the sample is not a pure substance, but consists of different components, the relative amounts of the individual phases can also be calculated.

- **Unit Cell Lattice Parameters**

As mentioned above crystalline materials are arranged in a regular pattern. The material's unit cell is the smallest building block in such a regular arrangement. The dimensions of this unit cell can be characterized using XRD. This is especially intriguing in non-ambient conditions.

- **Crystallite Size and Strain**

The width of the obtained peaks is affected by the crystallite size of the powder. Crystallites smaller than 120 nm produce broader peaks. This can be used to obtain data on the size of the crystallites. Microstrain in the sample also results in peak broadening. XRD measurements can also be used to quantify this effect.

From the X-ray pattern, the width generated in a peak which known as full width at half maximum (FWHM) (See figure 34), can be used to calculate the mean crystallites sizes of the film in a direction perpendicular to the respective (hkl) planes, by using the Scherrer's relation [98, 99], which is given as:

$$G = \frac{0,9\,\lambda}{\beta.\cos\theta} \qquad \text{(II.6)}$$

Where (G) is the grain size for (hkl) peak, (λ) is the wave-length of the X-ray beam, (β) is the full width at half maximum intensity of the peak (hkl) and (ɵ) is the angel between the incident ray and the (hkl) scattering planes.

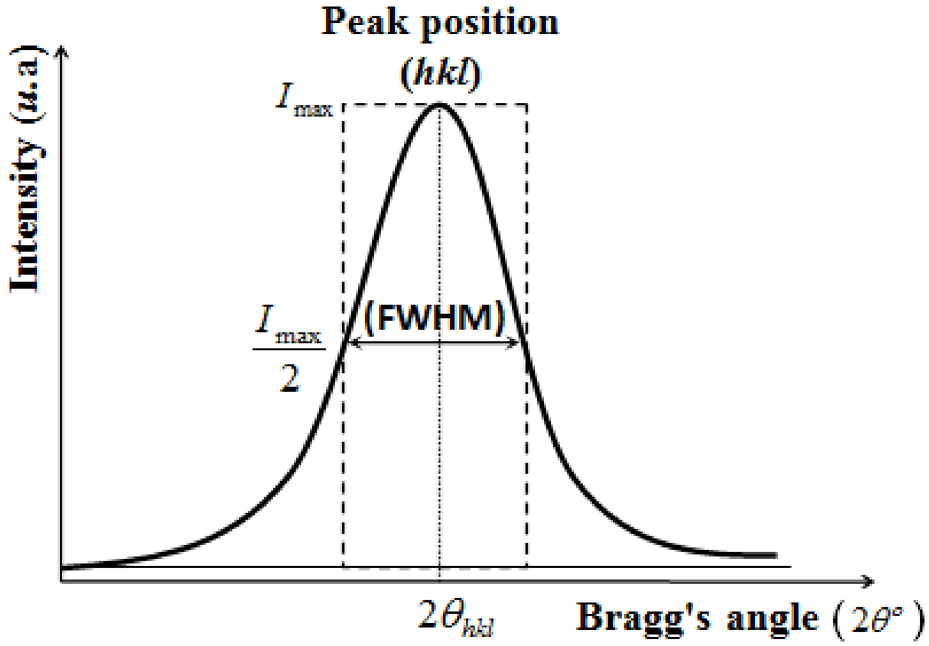

Figure 34: Full width at half maximum (FWHM) of a peak.

- **Texture**

Polycrystalline is such a crystal usually aggregates whose orientations can deviate greatly from complete randomness, which is said to possess texture. To compare the reflex intensities of various orientations they are usually normalized with the tabulated peak heights of the powder diffractograms. We are looking for a normalization of the x-ray peaks that produce quantities that are proportional to the fraction of the material with the corresponding crystalline orientation. For such normalization, approximately equal values for the total normalized scattering power are to be expected for crystalline films with the same thickness. Crystallographic texture in thin films, i.e. the preferred orientation of particular crystal planes relative to the film substrate, is a common and frequently useful phenomenon.

The texture coefficient (TC) represents the texture of the particular plane, deviation of which from unity implies the preferred growth. The (TC) of the samples can be calculated by using the formula:

$$\text{TC (hkl)} = \frac{\mathrm{I(hkl)/I0\ (hkl)}}{\frac{1}{N}\sum_{N}\mathrm{I(hkl)/I0\ (hkl)}} \qquad \text{(II.7)}$$

Where I (hkl) is the measured intensity of a plane (hkl), I_0(hkl) is the standard intensity of the plane (hkl) taken from the JCPDS data and N is the number of diffraction peaks. The value TC (hkl)=1 represents films with randomly oriented crystallites, while higher values indicate the grains-oriented abundance in a given (hkl) direction.

II.3.2 Optical characterization

Thickness is one of the most important thin-film parameters because it greatly influences the film's properties

II.3.2.1 UV-Visible spectroscopy

The functioning of optical measurement (Figure 35) is based on the observation of changes and effects caused by electromagnetic radiation's interaction with matter.

Technically, this necessitates the production of electromagnetic radiation the modification of its properties, and the control of its propagation through a given space. Similarly, the "fingerprints" that the material leaves on the radiation must be reproducible in an understandable form (Figure 36).

Figure 35: Experimental UV-visible spectroscopy device **UV-1800** used

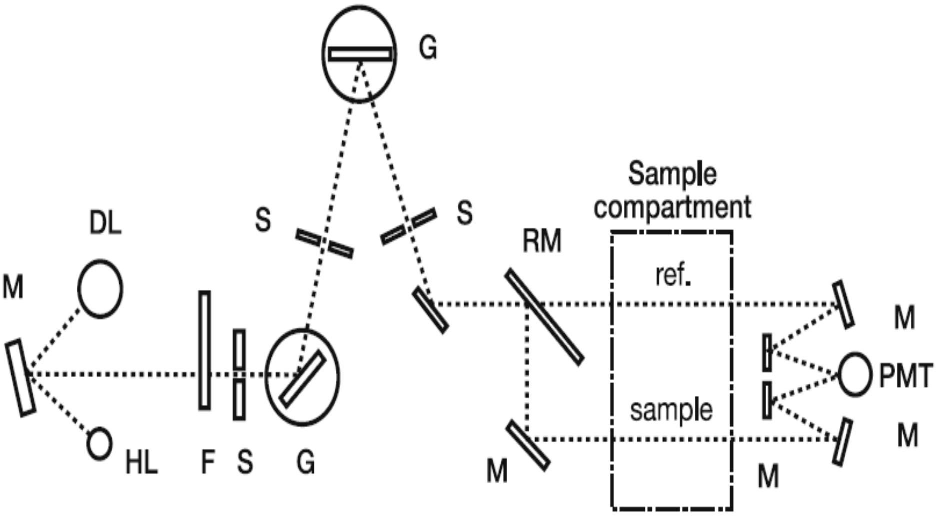

Figure 36: Layout of an imaginary spectrophotometer.[100].

The dotted line represents the optical path. The components are denoted as follows:

HL = halogen lamp.

DL = deuterium lamp.

M = mirror.

F = filter wheel.

S = slit.

G = grating.

RM = rotating mirror.

PMT = detector (photo multiplier tube).

- **Basic handling of UV spectral**

The various qualitative methods are discussed in (Figure37). All these procedures are easy to perform either directly with the spectrophotometer control software, or with the use of any calculation software (for example, Microsoft Excel).

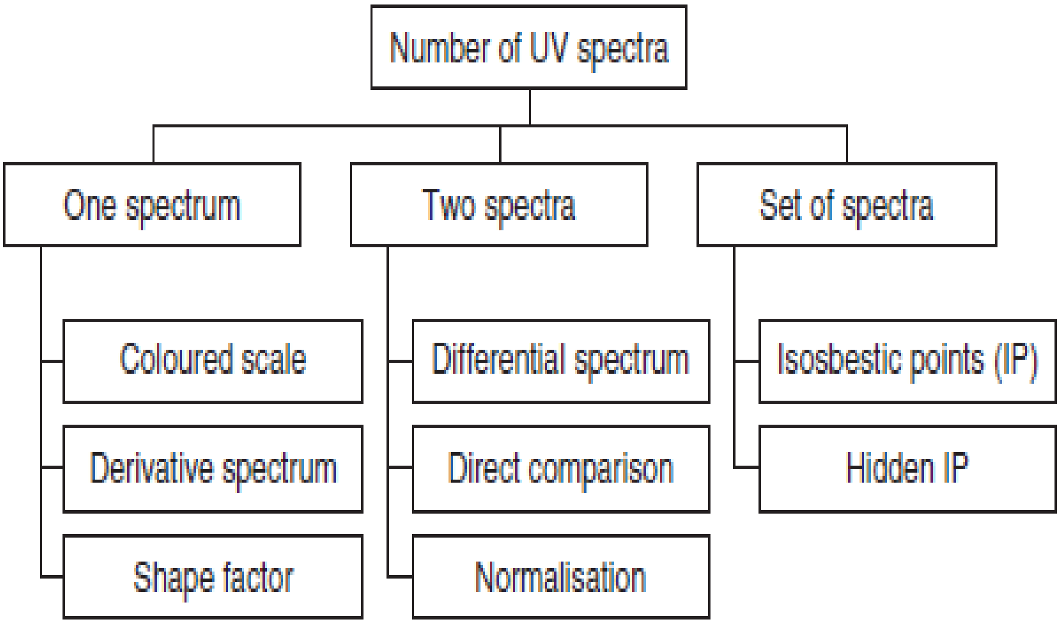

Figure 37**:** Qualitative handling methods for UV-visible spectra [101]

- **Band gap**

The optical band gap (E_g) of the as-deposited layers is determined by Tauc relation:

$$\mathrm{\alpha hv = A(hv - E_g)^n} \qquad \text{(II.8)}$$

Where:

A : is a constant.

hv : is the energy of incident photon.

α :is the absorption coefficient.

And n equals to $1/2$ for allowed direct transition.

The optical gap energy value E_g is estimated by extrapolating the linear region of $(\alpha h v)^2$ versus hv plot

- **Urbach tail**

When the doped samples are exposed to a specific wavelength of light, these defect states trap the excited electrons, preventing them from directly transitioning to the conduction band. As a result, these defect states cause the absorption tail in the absorption spectra, which extends into the forbidden gap. This absorption tail is known as the Urbach tail, and it is linked to the Urbach energy. It can be calculated using the following equation:

$$\alpha = \alpha_0 + e^{\left(\frac{E}{E_u}\right)} \qquad \text{(II.9)}$$

α: is the coefficient of absorption.

E : is the photon energy which equals to hv and E_u is the Urbach energy.[102, 103]

II.3.3 Electrical characterization

A constant current source injects current into the left outer most probe, which is collected in the right outer most one. The potential difference measured across the inner probes with a high-impedance voltmeter is then only dependent on the voltage drop across the specimen surface, thereby eliminating contact resistance phenomena.

Figure 38: Panel (a): Macroscopic probes with probe spacing are much greater than the thickness of the surface space–charge layer, allowing most of the current to pass through the bulk of the crystal.

Figure 38: Panel (b): Microscopic probes with schematic representations of current paths near a semiconductor surface, penetrating only a distance comparable to the spacing between the

probes superstructures on the crystal, the measured resistance is normally interpreted as bulk resistance only[104]

Figure 39: Experimental setup of device of the Four-Probe Method used (KEITHLEY 2400).

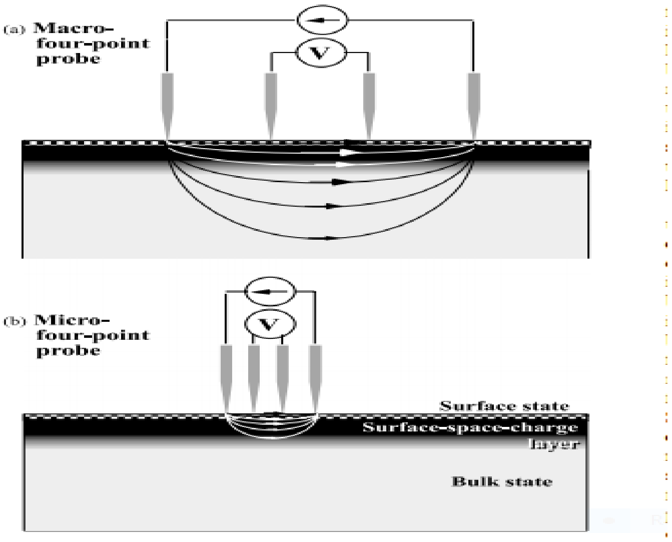

Figure 38: Schematic diagram of four-point probe measurement[44].

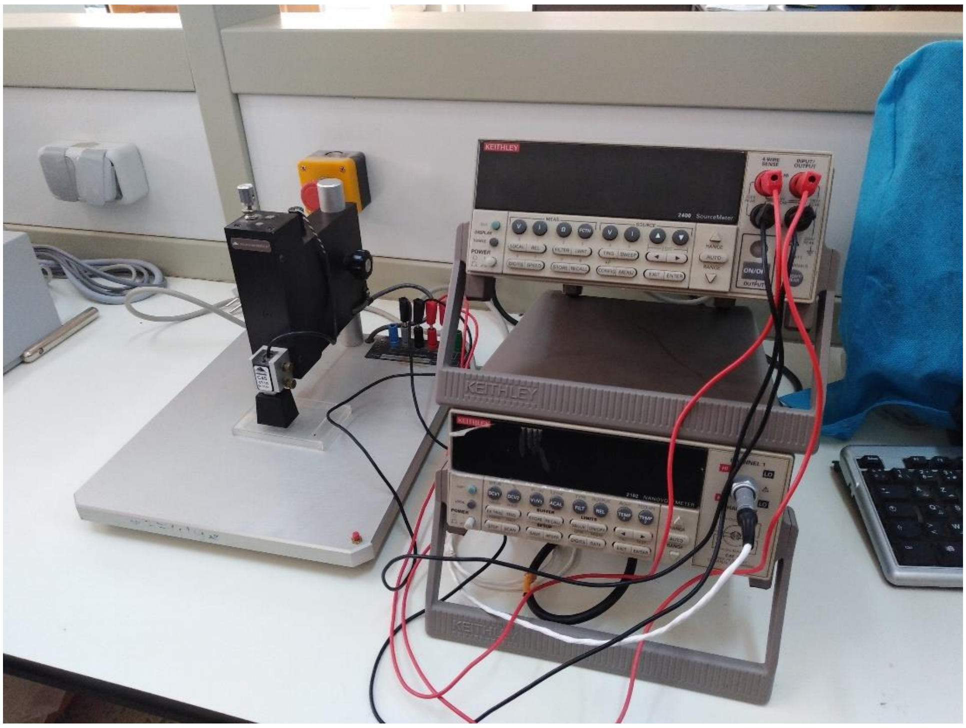

Figure 39: Experimental setup of device of the Four-Probe Method used (KEITHLEY 2400)

II.3.3.1 $V/_I$Measurement on a thin layer of thickness e and resistivityρ

If the thickness is negligible compared to the other dimensions, we can build a two-dimensional model of the conduction which gives:

$$\frac{V}{I} = K \times \frac{\rho}{I} \qquad \text{(II.10)}$$

K: Dimensionless coefficient of 2D geometry (position of contacts, shape of contours) (Figure 38).

The $\rho/_e$ ratio characterizes the layer, we denote it byR_S . We then have:

$$\frac{V}{I} = K \times R_S \qquad \text{(II.11)}$$

R_S Is expressed in Ohms

The coefficient K can be calculated analytically in a few very simple special cases, for example for 4 spikes aligned equidistant on a limitless layer (infinite):

$$K = \frac{\log(2)}{\pi} \qquad \text{(II.12)}$$

(Practical value:$1/_K = 4.532$).

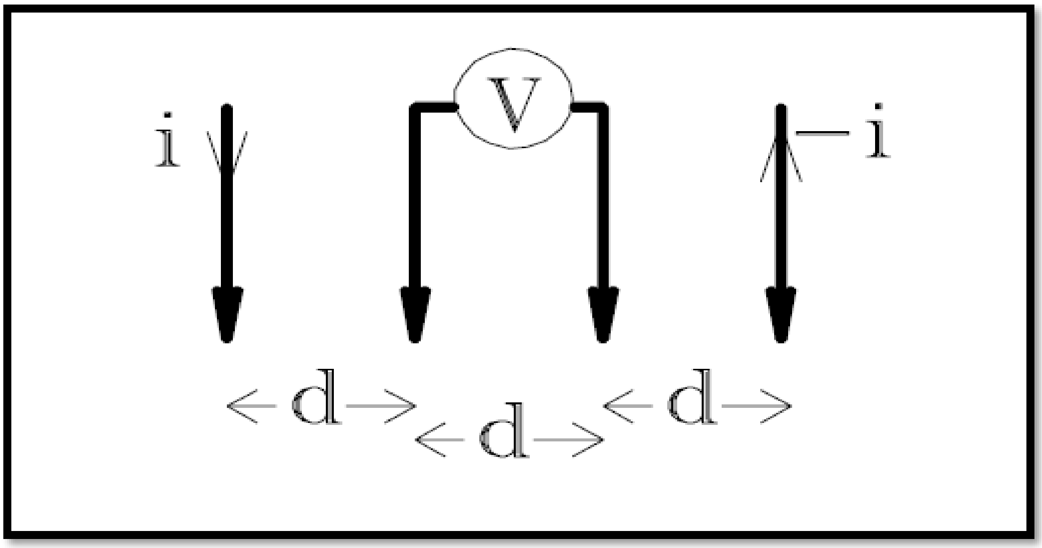

Figure 40: K value (special case)

II.3.3.2 Case of a doped layer

The resistivity is not uniform over the thickness$e$, but formulas (II.2) and (II.3) are still applicable, by generalization of the use of R_S.

We then define an average resistivity $\rho_m$such that: $R_S = \frac{\rho_m}{e}$

If the distribution law of the dopant is known, we can deduce from ρ_m the surface concentration and for different depths.

II.3.3.3 Practical method for 4-point measurement

- perform a $V/_I$ measurement not too close to the edges of the sample.
- express the measurement in $Ohms$.
- multiply by 4.532 to obtain R_S, note this result (always in $Ohms$)(the distance between centers being 1.59 mm, the thickness correction is not necessary).
- express the thickness e of the layer in cm.
- multiply R_S by e to obtain the resistivity ρ or ρ_m , note this result (in $Ohm.cm$).
- use an abacus to deduce the dopant concentration (after possibly conductivity calculation in $\mathrm{Ohm}^{-1}.Cm^{-1}$).

BE CAREFUL: it is not the same chart according to whether the doping is uniform (substrate, Polysilicon deposited) or not (diffused or implanted layer).

II.4 Conclusion

In this chapter, we described carefully the experimental montage of a homemade solar spray pyrolysis system, where we explained all its components such as the concentrator, air compressor, atomizer, receiver (substrate holder), multimeter and thermocouple. Then, we showed how the concentrator heats the substrates. After that, we talked about experimental details in which we discussed the preparation procedure of all types of oxide at different conditions, how to make the substrates ready. At the end of the chapter, we provided the used techniques for the characterization of our thin films such as X-ray diffraction (DRX), UV-Visible spectroscopy, four-point method.

Chapter III

Results of ZnO Thin Films

III.1 Introduction

The current chapter presents and discusses the main experiments and results obtained by the deposition of ZnO thin film at various conditions using spray pyrolysis technique and solar energy as source of heat.

III.2 Characterizations of prepared ZnO thin films

We are deposited some series of ZnO thin films by spray pyrolysis on glass substrates heated by solar system, and we will investigate the effect of substrate temperature, deposition rate and dopants.

III.2.1 Effect of substrate temperature

III.2.1.1 The crystalline structure of ZnO thin films

The spectra's of X-ray diffraction of the deposited ZnO thin films with various temperatures are shown in figure 41.

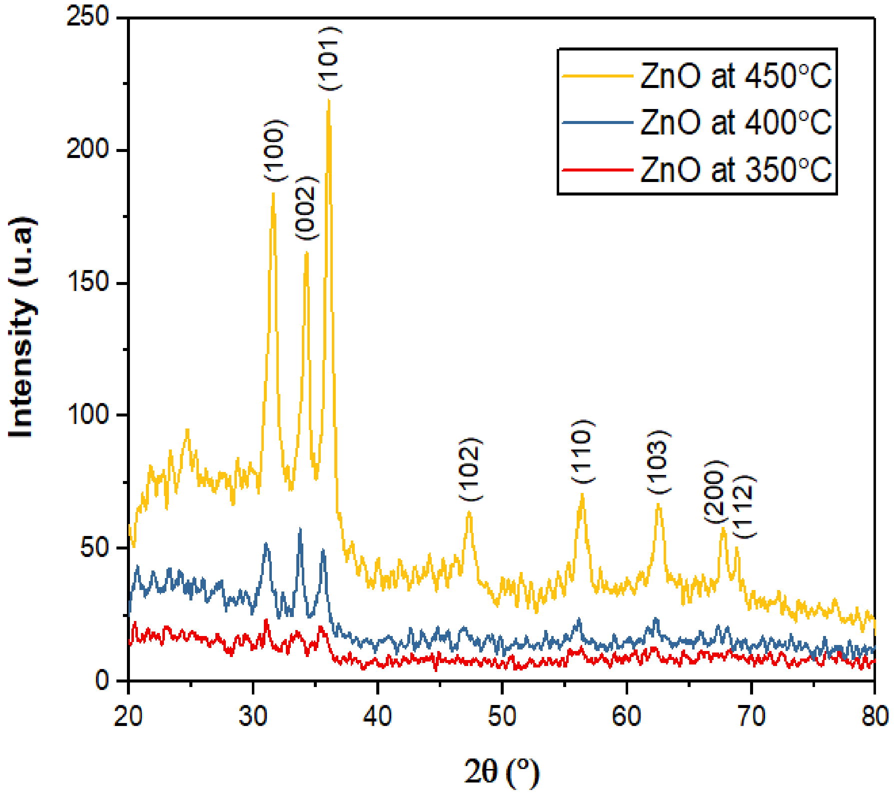

Figure 41:X-ray diffraction spectra of ZnO thin films at different deposition temperature.

Vertical lines show the peak positions and relative peak intensities of a ZnO powder reference (ICSD-26170). As first result, the structure property enhanced with the increase in deposition temperature up to 450°C. It was having a good crystallinity as well as for the peaks presences, which are (100), (002), (101), (102), (110), (103), (200) and (112) planes. It shows that the sprayed ZnO at 450°C was polycrystalline hexagonal wurtzite structure. The diffraction peak at 2θ= 36° related to (101) plan is the highest one with comparing of others of (100) and (002), indicate that the preferred orientation with the (101) plan. However, the crystalline quality of ZnO thin films was affected by deposition temperature to enhance at 450°C. However, the crystallite size of ZnO thin films the (101) plan was estimated using the Scherrer formula (II.6)

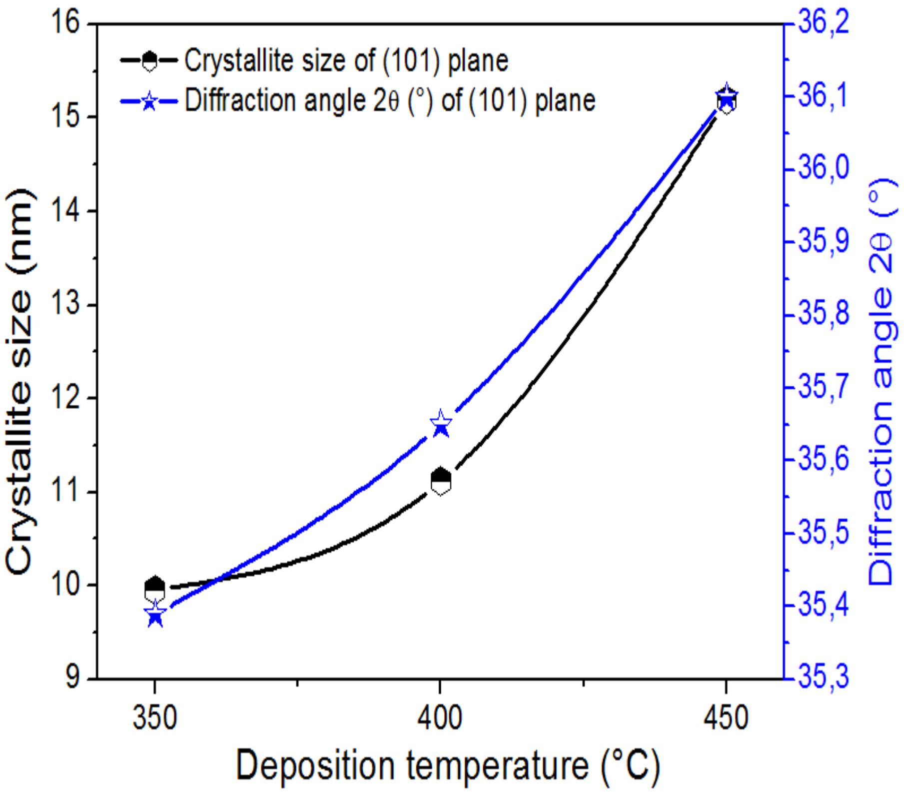

Figure 42:The variation of crystallite size and diffraction angle as a function of deposition temperature in ZnO thin films.

Figure 42 shows the variation of the crystallite size and diffraction angle of (101) diffraction peak as a function of deposition temperature. It can be seen from Figure 42 that the crystallite size increased greatly from 9.96 to 15.19 nm by increasing of deposition temperature from 350 to 450°C. This phenomenon can be explained by the improvement of the crystal structure of ZnO thin films at 450 °C. As can be seen, an increase in the deposition temperature shown that the diffraction angle also was increased due to the existence of sufficiently thicker films in less strained (or more relaxed) state, or by decrease of the defects in the films.

III.2.1.2 The optical properties of ZnO thin films

The optical transmission of ZnO thin films deposited at various temperatures is shown in Figure 43. From this figure the optical transmission was enhanced at 450 °C, this film exhibits an average transmission of about 85% in the visible region. The transmission was decreased greatly in the wavelength varied between 300-400 nm due to the absorption edge. We have found at 300 nm the transmission is higher of others caused by the increase crystallite size (see figure 42). It can be noted that the transmission of ZnO thin films is affected by crysatlinity.

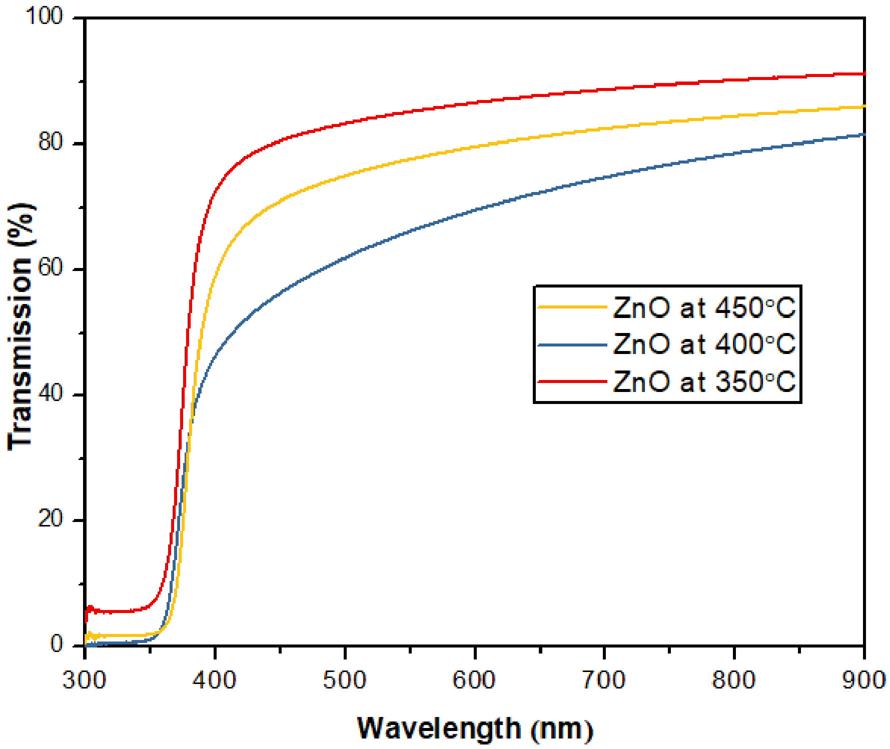

Figure 43:Transmission spectra T(λ) of ZnO thin films as a function of depostion temperature.

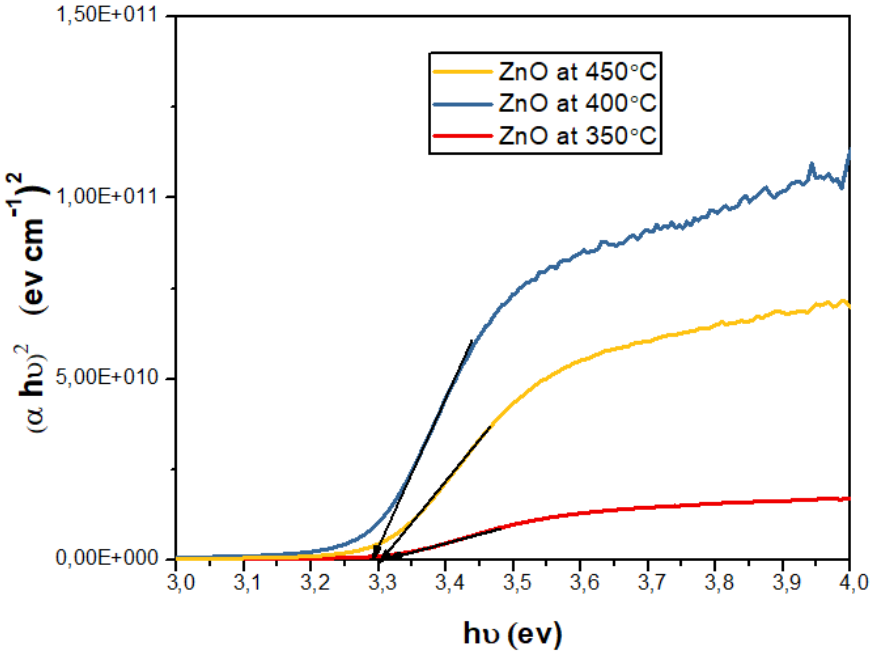

Figure 44:The typical variation of$(Ah\upsilon)^2$ vs. photon energy all deposited ZnO thin film as a function of deposition temperature.

Figure 45 shows the variation of the optical gap energy and the Urbach energy of ZnO thin films at various deposition temperatures.

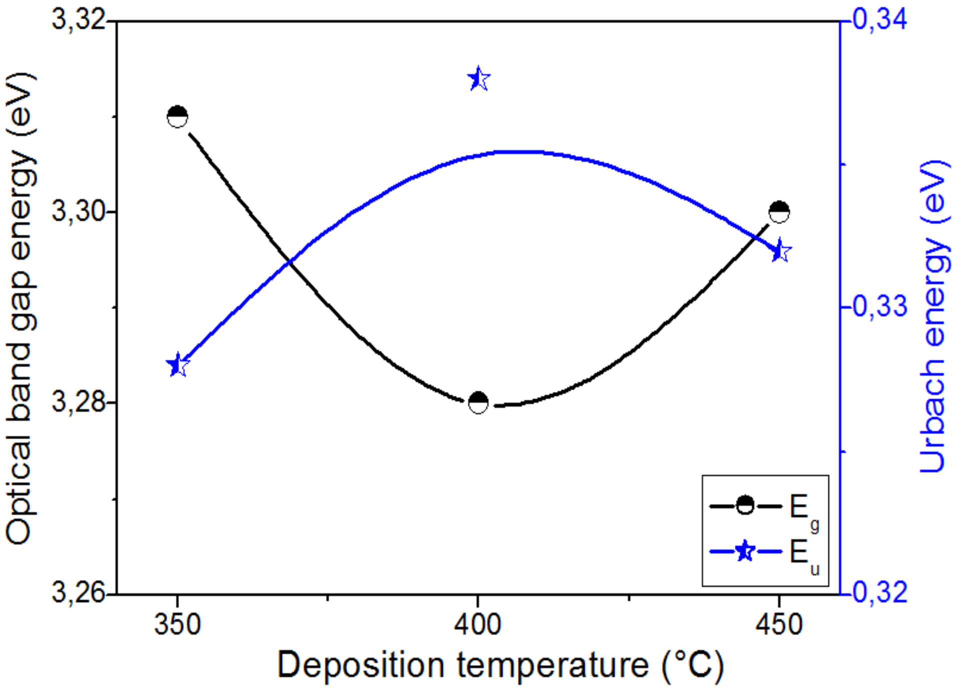

Figure 45:The variation of optical band gape E_g and Urbach energy Eu of ZnO thin films with deposition temperature.

The change is inverses to other due to the conduction band and valence band, with the increase of deposition temperature the optical band gap energy decreases at 400 °C then increase at 450 °C. The increase was affected by the increase of crystallite size (see Figure 42). however, the minimum value of Urbach energy was observed at 450 °C it is 0.328 eV, it is shown that the ZnO thin film prepared at 450 °C has less disorder with few defects, which may be attributed to the decrease of crystallite boundary for an increase of deposition temperature; similar observation was found for optical transmission.

III.2.1.3 The electrical resistivity of ZnO thin films

Figure 46 shows the variation of the electrical resistivity ρ of ZnO thin films as a function of deposition temperature. As result, the electrical resistivity decreased from 0.014 to 0.012 $(\Omega.cm)^{-1}$ for the increase of deposition temperature from 350 to 400 °C, and then increased up to 0.064 $(\Omega.cm)^{-1}$ for 450 °C. The increase in the resistivity of can be explained by the increase of crystallite size (see Figure 42).

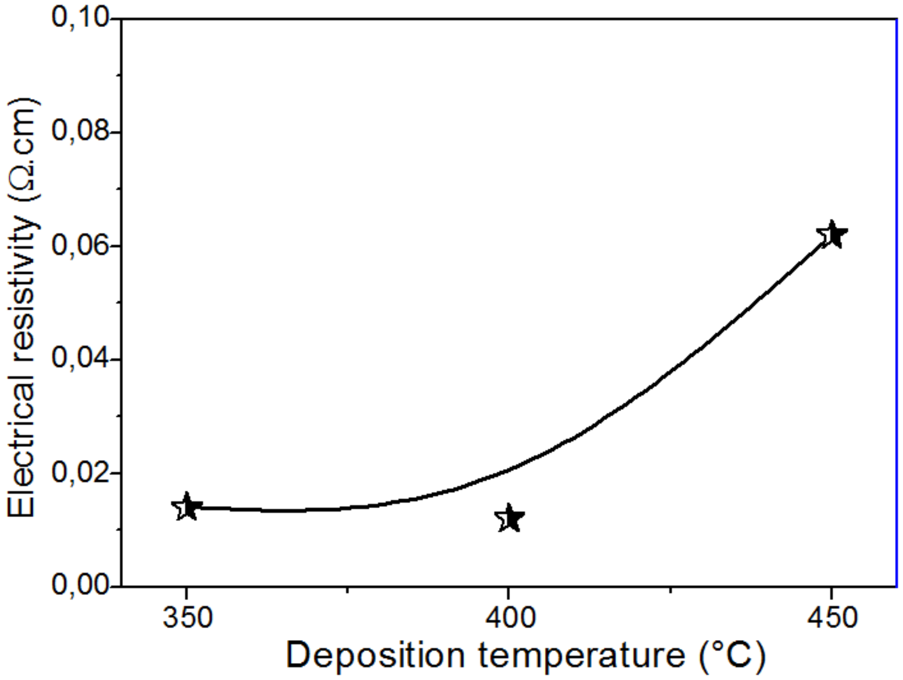

Figure 46:Electrical resistivity of ZnO thin films at different deposition temperature.

III.2.2 Effect of deposition rate:

III.2.2.1 The crystalline structure of ZnO thin films

The X-ray diffraction patterns of the solar spray-deposited ZnO thin films are shown in fig.47. As can be noticed, there are seven quite obvious peaks corresponding to (100), (002), (101), (102), (110), (103) and (112) planes, the XRD spectrum shown well that all films are polycrystalline in nature with a hexagonal wurtzite structure (JCPDS card no. 036-1451).

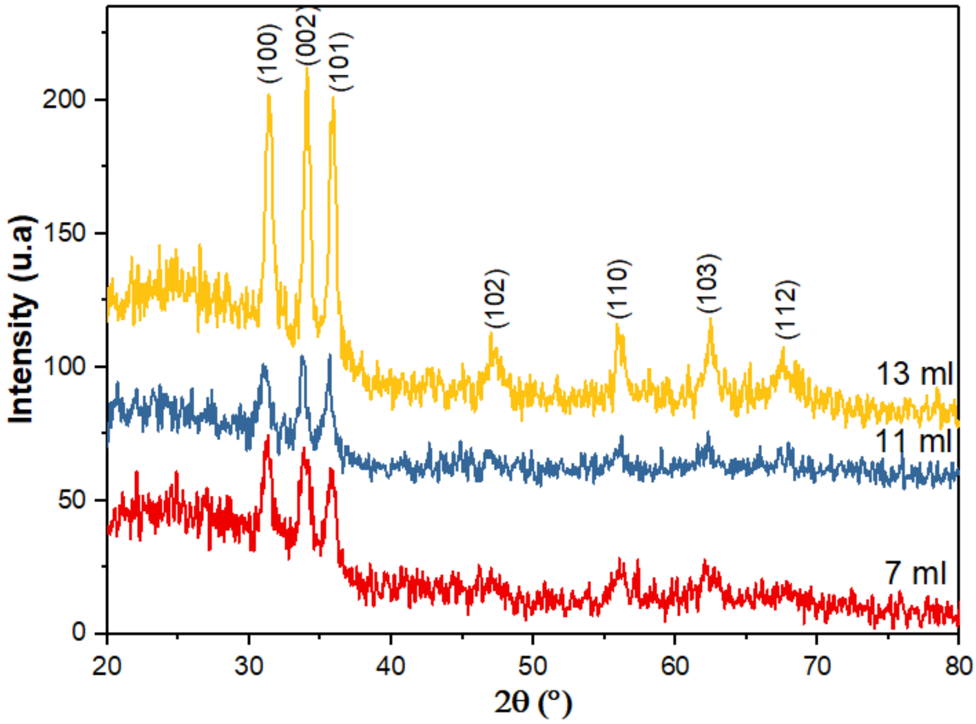

Figure 47: X-ray diffraction spectra of ZnO thin films at different deposition rates.

The XRD patterns of all the samples indicated increased intensities for the peaks due to the increasing in thickness or the quantity of precursors deposed, As can be seen the (002) plane, indicating preferential orientation along the c-axis.

The full width at half maximum (FWHM) ‘β’ of ZnO thin films for (002) plane are given in Table 4. As the thickness increases, FWHM of thin films shows an increase then decrease.

The lattice parameters ‘a’ and ‘c’ were calculated using the lattice spacing (d_{hkl}) of (002) plane.

$$d_{hkl} = \left(\frac{4}{3}\frac{h^2+hk+k^2}{a^2}+\frac{l^2}{c^2}\right)^{-\frac{1}{2}} \qquad \text{(III.1)}$$

The crystallite size of ZnO thin films(G) was calculated using a well-known Scherrer's Formula (II.6).

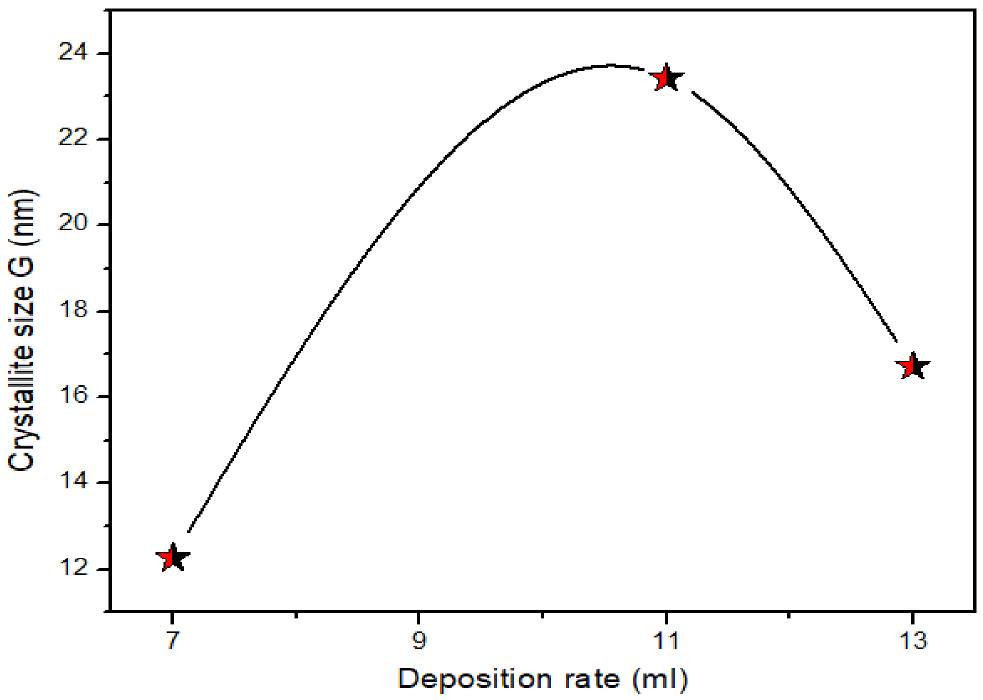

Figure 48: The variation of crystallite size as a function of deposition rate in ZnO thin films.

Fig.48 shows the variation of crystallite size as a function of deposition rate, it can be observed from fig 48 that the crystallite sizes increased until reaching the value 23,43 nm which corresponds to the deposition rate 11ml indicating by an improvement in the crystallinity then deceased which provides an adequate explanation for the deterioration in the crystallinity of the films.

The c-axis strain (ε_{zz}) values have been calculated using the following equation:

$$\varepsilon = \frac{c - c_0}{c_0} \times 100 \ \% \qquad \text{(III.2)}$$

where 'c' is the lattice constant of the thin films calculated from the X-ray diffraction data and 'c_0 'is the lattice constant of bulk ZnO (standard c_0 = 0, 5206 nm).

Table 4: Recapitulating measured values of Bragg angle (2θ), the inter planar spacing (d), the full width at half-maximum (FWHM), the crystallite size (G) and lattice parameters (cand a) for ZnO thin films as a function of deposition rate.

Deposition rate (ml)	**hkl**	2θ **(deg)**	**D (A°)**	**FWHM (deg)**	**G (nm)**	**C (A°)**	**A (A°)**
07	002	33.89	2.64461	0.62	12.26	5.28922	3.305192
11	002	33.75	2.65528	0.32	23.43	5.31056	3.232482
13	002	34.01	2.63565	0.45	16.72	5.2713	3.326635

Table 4 gives the variation of values of Bragg angle (2θ), the inter planar spacing (d), the full width at half-maximum (FWHM), the crystallite size (G) and lattice parameters (c and a) for ZnO thin films as a function of deposition rates.

III.2.2.2 The optical properties of ZnO thin films

The Impact of deposition rate on the optical transmittance of the ZnO samples is shown in Fig.49, as the thickness increases therefore the deposition time increases, the transmittance of films decreases, this result was await, as the deposition time is increased the absorbance of photons in a material increase. Additionally, the roughness is proportional with the thickness which provides increasing in multiple internal reflection at the surface, where gives an adequate explanation for the decreasing in transparency level.

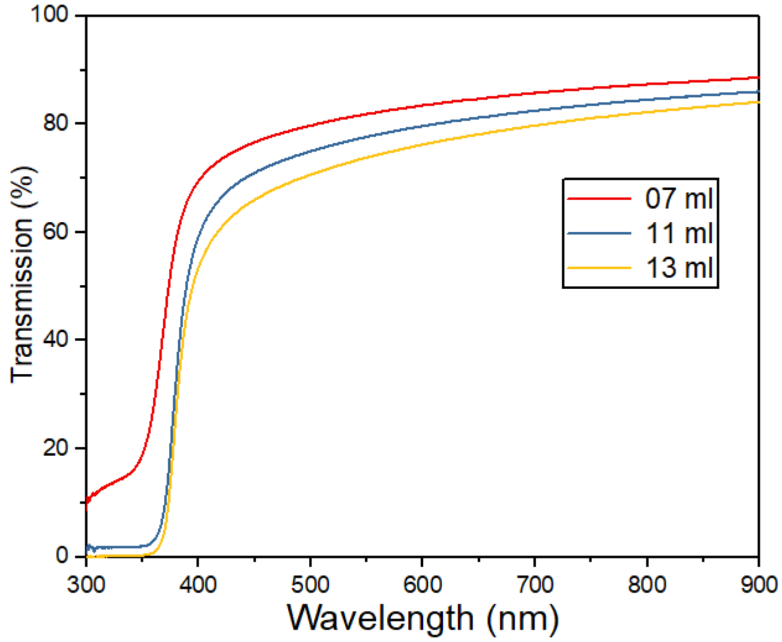

Figure 49: Transmission spectra T(λ) of ZnO thin films as a function of deposition rate:

For further study of the effect of deposition rate on optical proprieties of ZnO thin films prepared by solar spray pyrolysis, we use the transmission spectra recorded between 300 - 900 nm wavelength region to calculate band gap energy (E_g) and Urbach energy (Eu).

The Eg calculated by employed the Tauc plot and using the relation (II.8)

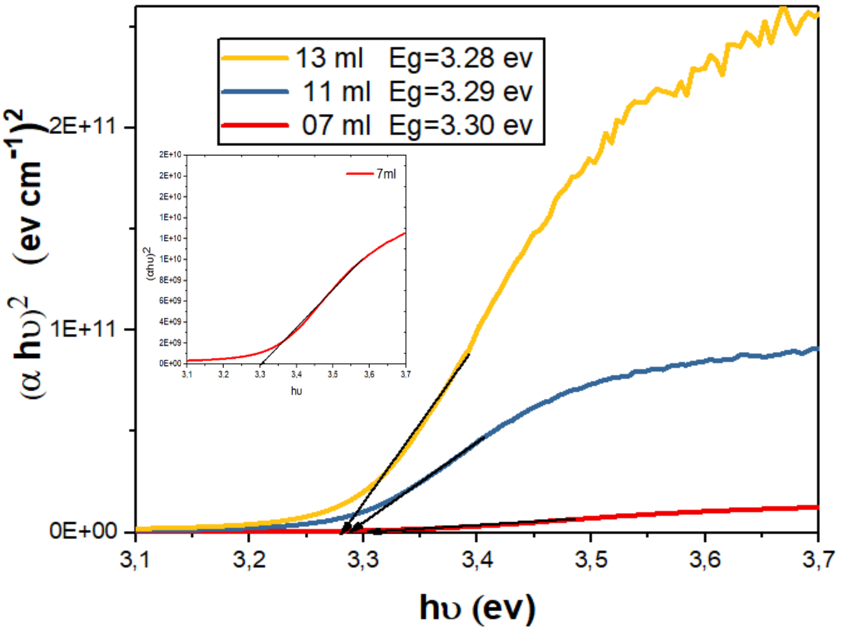

Figure 50: The typical variation of$(Ah\upsilon)^2$ vs. (hυ) all deposited ZnO thin film as a function of deposition rate.

Figure 50 shown a variation of $(Ah\upsilon)^2$ as a function of $(h\upsilon)$ used to inferring optical band gap E_g.

The Urbach tail energy (*Eu*) is expressed using the relation (II.9), The values of E_g and E_u mentioned in table 5.

Table 5: Recapitulating measured values of band gap energy E_g Urbach energy E_u and electrical resistivity (ρ) for ZnO thin films as a function of deposition rate.

deposition rate (ml)	E_g **(eV)**	E_u **(meV)**	ρ **(Ω.cm)**
07	3.30	123.2	1,19
11	3.29	145.6	0,01
13	3.28	190.00	0,08

As it can seen in (Fig 51) the Eg values estimated decreases slightly from 3,30 to 3,28 In contrast the E_u increase with the thickness. This is due to disorder in the film.

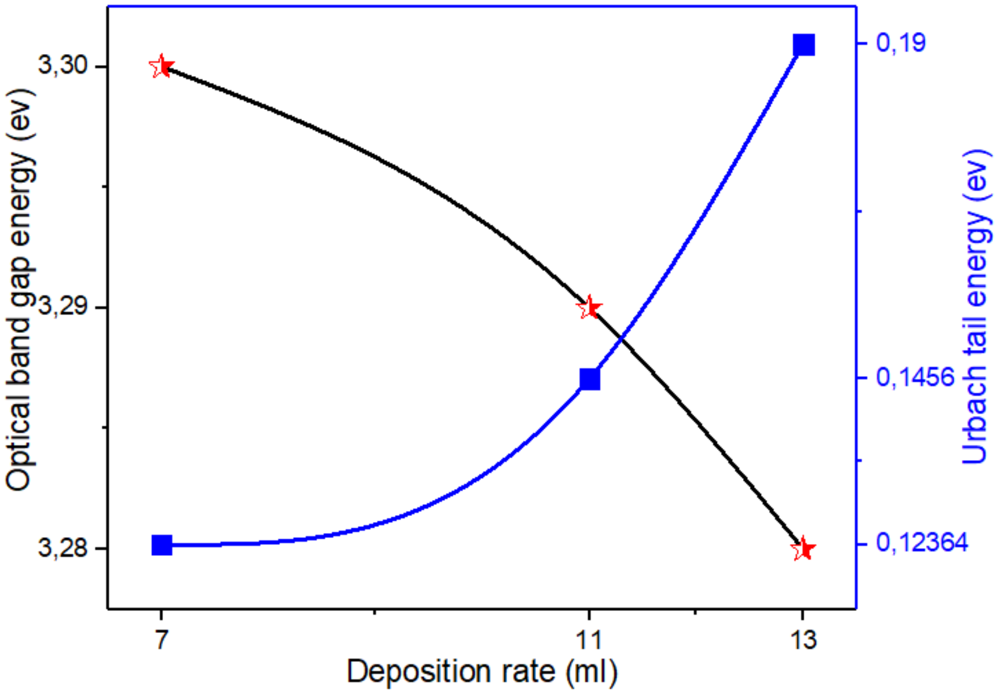

Figure 51: The variation of optical band gap E_g and Urbach energy E_u of ZnO thin films with deposition rate.

III.2.2.3 The electrical resistivity of ZnO thin films

the electrical resistivity was measured by a Keitheley electrometer 2400 using the four-probe method with a closer temperature, where a constant current is applied to the films and the different voltages are concluded.

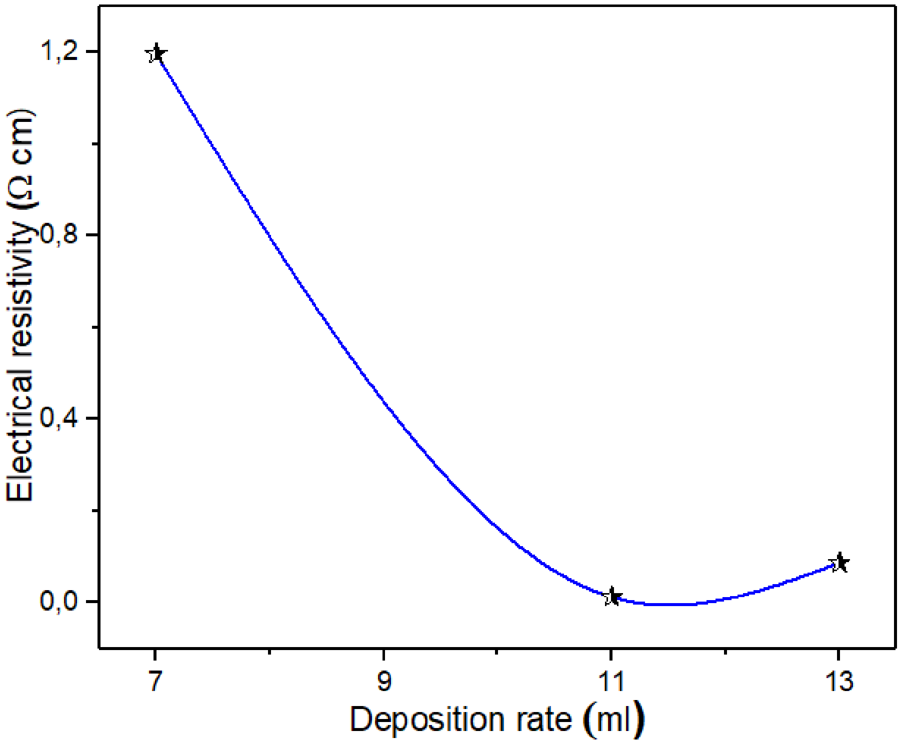

Figure 52: Electrical resistivity of ZnO thin films at different deposition rate.

Fig.52 shows the variation of the electrical resistivity ρ of ZnO at different deposition rates, it can be observed that the resistivity decreases from 1,19 to 0.01(Ω cm) with the increasing of deposition rate from 7 to 11ml then the resistivity slightly increases reach 0,08 (Ω.cm) as the deposition rate increases to 13 ml

The decrease of resistivity from 1,19 to 0.01(Ω.cm) can be explained by the improvement in the crystallite size. Which caused a decrease in grain boundary scattering, as for the increase in resistivity, this is due to deterioration of the crystallinity.

III.2.3 Effect of dopants:

III.2.3.1 Structural Properties of Ni-Doped ZnO Thin Films

Figure 53 shows the effects of the crystalline structure of Ni-doped ZnO thin films.

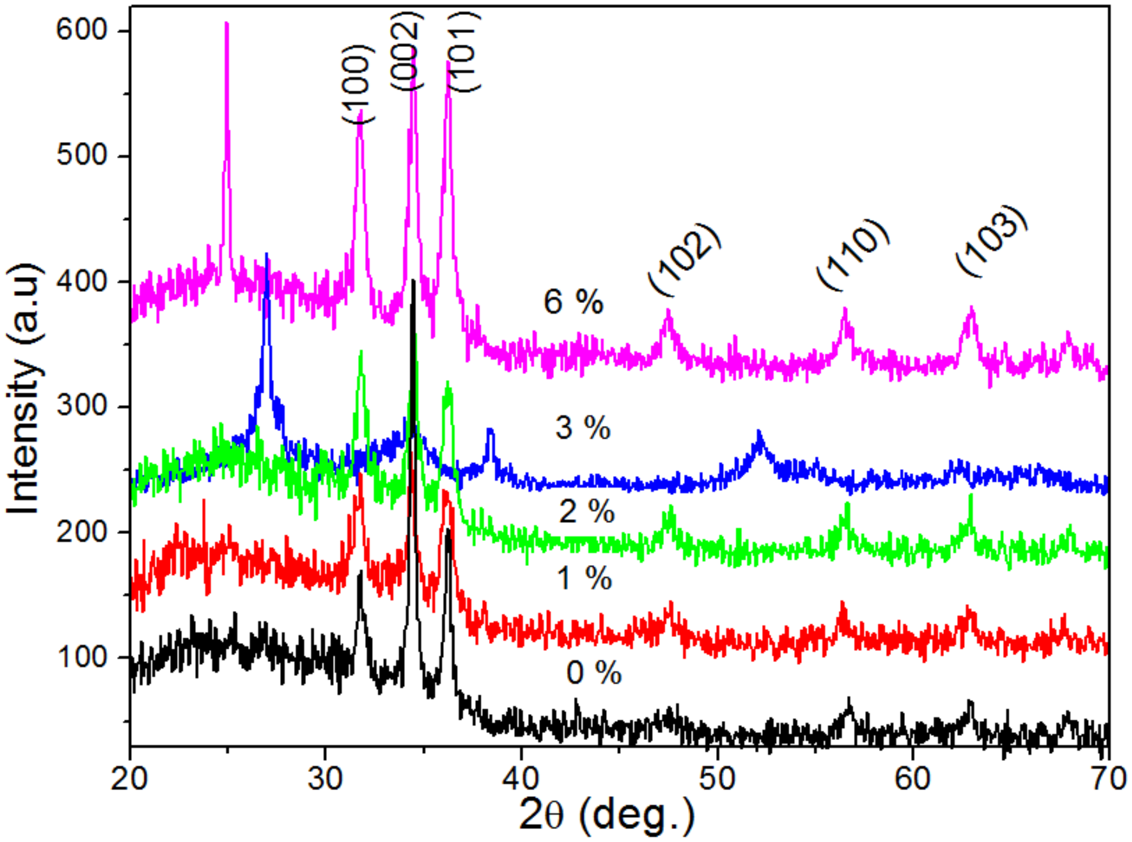

Figure 53:The XRD spectra of Ni- doped ZnO thin films with various Ni contents.

The XRD patterns of the obtained thin films at 0, 1, 2, 3, and 6 at % doping levels showed in figure53. all the patterns exhibit six diffraction peaks around 2θ ~ 32°, 34°, 36°, 47°, 57°, and 63° corresponding to (100), (002), (101), (102), (110), and (103) diffraction peaks of the ZnO crystal structure had been noted. (100), (002), and (101) are the highest peaks, which indicates that the ZnO thin films doped by nickel have a polycrystalline structure like the hexagonal wurtzite. When the doping level increase to 3 at %, the deposited layer has other peaks, located for 6 at % Ni at 2θ ~ 24° (see Fig.54) and for 3 at % Ni at 2θ ~ 38° and 52° (see Fig.54) [5, 6] To compare the orientations of (100), (002), and (101) peaks, The texture coefficient TC(hkl) was calculated from the intensities of these peaks as expressed in [7] (II.7)

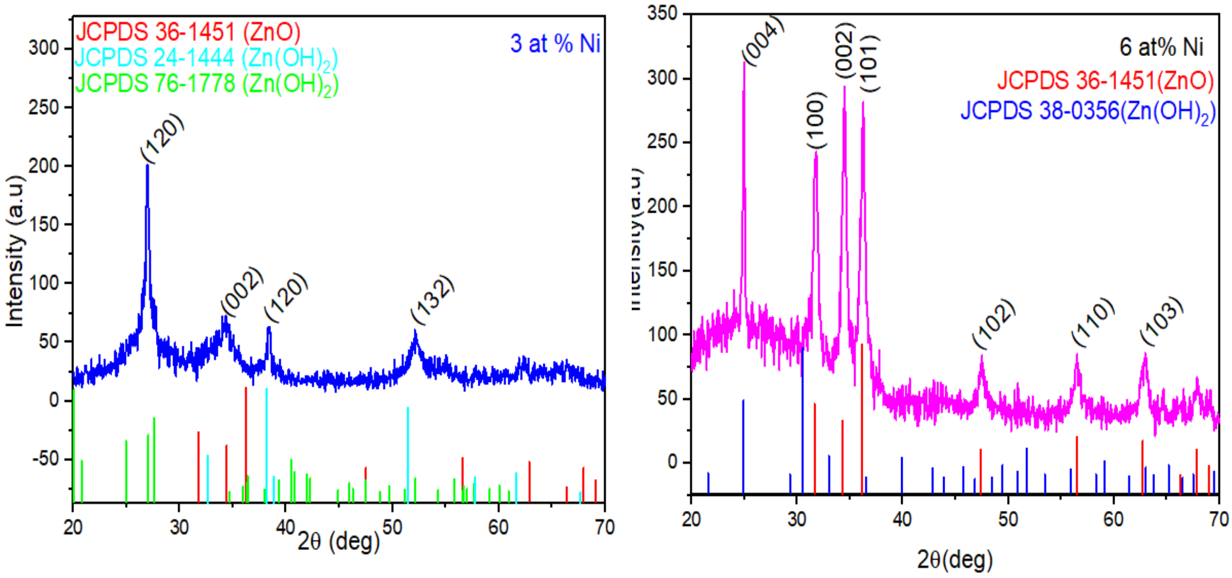

Figure 54:The XRD spectra of Ni-doped ZnO thin film at 3 and 6 at % Ni.

Texture value for the three peaks of Ni-doped ZnO thin films is presented in Fig 55.

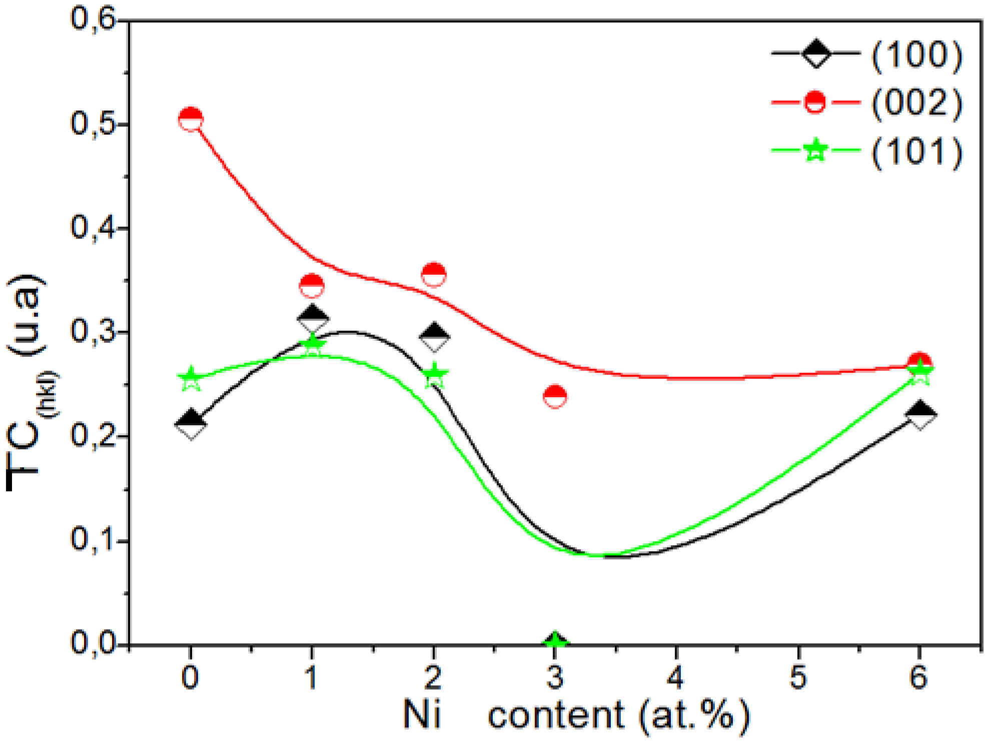

Figure 55:The variation of TC(hkl) of (101), (002) and (101) peaks in Ni- doped ZnO thin films with various Ni contents.

As shown in fig 55, the highest peak is (002), which means that the samples favorites c-axis as highly preferential orientation. However, the intensity of these diffraction peaks increases significantly, with the increase of doping content, due to crystallinity enhancement because of full width at half-maximum (FWHM) lattice. On the other hand, the crystallite size of Ni-doped ZnO thin films calculated according to the Scherrer equation (II.6), to give information about detailed structure

From Eq. (II.6), the crystallite size of (100), (002), and (101) planes with variable doping levels is shown in Fig 56.

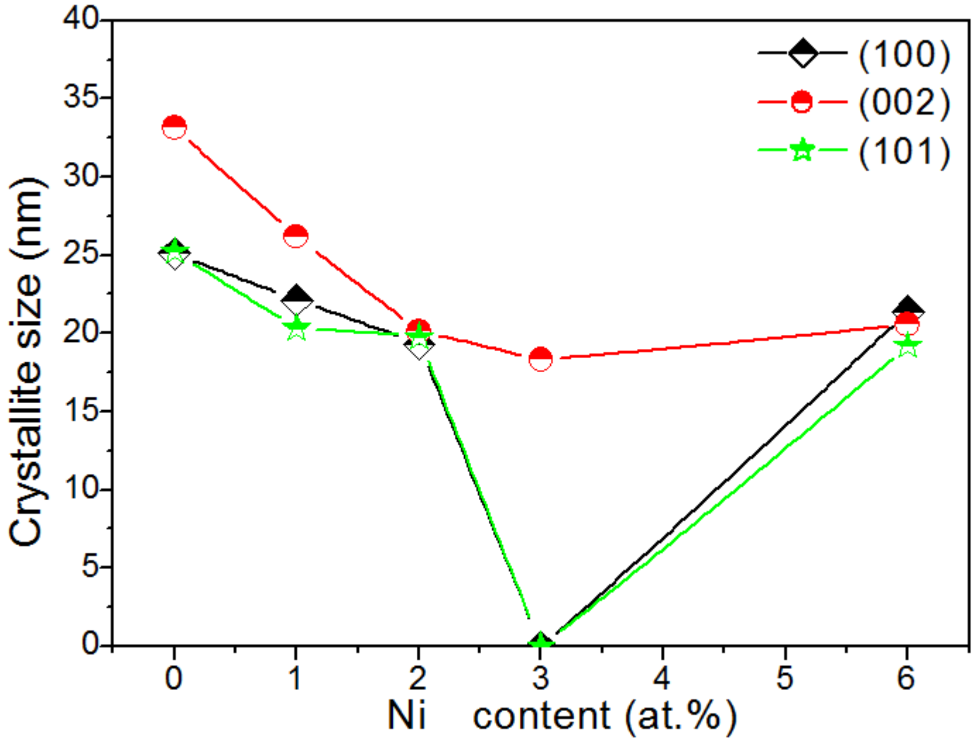

Figure 56:The variation of crystallite size of (100), (002), and (101) planes in Ni-doped ZnO thin films versus Ni content.

These experimental results in that the crystallite sizes of Ni-doped ZnO thin films decrease greatly with the increase of doping level due to the oxygen diffusion with deposition of the films. The dislocation density(δ) of the Ni-doped ZnO thin films was calculated using the following formula[105, 106]:

$$\delta = \frac{1}{G^2} \qquad \text{(III.3)}$$

Figure 57 shows the dislocation density variation as a function of Ni content, it is calculated for (100),(002), and (101) planes. We have also observed that the dislocation density values decrease greatly with increasing Ni content. It was shown that the film deposited with 3 at % has a maximum value.

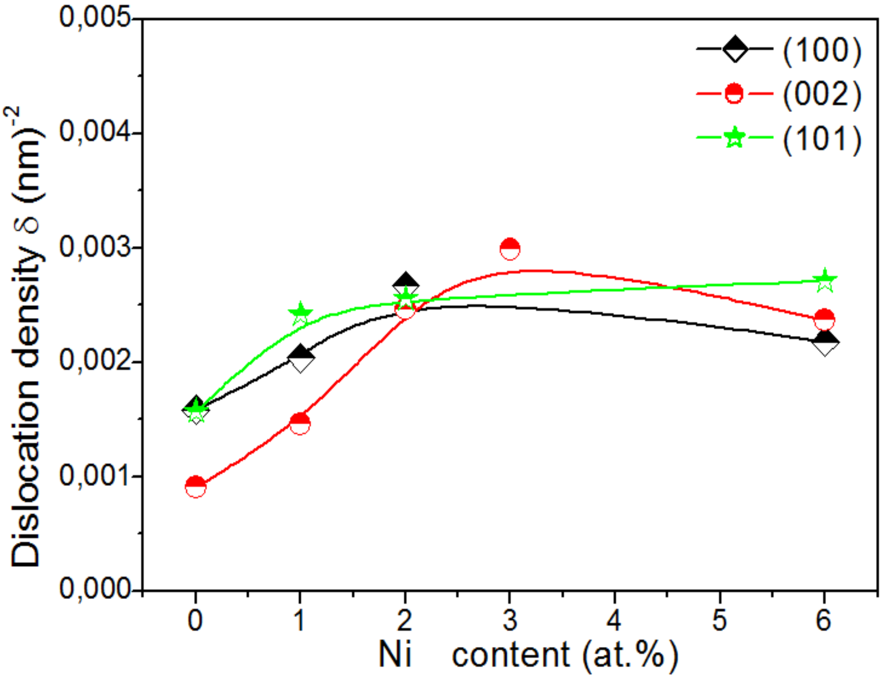

Figure 57:The variation of dislocation density of (100), (002), and (101) planes in Ni-doped Zn thin films versus Ni content.

III.2.3.2 Optical Characteristics of Ni-Doped ZnO Thin Films

The optical transmission spectra of all films in the spectral range of 300–900 nm wavelengths with different Ni contents are shown in Fig.58.

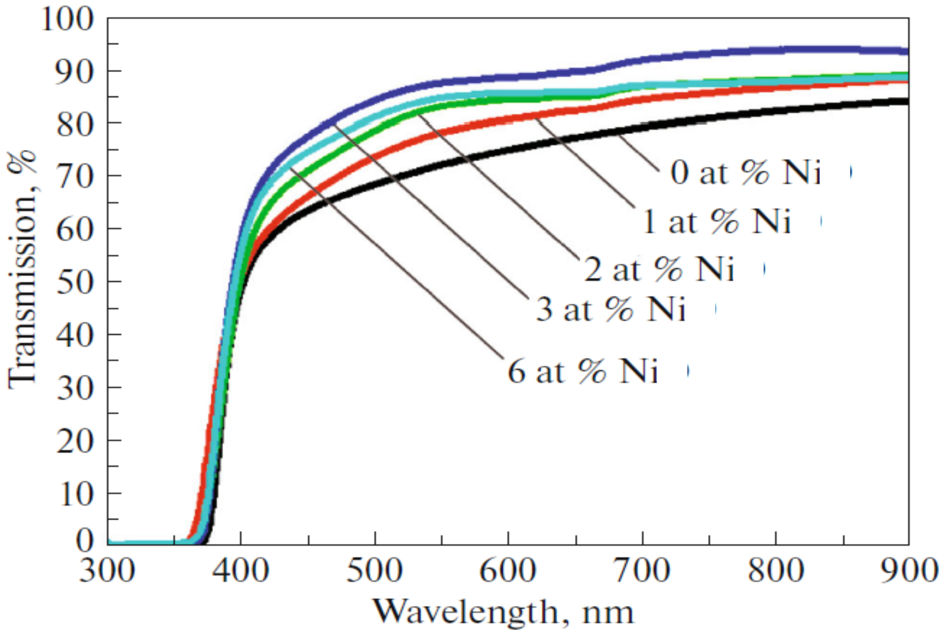

Figure 58:The optical transmission of Ni-doped ZnO thin films with various Ni contents.

The Ni-doped ZnO thin films exhibit an average optical transmission of about 85% in the visible region. However, the transmission was improved with increasing of Ni content until 3 at% then decreased. After 1 at % Ni, the transmission was shifted toward longer wavelengths, the Ni-doped ZnO thin films displaying the smallest band gap energy. The optical band gap (E_g) of Ni-doped ZnO thin films was derived assuming allowed direct transitions between the absorption edge of the valence band and conduction band. It is determined by the transmission spectra according to the equation (II.8) [107].

The optical band gap E_g was obtained by extrapolating the linear portion of the plot $(Ah\nu)^2$versus $h\nu$ to $A = 0$ (see Fig.59).

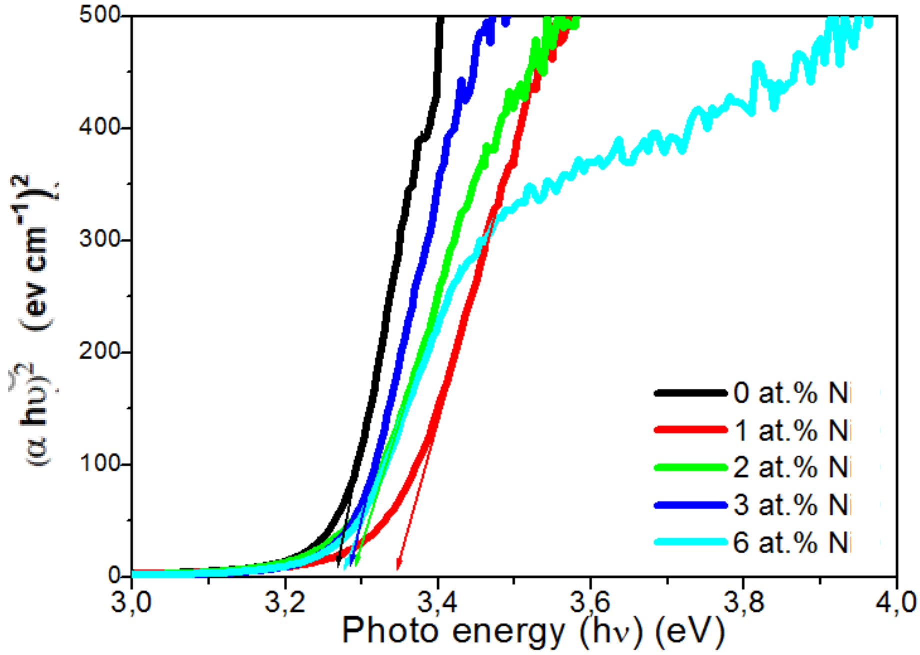

Figure 59:The variation of $(Ah\nu)^2$ as a function of ($h\nu$) for each films thickness for calculate optical energy.for Ni-doped ZnO with various Ni content.

The Urbach energy (E_U) of Ni-doped ZnO thin films also was calculated by the transmission spectra using the equation(II.9)[62]. The Urbach energy is determined by the curves of lnA as a function of photon energy hν, which is presented in Fig.60.

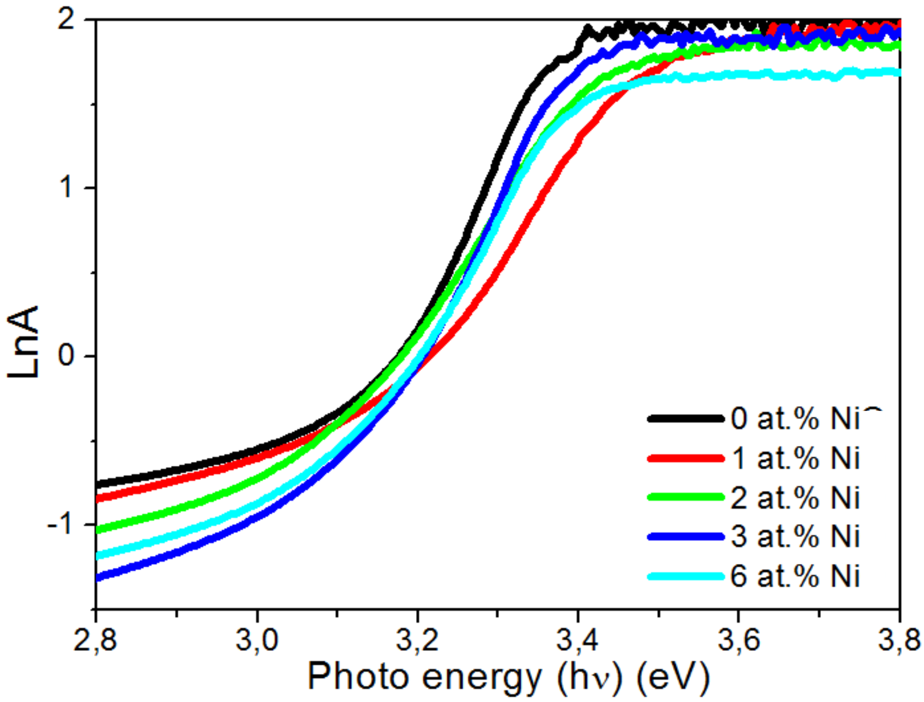

Figure 60:The variation of(lnA) versus(hν)for estimated Urbach energy for Ni-doped ZnO with various Ni content.

The experimental values of the optical gap energy and the Urbach energy of Ni-doped ZnO thin films at various Ni contents are shown in Fig.61.

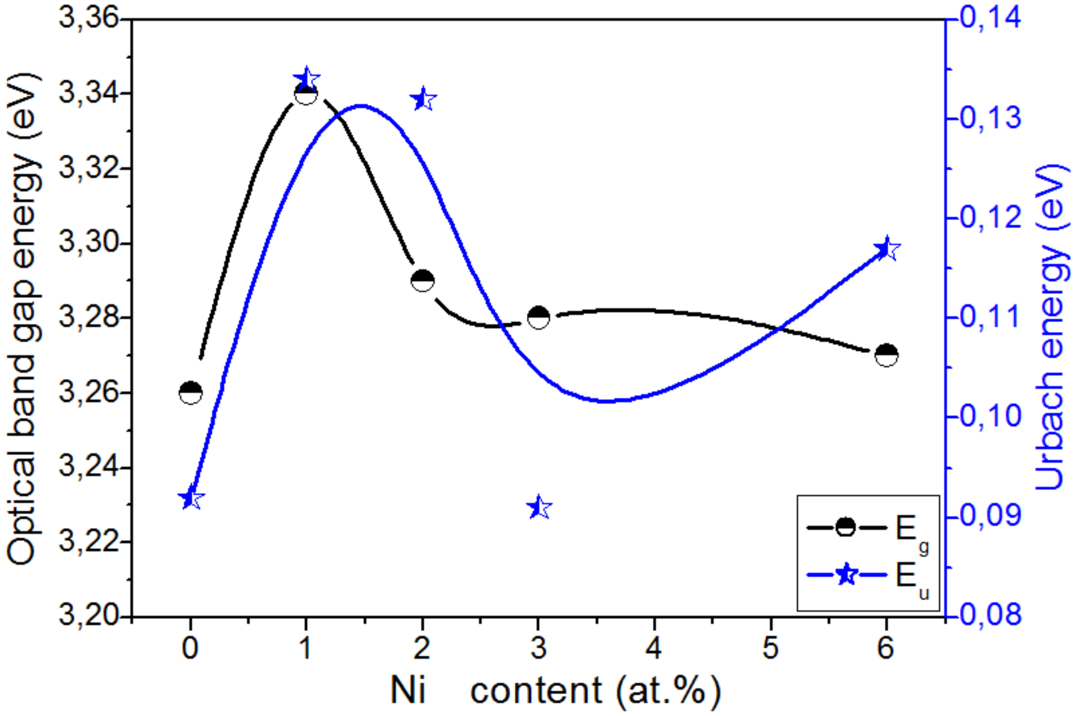

Figure 61:The variation of optical band gap Eg and Urbach energy E_u of Ni-doped ZnO thin films versus Ni content.

Firstly, the optical band gap energy increased from 0 to 1 at % Ni. With further Ni content increase, the band gap decreases to minimum value obtained as 3.27 eV for deposit sample with 6 at % Ni (see Table.6). Secondly, we have observed an increase, a decrease in the Urbach energy with the increase of Ni content. The increase can be explained by decreases of crystallite size (see Fig.56). As to the results of the disorder, it can be found that the thin film prepared with 3 at % Ni has a minimum disorder with few defects. However, the decrease of the optical gap with the growth of Ni contents can be explained by the oxygen cooperation in the formation of ZnO thin films.

Table 6:The variation of the optical band gap energy, Urbach energy, electrical conductivity, and film thickness of Ni-doped ZnO thin films

[Ni]/[ZnO] ration	Optical gap energy E_g (ev)	Urbach energy E_u (ev)	Conductivity σ $(\Omega.cm)^{-1}$	Film thickness d (nm)
0%	3.26	0,092	0,01638	149,65
1%	3.34	0,134	0,02074	134,66
2%	3.29	0,132	0,21781	126,62
3%	3.28	0,091	1,08795	101,4
6%	3.27	0,117	0,04159	126,3

III.2.3.3 Electrical Properties Ni-Doped ZnO Thin Films

Figure 62 shows the variation of the electrical conductivity and film thickness of Ni-doped ZnO thin films as a function of Ni content. As a result, by increasing Ni content, we observe an increase of electrical conductivity σ up to maximum value obtained at 3 at % Ni, which is 0.042 $(\Omega.cm)^{-1}$(see Table.6). The increase was caused by oxygen cooperation in the formation of ZnO thin films. The changes in the film thickness from 2 to 3 at % Ni can be explained by the formation of β-$Ni(OH)_2$ phase.

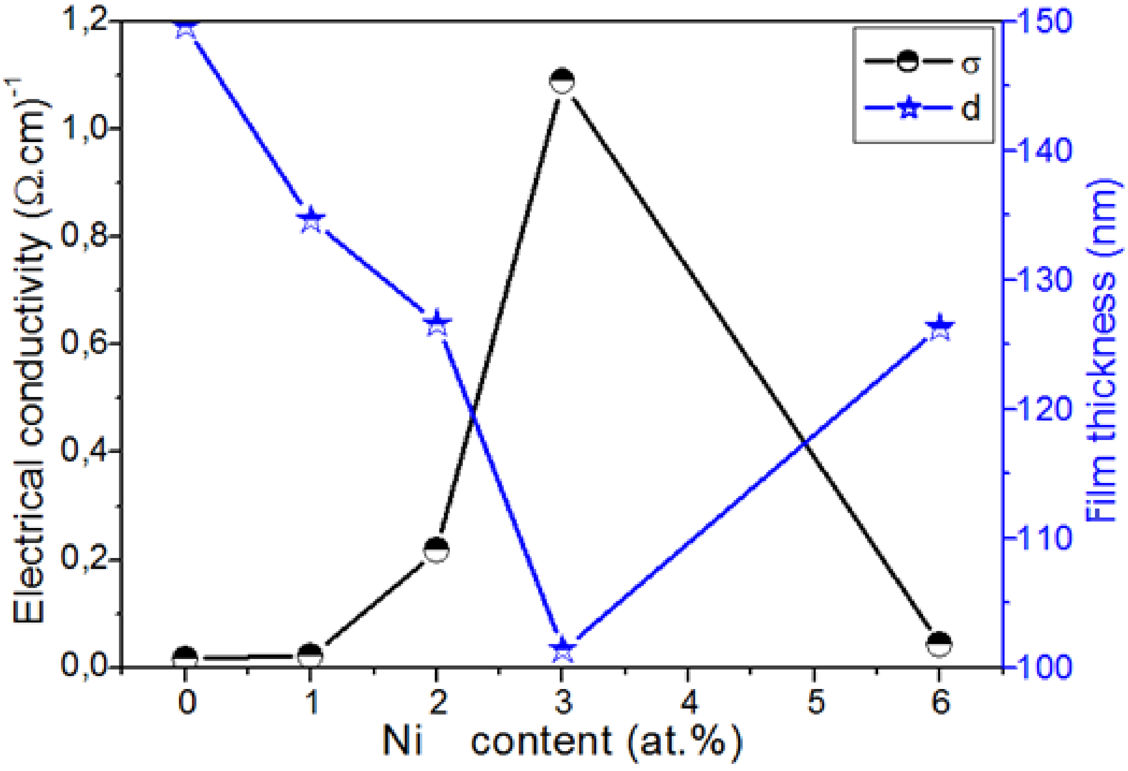

Figure 62: The variation of electrical conductivity and film thickness of Ni-doped ZnO thin films versus Ni content

III.3 Conclusion

In this chapter, we elaborated ZnO thin films with variation of substrate temperature, deposition rate and dopant using spray pyrolysis technique and solar heating ,then we studied the effect of deposition parameters on the structural, optical and electrical properties of samples prepared .The XRD patterns showed that the structural of all samples is polycrystalline structure .The diffraction peaks (100),(002) and (101) are the highest ones, the crystalline size is increased by increasing substrate temperatures and deposition rate and decreases by increasing the doping in the (ZnO) samples .From the transmittance spectra, for all samples it was exhibited an average optical transmission of about 85% in the visible region. it decreases by increasing the deposition time and substrate temperature of ZnO thin deposited, or by increasing the percentage of doping with Ni the transmittance increases. The gap energy decreases with the variation of all deposition parameters that has been mentioned, it was observed that the electrical conductivity increases with increasing of deposition rate and Ni content and by increasing the substrate temperature de conductivity decreases.

Chapter IV

Results of NiO Thin Films

IV.1 Introduction

Nickel oxide NiO is one of the parts of this family of TCO, its good adsorptive properties and chemical stability; it can be deposited onto glass, ceramics, oxides, and substrate materials of other types. In this chapter The NiO thin films will be deposited by spray pneumatic technique on a glass substrate at various NiO concentrations 0.05, 0.10 and 0.15 mol.l^{-1}. The NiO thin films were characterized by various methods likely X-ray diffraction, ultraviolet-visible spectrophotometer, and four points methods.

IV.2 Characterizations of prepared NiO thin films

IV.2.1 Effect of deposition rate

IV.2.1.1 The crystalline structure of NiO thin films

The effect of NiO concentration on the crystal structure and preferred orientations of the sprayed NiO thin films was characterized by the XRD technique. Figure.63 shows the XRD patterns of NiO thin films deposited with various concentrations of 0.05, 0.10 and 0.15 mol.l^{-1}.

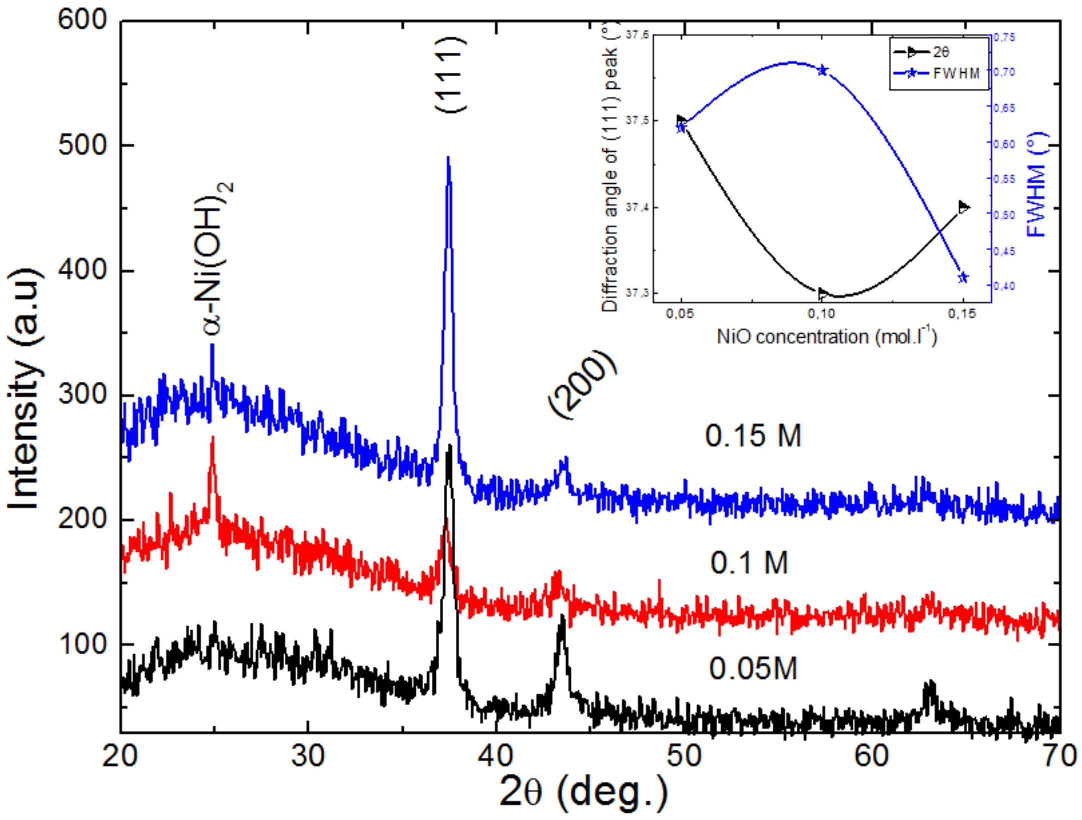

Figure 63:X-ray diffraction spectra of NiO thin films at different NiO concentrations. The inset shows the variations of the diffraction angle and the FWHM of the (111)

As the first result, All the films exhibited two diffraction peaks at 2θ = 37 and 44° related to (111) and (200) planes of NiO phase, indicating NiO thin films are polycrystalline cubic structure. The obtained crystalline structure of NiO thin films has a strong peak of the (111) crystal plane. It can be seen that the (111) peak of deposited NiO thin film with 0.15 mol.l^{-1} has a higher intensity, which confirmed the improvement of the crystalline quality and the reduction of defects in the crystal structure. The inset of Figure.63 shows the variations of diffraction angle and FWHM of the (111) diffraction. The smaller diffraction angle of the position peak was obtained for 0.1 mol.l^{-1},indicating the increase in the interplanar spacing d_{111}. However, the maximum value of the FWHM of the (111) peak measured for 0.1 mol.l^{-1}. On the other hand, we have observed at 2θ = 25° in the XRD patterns of NiO thin films a new phase, which it is related to α-Ni(OH)$_2$ due to the water solvent with preparation.

The crystallite size G of (111) diffraction peak of the NiO thin films was calculated using the Scherer's equation (II.6) [108, 109].these variations are presented in Table.7.

Figure.64 shows the variations of the crystallite size and strain of the (101) diffraction peak as a function of NiO concentration. It can be seen, the crystallite size has a slight change estimated at 2.0 nm for 0.05 and 0.10 mol.l^{-1} (see Table.7). And when the increase of the NiO concentration from 0.1 to 0.15 mol.l^{-1}, the crystallite size greatly increased from 11.97 to 20.45 nm, which may be due to the improvement of the crystalline quality. However, we have observed that the crystallite size was related to the FWHM value, when the minimum crystallite size corresponded to the higher FWHM, and the decrease of FWHM due to the increase in the peak intensity. The strain has a minimum value at 0.1M due to the decrease in the lattice parameter of NiO.

Table 7:The Diffraction angle, FWHM crystallite sizes, lattice parameter and strain of the (111) plane in NiO thin films as a function of NiO concentration

NiO concentration (mol.l^{-1})	**Diffraction angle 2θ (°)**	**FWHM β (deg)**	**Crystallite size G (nm)**	**Latticeparameter a (nm)**	**Strain ε (nm)**
0.05	37.5	0.62	13.53	0.4151	0.627
0.10	37.3	0.70	11.98	0.4172	0.114
0.15	37.4	0.41	20.46	0.4161	0.371

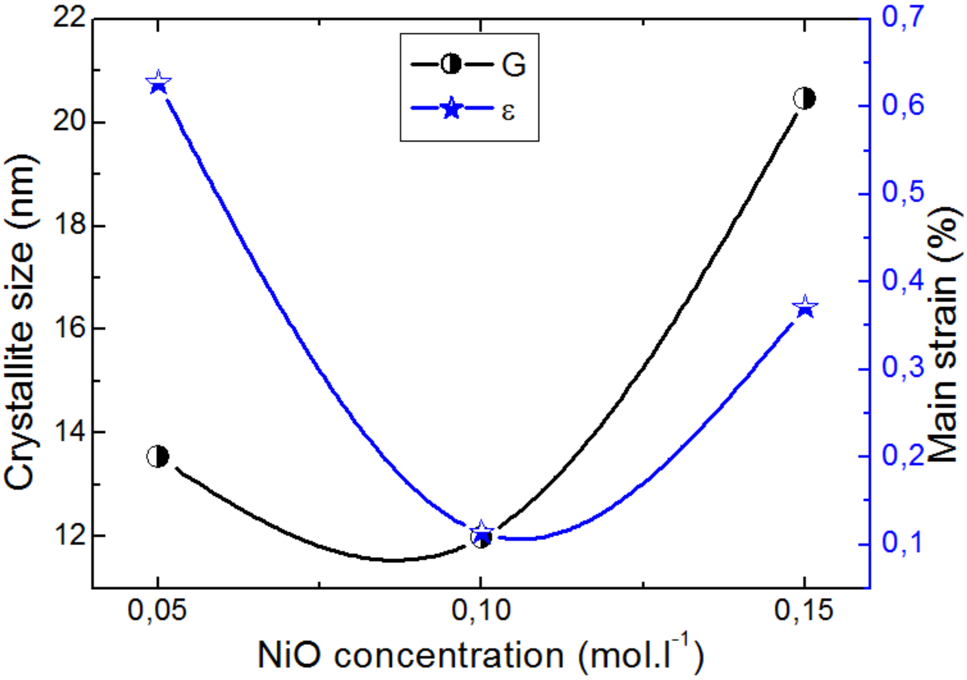

Figure 64:The variations of the crystallite size and the strain of NiO thin films as a function of NiO concentration

IV.2.1.2 Optical Characteristics of NiO Thin Films

The optical transmission of NiO thin films at different NiO concentrations as shown in Figure.65.

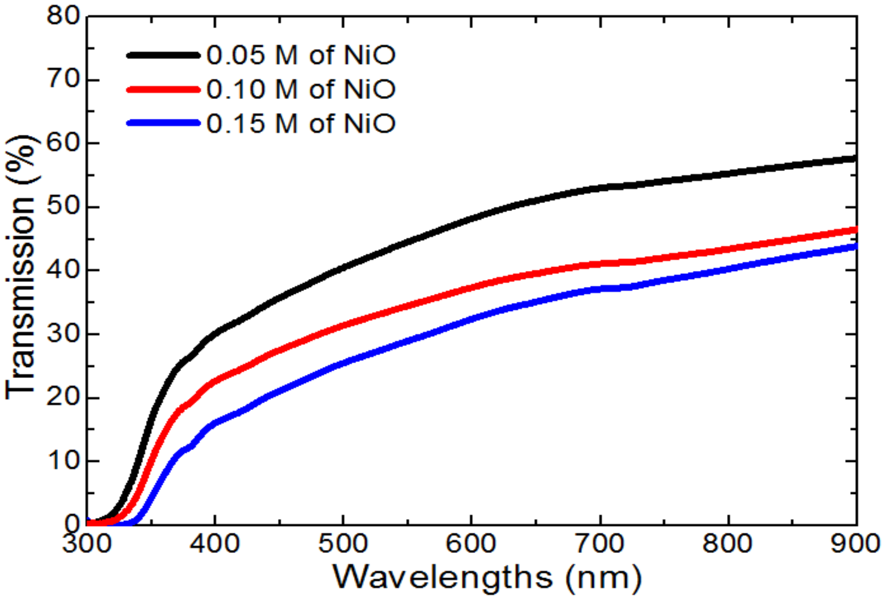

Figure 65:Transmission spectra of NiO thin films as a function of NiO concentration

As the NiO concentration increase, the transmission was decreased due to the increase in the film thickness. But the NiO thin films have a good transmission with comparing by other NiO thin films[110, 111], they found that the NiO thin films have a low transmission about of 40% in the visible. The region of strong absorbance was observed between λ = 330 to 380 nm, in this region, the transmission decreased due to the excitation and the migration of the electrons from the valence band to the conduction band. It is clearly observed that the absorption edge shifted to the low wavelength can be found that the band gap was increased. The calculation of the optical band gap energy is a major factor in determining the electrical conductivity of the thin films, which based on optical transmission. It was calculated from the classical method by the extrapolation of the curve at$A = 0$[112], which represented to the drawn of the $(Ah\upsilon)^2$ as a function of hυ (see Figure 66) using the equation(II.8)[113, 114] (see Table .8).

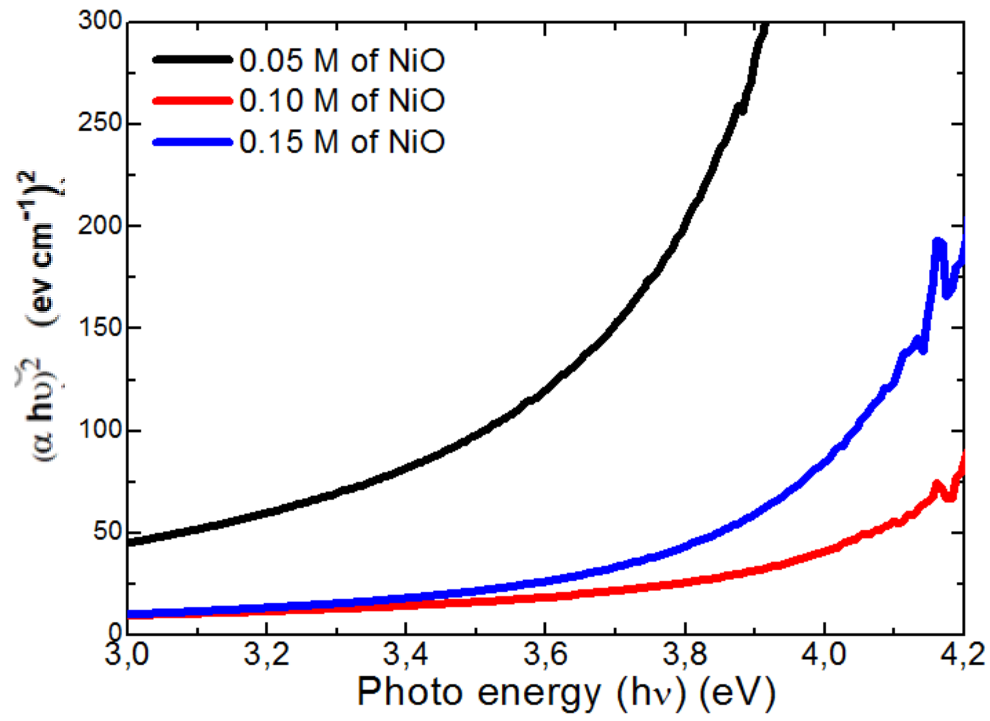

Figure 66:The typical variation of $(Ah\nu)^2$ vs. photon energy all deposited NiO thin film as a function of NiO concentration

On the other hand, the disorder in the NiO thin films was characterized by the Urbach energy (E_u) has been calculated by the expression(II.9)[115].

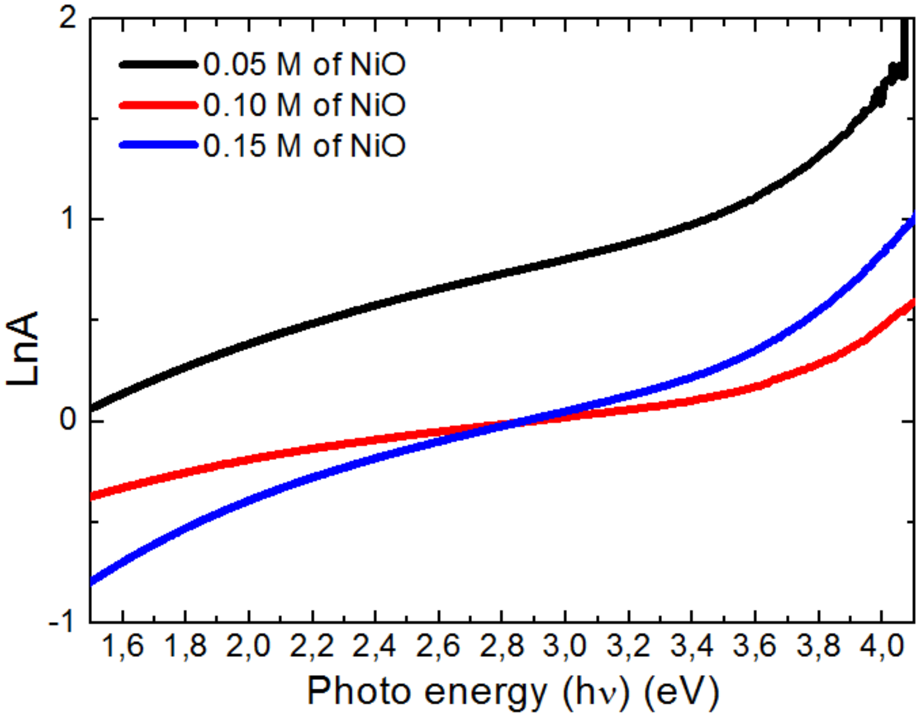

Figure 67:.The typical variation ofLnA vs. photon energy all deposited NiO thin film as a function of NiO concentration

The values are presented in Table 8. Figure.67 shows the drawn of LnA as a function of photon energy hυ for deducing the Urbach energy.

Table 8:The variation of optical band gap energy, Urbach energy and electrical conductivity as a function of NiO concentration

NiO concentration ($mol.l^{-1}$)	**Optical gap energy E_g (eV)**	**Urbachenergy E_u (eV)**	**electricalconductivity σ (nm)**
0.05	3,54	0,193	0,063
0.10	3,68	0,214	0,169
0.15	3,76	0,322	0,081

Figure.68 shows the variations of optical band gap energy and Urbach energy of the NiO thin films, the variables are presented in Table.8. By an increase in the NiO concentration from 0.05 to 0.15 mol.l^{-1}, found an increase of the optical band gap with the increase of the Urbach energy, this increase can be explain by the effect of stage confinement car the crystalline size very small (about 13 nm). The variation of the optical band gap energy of the NiO thin films was varied from 3.5 to 3.75eV, which is in good agreement with the E_g value of bulk NiO (3.6-4 eV)[116]. But the increase of the Urbach energy can be explained by the decrease of crystallite size and the increase of the strain was presented in Figure 64.

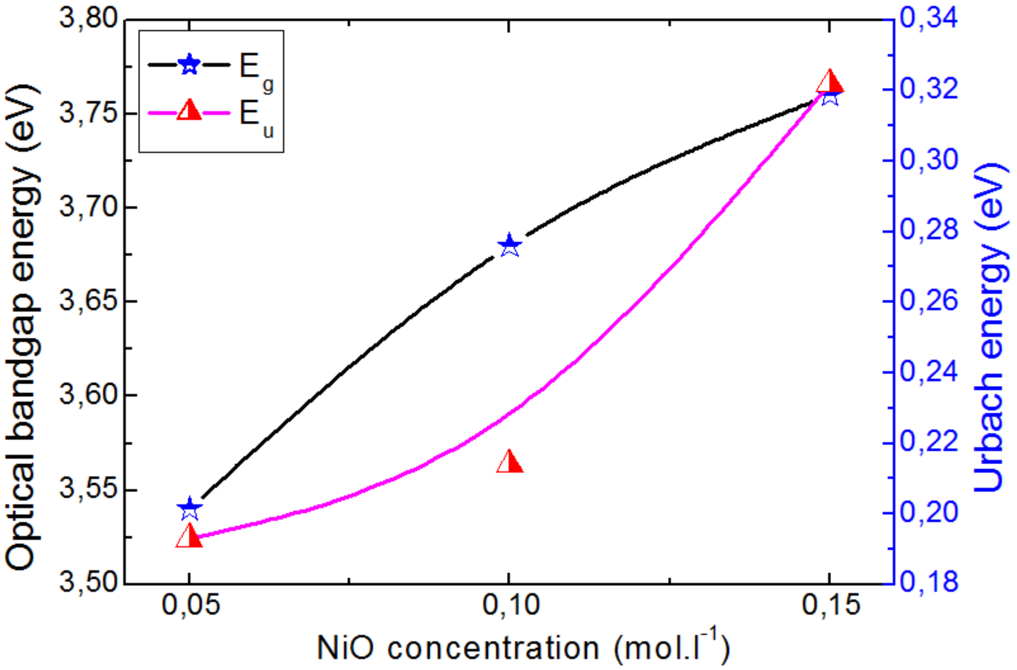

Figure 68:The variations of optical bandgapEg and Urbach energy Eu of NiO thin films with NiO concentration

IV.2.1.3 Electrical Properties of NiO Thin Films

The four-point method was used to calculate the electrical conductivity σ of the NiO thin films, the measurement was based on the sheet resistance R_{sh} ; it is obtained by the following relation:

$$\sigma = \frac{1}{d\mathrm{R_{sh}}} = \frac{1}{\mathrm{d}}\left(\frac{\pi}{\ln(2)}\cdot\frac{\mathrm{V}}{\mathrm{I}}\right)^{-1} \tag{IV.4}$$

where I is the applied current = 0,5.10^{-6} and V is the measurement voltage and d is the film thickness. Figure 69 shows the variation of electrical conductivity of NiO films with different

NiO concentration. As see the electrical conductivity firstly increased from 0.063 to 0.169 $(\Omega.cm)^{-1}$ when NiO concentration increases from 0.05 to 0.10 mol.l^{-1}, than decreased to

0.081 $(\Omega.cm)^{-1}$ at 0.15 mol.l^{-1}.As a result of the compositional changes, especially the formation of nickel vacancies, this leads to p-type conductivity. The increase in the electrical conductivity variation with NiO concentration can be explained by the decrease of crystallite size (see Figure 64).

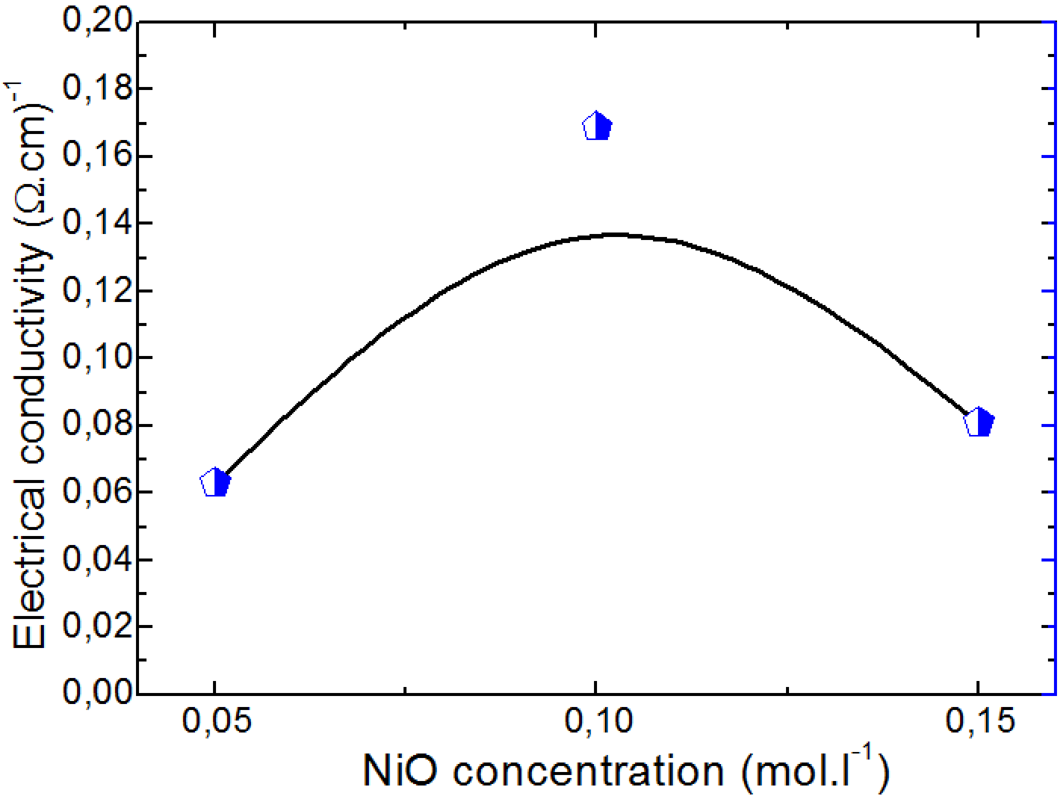

Figure 69:Electrical conductivity of NiO thin films at different NiO concentrations

IV.2.2 The comparative results of our work with other researches

Table 9 presents the comparative results of our work with other researches; we have compared the structural, optical and electrical properties of the nickel oxide thin films. Through these results, it is clear to us that the best values for nickel oxide have been found, which are represented in the crystallite size, optical band gap, Urbach energy and electrical conductivity.

Table 9:The comparative study of the structural, optical and electrical properties of nickel oxide thin films at different conditions

NiO concentration (mol.l^{-1})	**Dep. Temp T (°C)**	**Deposition method**	**Texture**	**Latice parameter a (nm)**	**Crystallite size G (nm)**	**Optical energy E$_g$(eV)**	**Urbach energy E$_u$ (eV)**	**Electrical conductivity (Ω.cm)**	**Rf.**
3%Cu:NiO	300	RF sputtering	Crystalline	0.4208	4.0	3.8835	-	-	[117]
0.10 **0.10**	350 390	Spray pyrolysis	Crystalline	0.416 0.416	5-12 8-13	3.10 3.85	- -	0.035 0.025	[109]
0%Na:NiO **3%Na:NiO**	420	Spray pneumatic	Crystalline	0.4138 0.4166	16.47 18.90	3.62 3.60	0.422 0.312	-	[62]
0.05	350	Spray pyrolysis	Crystalline	0.417	45	3.83	-	-	[116]
0.01	250	Hydro thermal	Crystalline	0.418	6.6	3.1	-	-	[118]
Oxygen flowrate (sccm)	RT	magnétrons puttering	Crystalline	0.4205	8.45	3.41	-	5.10^{-3}	[119]
0.05 **0.10** **0.15**	450	Spray pyrolysis	Crystalline	0.193 0.214 0.322	13.53 11.98 20.46	3.54 3.68 3.76		0.063 0.169 0.081	This work

IV.3 Conclusion

In this chapter we studied The effect of NiO concentration, on structural, optical and electrical properties, As the first result, NiO thin films are polycrystalline cubic structure, the crystallite size has a slight change estimated at 2 nm And when the increase of the NiO concentration from 0.1 to 0.15 mol.l^{-1}, the crystallite size greatly increased from 11.97 to 20.45 nm, As the NiO concentration increase, the transmission was decreased, and it found an increase of the optical band gap, the electrical conductivity firstly increased than decreased whith increasing NiO concentration.

Chapter V

Results of SnO_2 Thin Films

V.1 Introduction

As commonly known, that the SnO_2 thin films properties are significant effected by technique of elaboration and deposition parameters. In the case of spray pyrolysis, the main parameter which is widely influenced on SnO_2 thin films properties is deposition rate which controls the formation of film. In this chapter, SnO_2 thin films have been deposited by spray pyrolysis. Deposition rate effect on structural, optical and electrical properties of SnO_2 films have been investigated

V.2 Characterizations of prepared SnO_2 thin films (Effect of deposition rate)

V.2.1 The crystalline structure of SnO_2 thin films

The crystalline structure of SnO_2 thin films is detected in Figure 70, it is presented the X-ray diffraction variation in the range of 2θ = 20° to 80°. The XRD of SnO_2 thin film presents same diffraction peaks at different diffraction angle are (110), (101), (200), (211), (310) and (112) crystal peaks of SnO_2 at 2θ = 26°, 33°, 38°, 54°, 62° and 66°. After characterized, we have observed that the elaborated SnO_2 thin films have a polycrystalline structure.

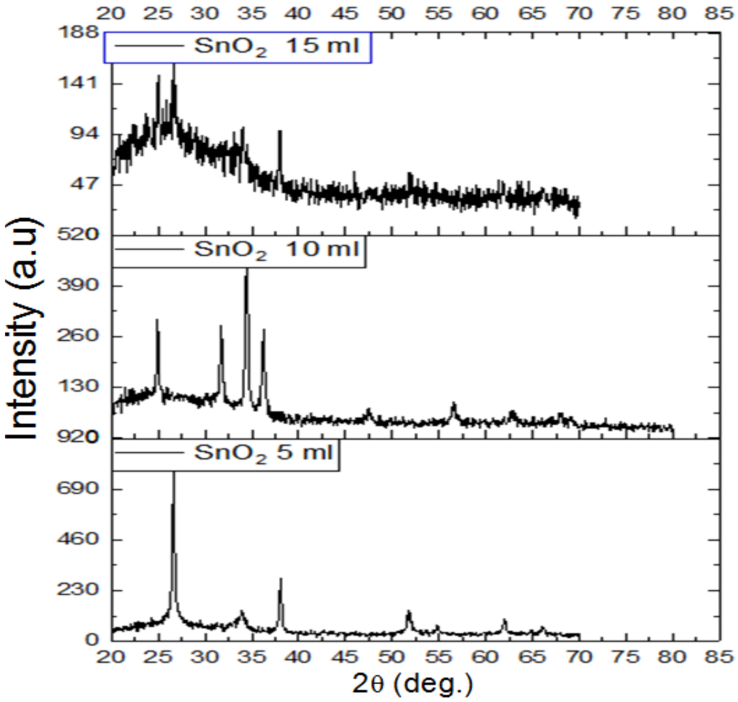

Figure 70:X-ray diffraction spectra of SnO_2 thin films at different deposition rates.

The crystallite size of all deposited SnO_2 thin films was calculated by the Debye-Scherrer formula (II.6)

Reported in the Figure.71 as a function of deposition rate the variation of the average crystallite size of SnO_2 thin films, as seen, the crystallite size increased then decreased with increasing of SnO_2 rate from 32.5 nm for 5 ml to 35.3 nm for 10 ml and 29.6 nm for 15 ml.

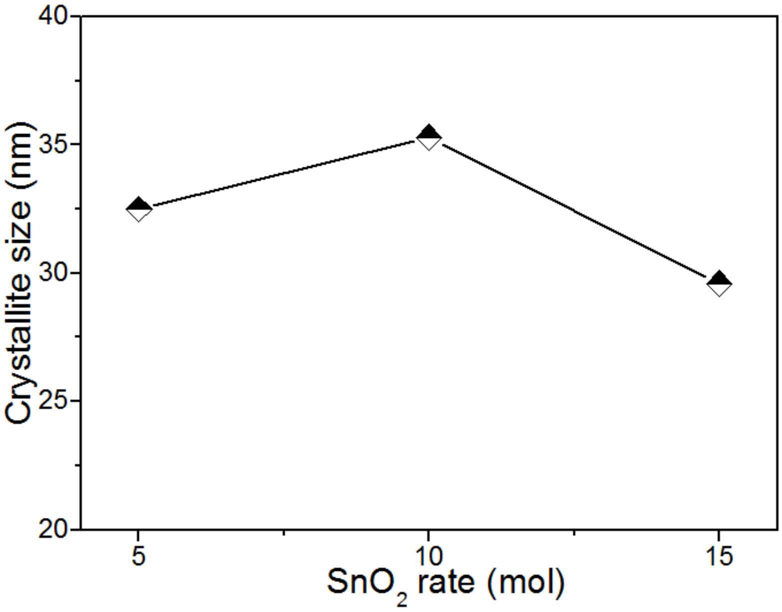

Figure 71:The variation of crystallite size as a function of deposition rate in SnO2 thin films.

V.2.2 Optical Characteristics of SnO_2 Thin Films

In Figure 72, the variation of optical transmittance of elaborated SnO_2 thin films have been presented as a function of the longer of the wavelength in the range of 300–900 nm. As seen from these spectra's the transmittance of SnO_2 thin films were decreased and increased with increasing SnO_2 rate in the visible region, the maximum transmittance of SnO_2 thin film was obtained for 15 ml.

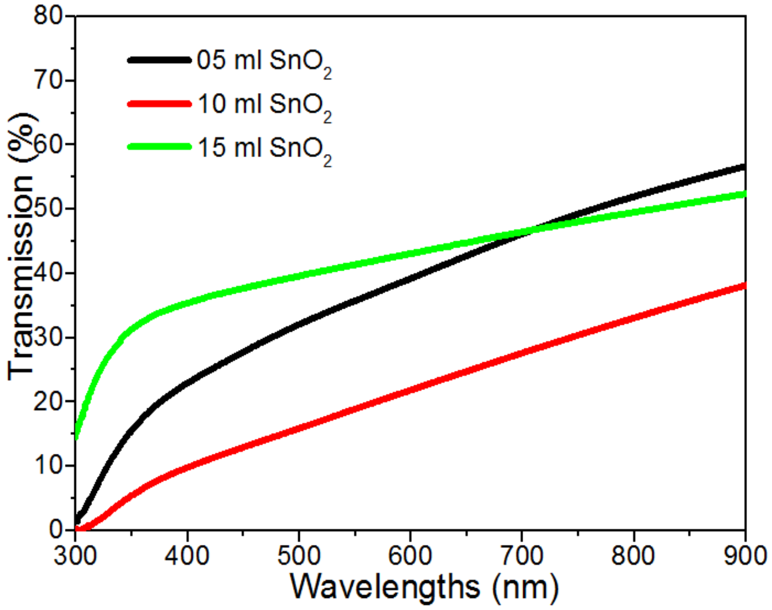

Figure 72:Transmission spectra of SnO2 thin films as a function of deposition rate.

The optical bandgap energy of fabricated thin films of SnO_2 have been derived from the direct transitions of inter band in the valence band and conduction band, it was determined by the equation (II.8)

Figure.73 shows the variation of the optical bandgap energy of fabricated SnO_2 thin films at several SnO_2 rates. As seen, the optical bandgap energy decreased with increasing of SnO_2 rate until10 ml then increased.

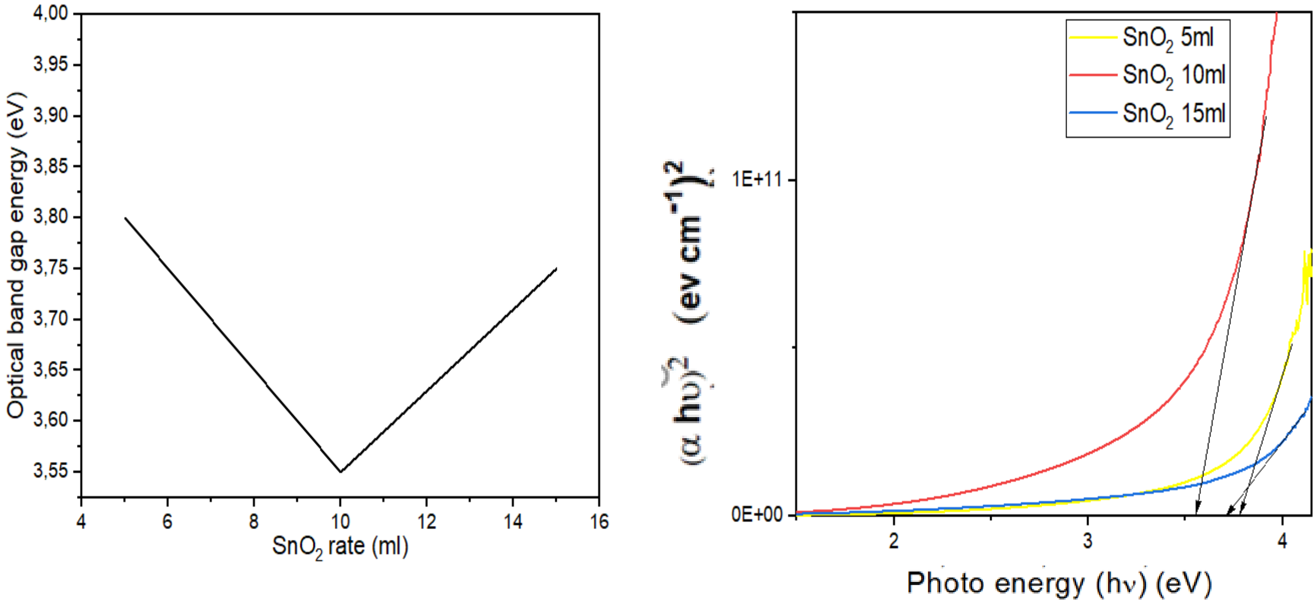

Figure 73:The variation of optical band gap Eg of SnO_2 thin films with deposition rate.

V.2.3 Electrical Properties of SnO_2 Thin Films

The electrical characterization as the conductivity of fabricated SnO_2thin films is shown in Figure.74, as seen, the electrical conductivity was increased from 0.01 $(\Omega.cm)^{-1}$ for 05 ml of SnO_2 to 0.06 (Ω.cm) for 15 ml of SnO_2, it is comparable with the variation of the crystallite size (see Figure.68) and optical band gap energy (see Figure 73). The decrease of electrical conductivity of SnO_2thin films caused by the oxygen vacancy and the increase can be linked by the oxygen diffusion.

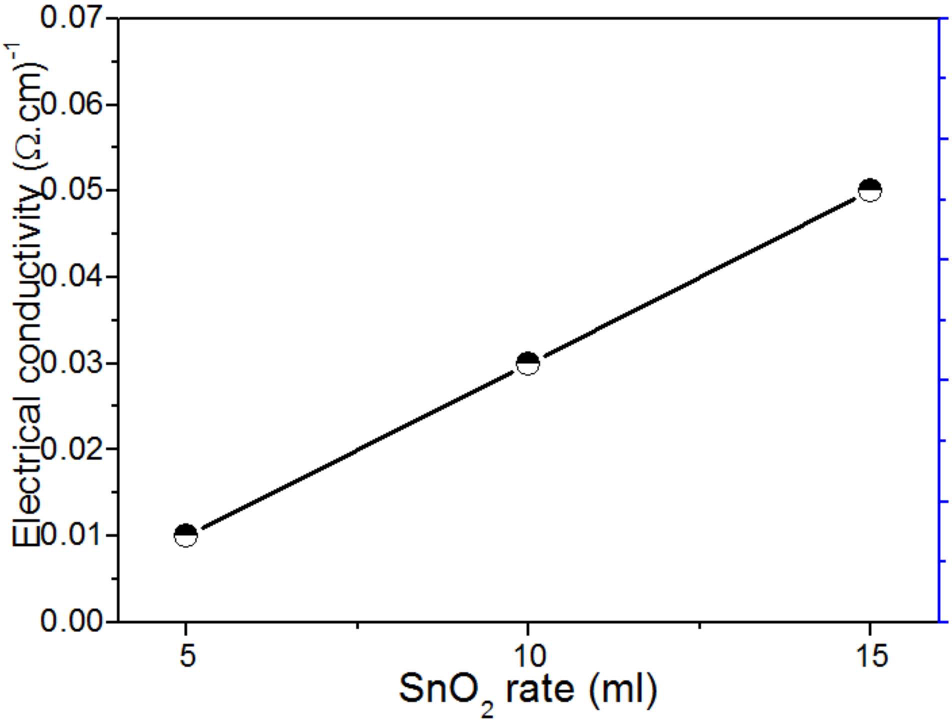

Figure 74:Electrical conductivity of SnO2thin films at different deposition rate.

V.3 Conclusion

in this chapter we elaborated SnO_2 thin films with variation of the effect of deposition rate (5,10,15ml),the XRD patterns shows that the elaborated SnO_2 thin films have a polycrystalline structure. the crystallite size increased until reached the value 35,3 nm then decreased, the transmittance of SnO_2 thin films were decreased then increased with increasing of deposition rate in the visible region, the maximum transmittance of SnO_2 thin film was obtained for 15 ml. the optical band gap energy increased with increasing of SnO_2 rate, the electrical conductivity was increased from 0.01 $(\Omega.cm)^{-1}$ to 0.06 $(\Omega.cm)^{-1}$ with the increase of deposition rate.

General Conclusion

General conclusion

In this thesis, in the first chapter, we talked about the solar energies, Algeria's fortune, with this energy, and its applications in different field namely its use in substrate heating. After that the thin films was defined. Bibliographic study of zinc, nickel, and tin oxides was undertaken with some applications of those oxides layers. As last part of this chapter, thin film preparation techniques were exposed and it was focused on the method of spray pyrolysis. After, in 2nd chapter the experimental montage of a homemade solar spray pyrolysis system was described carefully, where all its components were explained such as the concentrator, air compressor, atomizer, receiver (substrate, holder), multimeter and thermocouple, then we showed how the concentrator heats the substrates. After that we talked about experimental details in which we discussed the procedure of preparation of all types of oxides. Zinc acetate dehydrate 0.1M ($Zn(CH_3COO)_2$, $2H_2O$), nickel chloride hexahydrate 0.1 M ($NiCl_2$, $6H_2O$) and 0.1 M of the Tin(II) chloride dihydrate $SnCl_4.2H_2O$ were used to prepare oxides solutions. Then, we provided the techniques used for the characterization of our thin films such as X-ray diffraction (DRX),UV-Visible spectroscopy, four-point measurement.

The most important results obtained were the outcome of chapter 3,4 and 5 which can be summarized as follows:

The ZnO thin films were deposited on a glass substrate of course by using spray pyrolysis technique and solar energy as source of heat. As first series of elaborated ZnO, the effect of deposition temperature (350, 400 and 450 °C) on structural, optical and electrical properties was investigated. Polycrystalline ZnO films with a hexagonal wurtzite structure under a strong (101) preferred orientation were observed at all sprayed films with maximum crystallite size of 15.19 nm via spraying film at 450°C. The ZnO thin films have good transparency which is about 85%. The band gap energy varies from 3.28 to 3.31 eV and it was affected by deposition temperature, it was shown that the ZnO thin film prepared at 450°C has less disorder with few defects. The ZnO film deposited at 450 °C have a lowest electrical resistivity which was of about 0.064 $(\Omega.cm)^{-1}$.

The second series of elaborated ZnO, the impact of solution amount on deposition of ZnO was studied. The XRD results show that the films are polycrystalline with a hexagonal wurtzite and the (002) plan was the preferred orientation. The crystallite size increases until reached 23.43 nm then decrease to 16.72nm which, perhaps, is due to crystallinity case. Optical proprieties show that the transmittance decrease when the deposition time (amount of solution) increase; it means with increasing of the film thickness. The values of band gap energy and urbach energy change oppositely and the smallest recorded Eg value is 3.28eV, where the urbach energy is 190.0meV, and the deposited solution corresponds to 13 ml. The low result of the electrical resistivity (0.01Ωcm^{-1}) is achieved at highest value of crystallite size.

For the third serie of zinc oxide, the Ni-doped ZnO thin films were successfully deposited on a glass substrate by the cited method, at 450°C. The effect of Ni doping on structural, optical, and electrical properties of ZnO thin films was investigated. The followings conclusions from Ni-doped ZnO thin films are drawn as follow:

- XRD patterns of Ni-doped ZnO thin films indicate that the obtaining ZnO thin films are polycrystalline with (100), (002), and (101) highest peaks of ZnO phase. However, $\alpha Ni(OH)_2$ and β-$Ni(OH)_2$ were observed at 6 and 3 at % Ni, respectively. The crystalline structure was improved for doped thin films, the crystallite size decreased by increasing the Ni content up to 6 at % Ni.
- All thin films have a high transmission in the visible region of about 85%. The optical band gap energy increased from 3.26 eV for 0% to 3.34 eV for1 at %Ni, and then decreased to 3.27 eV for 6 at % Ni. The thin film deposited with 3 at % Ni has the lowest value of Urbach energy, 0.091 eV.
- The electrical conductivity of the Ni-doped ZnO films increased greatly from 0.016 $(\Omega\ cm)^{-1}$ for 0 at % Ni to 0.042 $(\Omega\ cm)^{-1}$ for 3 at % Ni. It can be noted that the deposited film with 3 at % Ni is a p-type semiconductor.

NiO thin films were successfully elaborated on the glass substrate by solar spray pneumatic technique on 450°C heated glass substrate. The effect Ni concentration (0.05, 0.10 and 0.15 $mol.l^{-1}$) on structural, optical and electrical properties was investigated. Polycrystalline NiO films with a cubic structure and a strong (111) preferred orientation were observed at all sprayed films with minimum crystallite size of 11.97nm which was attained in the case of sprayed film with 0.1$mol.l^{-1}$. However, α-$Ni(OH)_2$ was observed with spraying 0.15 $mol.l^{-1}$. The NiO thin films have good transparency in the visible region, whereas the band gap energy varies from 3.54 to 3.76eV and it was affected by Ni concentration. It was shown that the NiO thin film prepared with sprayed solution of 0.05 $mol.l^{-1}$ has less disorder. The NiO film deposited with amount of 0.15 $mol.l^{-1}$ has the electrical conductivity was 0.169 $(\Omega.cm)^{-1}$.

With SnO_2 thin films, where they were deposited on a glass substrate by the same method with 0.1 M using tin chloride dehydrate. The effect of amount solution on structural, optical and electrical characterizations of SnO_2 was investigated. Characterized SnO_2 thin films show that the elaborated SnO_2 has a polycrystalline structure with maximum crystallite size of 35.3 nm for 10ml sprayed solution. The transmittance of SnO_2 thin films reveals a fluctuation around 60 % in the visible region: decrease and increase with increasing SnO_2 rate. The optical band gap energy increased with increasing of SnO_2 rate from 3.2 eV for 5 ml to 3.6 eV for 15 ml. The electrical conductivity was increased from 0.01 ($\Omega.cm^{-1}$) for 05 ml of SnO_2 to 0.06 ($\Omega.cm^{-1}$) for 15 ml of SnO_2.

Future works

According to the results of this study, the following future studies are suggested:

- First part is about the prepared thin films can be adapted to gas detection applications due to the existing phase and higher electrical conductivity.
- Second part is the development of the device used, so that it becomes more efficient and accurate and works automatically, as well as the spraying becomes automatic.
- The last part concerns the materials, where other oxides will be sprayed with the improving of depositions conditions to obtain better results.

References

References

1. Shen, C., et al., *Investigating the performance of a novel solar lighting/heating system using spectrum-sensitive nanofluids.* Applied Energy, 2020. **270**: p. 115208.
2. Touaba, O., et al., *Experimental investigation of solar water heater equipped with a solar collector using waste oil as absorber and working fluid.* Solar Energy, 2020. **199**: p. 630-644.
3. Singh, O.K., *Development of a solar cooking system suitable for indoor cooking and its exergy and enviroeconomic analyses.* Solar Energy, 2021. **217**: p. 223-234.
4. Aoun, Y., et al., *Study the structural, optical and electrical properties of sprayed Zinc oxide (ZnO) thin films before and after annealing temperature.* Main Group Chemistry, 2015. **14**(1): p. 27-33.
5. AOUN, Y., *Conception et développement d'un four solaire pour l'élaboration des oxydes métalliques-caractérisation des oxydes*. 2016, Université Mohamed Khider-Biskra.
6. Azarang, M., et al., *Zn-doped PbO nanoparticles (NPs)/fluorine-doped tin oxide (FTO) as photoanode for enhancement of visible-near-infrared (NIR) broad spectral photocurrent application of narrow bandgap nanostructures: SnSe NPs as a case study.* Journal of Applied Physics, 2018. **124**(12): p. 123101.
7. Sharma, D.K., et al., *A review on ZnO: Fundamental properties and applications.* Materials Today: Proceedings, 2020.
8. Ahmed, M.E.M., *Structural and Optical Properties of ZnO Nano-Powder Synthesized by Combustion and Sol-gel Method*. 2018, Sudan University of Science and Technology.
9. Goel, R., R. Jha, and C. Ravikant, *Investigating the structural, electrochemical, and optical properties of p-type spherical nickel oxide (NiO) nanoparticles.* Journal of Physics and Chemistry of Solids, 2020. **144**: p. 109488.
10. Benramache, S., B. Benhaoua, and O. Belahssen, *The crystalline structure, conductivity and optical properties of Co-doped ZnO thin films.* Optik, 2014. **125**(19): p. 5864-5868.
11. Rhodes, C.J., *Solar energy: principles and possibilities.* Science progress, 2010. **93**(1): p. 37-112.
12. Mebrek, N., M.T. Bouziane, and F. Demnati, *Study of the efficiency of a hybrid pumping system (photovoltaic/electric) for better rural setting management.*
13. Bahcall, J.N., M. Pinsonneault, and G. Wasserburg, *Solar models with helium and heavy-element diffusion.* Reviews of Modern Physics, 1995. **67**(4): p. 781.
14. Sultanova, S., et al. *Definitions of useful energy and temperature at the outlet of solar collectors*. in *E3S Web of Conferences*. 2020. EDP Sciences.

15. Eghosa, O.-O. and I. Aniekan, *Angular solar relations analysis of a flat plate solar collector in Benin City metropolis.* International Journal of Engineering and Innovative Research. **2**(2): p. 67-77.

16. Moukhtar, I., et al., *Introduction and Literature Review.* Solar Energy, 2021: p. 1-27.

17. Bouzid, Z. and N. Ghellai, *Overview of solar potential, state of the art and future of photovoltaic installations in Algeria.* International Journal of Renewable Energy Research (IJRER), 2015. **5**(2): p. 427-434.

18. Kalogirou, S.A., *Solar energy engineering: processes and systems*. 2013: Academic Press.

19. Smets, A.H., et al., *Solar Energy: The physics and engineering of photovoltaic conversion, technologies and systems*. 2015: UIT Cambridge.

20. Abood, A.A., *A comprehensive solar angles simulation and calculation using matlab.* International Journal of Energy and Environment, 2015. **6**(4): p. 367.

21. Sahouane, N., et al., *Energy and economic efficiency performance assessment of a 28 kWp photovoltaic grid-connected system under desertic weather conditions in Algerian Sahara.* Renewable Energy, 2019. **143**: p. 1318-1330.

22. خويلدات, et al., *Trends And Policies Of Renewable Energy In Algeria Between Reality And Crucial Future Programs* توجهات وسياسات الطاقة المتجددة في الجزائر بين الواقع و التحديات المستقبلية الحاسمة. 2019.

23. Charrouf, O., et al. *Degradation evaluation of PV modules operating under Northern Saharan environment in Algeria*. in *AIP Conference Proceedings*. 2017. AIP Publishing LLC.

24. Bailek, N., et al., *Optimized fixed tilt for incident solar energy maximization on flat surfaces located in the Algerian Big South.* Sustainable Energy Technologies and Assessments, 2018. **28**: p. 96-102.

25. eddine Boukelia, T. and M.-S. Mecibah, *Parabolic trough solar thermal power plant: Potential, and projects development in Algeria.* Renewable and Sustainable Energy Reviews, 2013. **21**: p. 288-297.

26. Djehad, B., et al. *The sizing of the isolated photovoltaic system (Domestic self-consumption) and economic comparison between the cost of this energy (price of KWh) and different sector*. in *2019 10th International Renewable Energy Congress (IREC)*. 2019. IEEE.

27. Bouraiou, A., et al., *Status of renewable energy potential and utilization in Algeria.* Journal of Cleaner Production, 2020. **246**: p. 119011.

28. Group, T.W.B., *Algeria - Solar Irradiation And PV Power Potential Maps.* the World Bank Group, August 22, 2018.

29. Algerienne, R., *Bedoui inaugure à Ouargla une centrale solaire de Sonatrach d'une capacité de 10 mégawatts.* Radio Algerienne 25/11/2018.

30. Gunther, M. and R. Shahbazfar, *Solar dish technology.* Advanced CSP teaching materials, 2011. **1**: p. 1-63.

31. Chen, A., *The Critical Angle and Percent Efficiency of Parabolic Solar Cookers.* National Science foundation NFS.

32. COMPANY, F., *This Solar Water Heater Tracks The Sun, So You Get More Hot Water.* FASTCOMPANY, 04-15-15.

33. Shi-Ming, Z., et al., *Atomic simulation of SiyHx structure configuration in a-Si: H thin films.* ACTA PHYSICA SINICA, 2020. **69**(7).

34. Zhao, W., D. Liu, and Q. Feng, *Enhancement of salicylhydroxamic acid adsorption by Pb (II) modified hemimorphite surfaces and its effect on floatability.* Minerals Engineering, 2020. **152**: p. 106373.

35. Kupczak, K., et al., *Chemical and Phase Reactions on the Contact between Refractory Materials and Slags, a Case from the 19th Century Zn-Pb Smelter in Ruda Śląska, Poland.* Minerals, 2020. **10**(11): p. 1006.

36. Li, T., et al., *Rocksalt-zincblende–wurtzite mixed-phase ZnO crystals with high activity as photocatalysts for visible-light-driven water splitting.* Frontiers in chemistry, 2020. **8**.

37. Shaba, E., et al., *A critical review of synthesis parameters affecting the properties of zinc oxide nanoparticle and its application in wastewater treatment.* Applied Water Science, 2021. **11**(2): p. 1-41.

38. Borade, P.A., et al., *Role of defects in modulating the near band edge emissions of sub-micron ZnO crystals.* Optical Materials, 2020. **109**: p. 110348.

39. Galdámez-Martinez, A., et al., *Photoluminescence of ZnO nanowires: a review.* Nanomaterials, 2020. **10**(5): p. 857.

40. Shearin, A.M., *Molecule Assisted Hydrothermal Synthesis Of Zinc Oxide Nanomaterials With Possible Applicatios In Solar Energy.* 2016.

41. Benramache, S., et al., *Influence of growth time on crystalline structure, conductivity and optical properties of ZnO thin films.* Journal of Semiconductors, 2013. **34**(2): p. 023001.

42. Tliba, M., et al., *La-doped zno thin films prepared by spray pyrolysis withmoving nozzle: study of physical properties and adsorption ability of the copper.* Dig. J. Nanomater. Biostructures, 2018. **13**(4): p. 991-1002.

43. Rahman, F., *Zinc oxide light-emitting diodes: a review.* Optical Engineering, 2019. **58**(1): p. 010901.

44. فار, et al., *L'effet de la molarité de nickel sur les propriétés des couches minces d'oxyde de nickel NiO élaborées par la technique de spray pyrolyse alimentée par énergie solaire.* 2019.

45. Karmakar, S., et al., *Superior field emission and alternating current conduction mechanisms for grains and grain boundaries in an NiO-[CdO] 2 nanocomposite.* Journal of Physics and Chemistry of Solids, 2020. **142**: p. 109462.
46. Bharathy, G. and P. Raji, *Room temperature ferromagnetic behavior of Mn doped NiO nanoparticles: a suitable electrode material for supercapacitors.* Journal of Materials Science: Materials in Electronics, 2017. **28**(23): p. 17889-17895.
47. Abul-Magd, A.A., H. Morshidy, and A. Abdel-Ghany, *The role of NiO on the structural and optical properties of sodium zinc borate glasses.* Optical Materials, 2020. **109**: p. 110301.
48. WebElements, *Nickel oxide.* May 2021.
49. Saraç, B.E., *Structural and optoelectronic properties of sol-gel derived nickel oxide thin films*. 2017, MIDDLE EAST TECHNICAL UNIVERSITY.
50. Menaka, S.M., G. Umadevi, and M. Manickam, *Effect of copper concentration on the physical properties of copper doped NiO thin films deposited by spray pyrolysis.* Materials Chemistry and Physics, 2017. **191**: p. 181-187.
51. Van Houten, S., *Semiconduction in LixNi1− xO.* Journal of Physics and Chemistry of Solids, 1960. **17**(1-2): p. 7-17.
52. Mora-Gomez, J., et al., *Electrochemical degradation of norfloxacin using BDD and new Sb-doped SnO2 ceramic anodes in an electrochemical reactor in the presence and absence of a cation-exchange membrane.* Separation and Purification Technology, 2019. **208**: p. 68-75.
53. Mounkachi, O., et al., *Band-gap engineering of SnO2.* Solar Energy Materials and Solar Cells, 2016. **148**: p. 34-38.
54. Zhang, M., et al., *SnO2 epitaxial films with varying thickness on c-sapphire: structure evolution and optical band gap modulation.* Applied Surface Science, 2017. **423**: p. 611-618.
55. Yu, H., et al., *pN heterostructural sensor with SnO-SnO2 for fast NO2 sensing response properties at room temperature.* Sensors and Actuators B: Chemical, 2018. **258**: p. 517-526.
56. Lagha-Menouer, K., *Etude et réalisation d’une cellule solaire multicouches du type Si-SiO2-SnO2-ZnO par APCVD.* Université mouloud mammeri de tizi-ouzou, 2011.
57. Bouras, K., *Re-doped SnO2 oxides for efficient UV-Vis to infrared photon conversion: application to solar cells*. 2016, Strasbourg.
58. Lu, Y., *SnO2 Thin Films-Chemical Vapor Deposition and Characterization*. 2015: Verlag nicht ermittelbar.
59. Ynineb, F., et al., *Influence of Sn content on properties of ZnO: SnO2 thin films deposited by ultrasonic spray pyrolysis.* Materials science in semiconductor processing, 2013. **16**(6): p. 2021-2027.

60. Saadeddin, I., *Préparation et caractérisation des nouvelles électrodes transparentes à base de SnO2 (indice) et In2 (indice) O3 (indice): sous forme de céramiques et couches minces*. 2007, Université Sciences et Technologies-Bordeaux I.

61. Aoun, Y., et al., *Effect of deposition rate on the structural, optical and electrical properties of Zinc oxide (ZnO) thin films prepared by spray pyrolysis technique.* Optik, 2015. **126**(20): p. 2481-2484.

62. Aoun, Y., et al., *Preparation and characterizations of monocrystalline Na doped NiO thin films.* Materials Research, 2018. **21**(2).

63. Qiu, P., et al., *Plasma-enhanced atomic layer deposition of gallium nitride thin films on fluorine-doped tin oxide glass substrate for future photovoltaic application.* Ceramics International, 2020. **46**(5): p. 5765-5772.

64. Benramache, S., et al., *Transition width effect on optical characterizations of ZnO thin films deposited by spray ultrasonic.* Inorganic and Nano-Metal Chemistry, 2019. **49**(6): p. 177-181.

65. Benramache, S., et al., *The calculate of optical gap energy and urbach energy of Ni 1− x Co x O thin films.* Sādhanā, 2019. **44**(1): p. 26.

66. Benramache, S. and Y. Aoun, *Spin Coating Method Fabricated of In 2 O 3 Thin Films.* Annals of the West University of Timisoara. Physics Series, 2019. **61**: p. 56-63.

67. Al Farsi, B., et al., *Structural and optical properties of visible active photocatalytic Al doped ZnO nanostructured thin films prepared by dip coating.* Optical Materials, 2021. **113**: p. 110868.

68. Vu, T.D., et al., *Physical vapour deposition of vanadium dioxide for thermochromic smart window applications.* Journal of Materials Chemistry C, 2019. **7**(8): p. 2121-2145.

69. Mostafa, A.M. and A. Menazea, *Laser-assisted for preparation ZnO/CdO thin film prepared by pulsed laser deposition for catalytic degradation.* Radiation Physics and Chemistry, 2020. **176**: p. 109020.

70. Nikiforov, A., et al., *Formation of SnO and SnO2 phases during the annealing of SnO (x) films obtained by molecular beam epitaxy.* Applied Surface Science, 2020. **512**: p. 145735.

71. Gonçalves, R., et al., *The effect of thickness on optical, structural and growth mechanism of ZnO thin film prepared by magnetron sputtering.* Thin Solid Films, 2018. **661**: p. 40-45.

72. Shi, F., *Introductory Chapter: Basic Theory of Magnetron Sputtering*, in *Magnetron Sputtering*. 2018, IntechOpen.

73. Pellicori, S., *Choosing between thermal evaporation and sputter deposition.* Coating Mater. News, 2000. **10**(3).

74. Baptista, A., et al., *Sputtering physical vapour deposition (PVD) coatings: A critical review on process improvement and market trend demands.* Coatings, 2018. **8**(11): p. 402.

75. Vladoiu, R., et al., *Thermionic Vacuum Arc—A versatile technology for thin film deposition and its applications.* Coatings, 2020. **10**(3): p. 211.

76. Maury, F., *Recent trends in the selection of metal-organic precursors for MOCVD process.* Le Journal de Physique IV, 1995. **5**(C5): p. C5-449-C5-463.

77. OTHMANE, M., *Synthesis and characterization of Zinc Oxide (ZnO) Thin films deposited by spray pyrolysis for applying: electronics and photonics*. 2018, UNIVERSITE MOHAMED KHIDER BISKRA.

78. Zhong, B., et al., *Fabrication of novel hydrophobic SiC/SiO2 bead-string like core-shell nanochains via a facile catalyst/template-free thermal chemical vapor deposition process.* Materials Chemistry and Physics, 2018. **217**: p. 111-116.

79. May, P., et al., *CVD diamond-coated fibres.* Diamond and related materials, 1995. **4**(5-6): p. 794-797.

80. Naslain, R. and F. Langlais, *CVD-processing of ceramic-ceramic composite materials*, in *Tailoring multiphase and composite ceramics*. 1986, Springer. p. 145-164.

81. Chen, C., et al., *Achieving high performance corrosion and wear resistant epoxy coatings via incorporation of noncovalent functionalized graphene.* Carbon, 2017. **114**: p. 356-366.

82. Sun, Y., et al., *Research on the mechanism of micromachining of CVD diamond by femtosecond laser.* Ferroelectrics, 2019. **549**(1): p. 266-275.

83. Franssila, S., *Introduction to microfabrication*. 2010: John Wiley & Sons.

84. Perednis, D. and L.J. Gauckler, *Thin film deposition using spray pyrolysis.* Journal of electroceramics, 2005. **14**(2): p. 103-111.

85. Hui, R., et al., *Deposition, characterization and performance evaluation of ceramic coatings on metallic substrates for supercritical water-cooled reactors.* Surface and Coatings Technology, 2011. **205**(11): p. 3512-3519.

86. Messing, G.L., S.C. Zhang, and G.V. Jayanthi, *Ceramic powder synthesis by spray pyrolysis.* Journal of the American Ceramic Society, 1993. **76**(11): p. 2707-2726.

87. Sutka, A., et al., *Ethanol monitoring by ZnFe2O4 thin film obtained by spray pyrolysis.* Sensors and Actuators B: Chemical, 2013. **176**: p. 330-334.

88. Ukoba, K.O. and F.L. Inambao. *Deposition of Nanostructured TiO 2/NiO Heterojunction Solar Cells Using Spray Pyrolysis*. in *The World Congress on Engineering and Computer Science*. 2018. Springer.

89. Filipovic, L., et al., *A method for simulating spray pyrolysis deposition in the level set framework.* Eng. Lett, 2013. **21**(4): p. 224-240.

90. Mezhericher, M., et al., *Aerosol-assisted synthesis of submicron particles at room temperature using ultra-fine liquid atomization.* Chemical Engineering Journal, 2018. **346**: p. 606-620.

91. Ghan, S.J., C.C. Chung, and J.E. Penner, *A parameterization of cloud droplet nucleation part I: single aerosol type.* Atmospheric Research, 1993. **30**(4): p. 198-221.

92. Wang, W.-N., et al., *Investigation on the correlations between droplet and particle size distribution in ultrasonic spray pyrolysis.* Industrial & Engineering Chemistry Research, 2008. **47**(5): p. 1650-1659.

93. Misyura, S., *Contact angle and droplet evaporation on the smooth and structured wall surface in a wide range of droplet diameters.* Applied Thermal Engineering, 2017. **113**: p. 472-480.

94. Eckert, M., *Max von Laue and the discovery of X-ray diffraction in 1912*. 2012, WILEY-VCH Verlag Berlin.

95. Kraniotis, G. and S. Whitehouse, *Compact calculation of the perihelion precession of Mercury in general relativity, the cosmological constant and Jacobi's inversion problem.* Classical and Quantum Gravity, 2003. **20**(22): p. 4817.

96. Stelzried, C., R. Clauss, and S. Petty, *Deep Space Network Receiving Systems' Operating Noise Temperature Measurements.* The Interplanetary Network Progress Report 42-154, April–June 2003, 2003: p. 1-7.

97. Eby, G.N., 2004, Principles of Environmental Geochemistry. Brooks/Cole-Thomson Learning, p. 212-214.

98. Saravanakannan, V. and T. Radhakrishnan, *Structural, electrical and optical characterization of CuO thin films prepared by spray pyrolysis technique.* International Journal of ChemTech Research, 2014. **6**(1): p. 306-310.

99. Rahdar, A., M. Aliahmad, and Y. Azizi, *NiO nanoparticles: synthesis and characterization.* 2015.

100. Räty, J.A., K.-E. Peiponen, and T. Asakura, *UV-visible reflection spectroscopy of liquids*. Vol. 92. 2004: Springer Science & Business Media.

101. Thomas, O. and C. Burgess, *UV-visible Spectrophotometry of Water and Wastewater*. 2017: Elsevier.

102. Boubaker, K., *A physical explanation to the controversial Urbach tailing universality.* The European Physical Journal Plus, 2011. **126**(1): p. 10.

103. Choudhury, B., B. Borah, and A. Choudhury, *Extending photocatalytic activity of TiO2 nanoparticles to visible region of illumination by doping of cerium.* Photochemistry and photobiology, 2012. **88**(2): p. 257-264.

104. Hasegawa, S. and F. Grey, *Electronic transport at semiconductor surfaces—from point-contact transistor to micro-four-point probes.* Surface Science, 2002. **500**(1-3): p. 84-104.

105. Islam, M.R., et al., *Structural, optical and photocatalysis properties of sol–gel deposited Al-doped ZnO thin films.* Surfaces and Interfaces, 2019. **16**: p. 120-126.

106. Santos, Y., et al., *A novel structure ZnO-Fe-ZnO thin film memristor.* Materials Science in Semiconductor Processing, 2018. **86**: p. 43-48.

107. Benramache, S., et al., *Elaboration and characterisation of ZnO thin films.* Matériaux & Techniques, 2012. **100**(6-7): p. 573-580.

108. Diha, A., S. Benramache, and L. Fellah, *The crystalline structure, optical and conductivity properties of fluorine doped ZnO nanoparticles.* 2019.

109. Varughese, G., et al., *Characterisation and optical studies of copper oxide nanostructures doped with lanthanum ions.* Advances in materials science, 2014. **14**(4): p. 49.

110. Kate, R.S., S.C. Bulakhe, and R.J. Deokate, *Effect of substrate temperature on properties of nickel oxide (NiO) thin films by spray pyrolysis.* Journal of Electronic Materials, 2019. **48**(5): p. 3220-3228.

111. Panneerselvam, V., et al., *Role of copper/vanadium on the optoelectronic properties of reactive RF magnetron sputtered NiO thin films.* Applied Nanoscience, 2018. **8**(6): p. 1299-1312.

112. Ismail, R.A., S.a. Ghafori, and G.A. Kadhim, *Preparation and characterization of nanostructured nickel oxide thin films by spray pyrolysis.* Applied Nanoscience, 2013. **3**(6): p. 509-514.

113. Shkir, M., et al., *Structural, morphological, vibrational, optical, and nonlinear characteristics of spray pyrolyzed CdS thin films: Effect of Gd doping content.* Materials Chemistry and Physics, 2020. **255**: p. 123615.

114. Benramache, S., H. Guezzoun, and B. Benhaoua, *Synthesis and characterizations of nanocrystalline Na and Al codoped NiO thin films.* International Journal of Integrated Engineering, 2020. **12**(1): p. 204-209.

115. Khalfallah, B., I. Riahi, and F. Chaabouni, *Effect of Cu doping on the structural, optical and electrical properties of ZnO thin films grown by RF magnetron sputtering: application to solar photocatalysis.* Optical and Quantum Electronics, 2021. **53**(5): p. 1-14.

116. Mahmoud, S.A., A. Shereen, and A.T. Mou'ad, *Structural and optical dispersion characterisation of sprayed nickel oxide thin films.* Journal of Modern Physics, 2011. **2011**.

117. Manouchehri, I., et al., *Optical properties of zinc doped NiO thin films deposited by RF magnetron sputtering.* Optik, 2016. **127**(20): p. 9400-9406.

118. Nakate, U.T., et al., *Ultrathin ternary metal oxide Bi2MoO6 nanosheets for high performance asymmetric supercapacitor and gas sensor applications.* Applied Surface Science, 2021. **551**: p. 149422.

119. Salunkhe, P., M.A. AV, and D. Kekuda, *Investigation on tailoring physical properties of Nickel Oxide thin films grown by dc magnetron sputtering.* Materials Research Express, 2020. **7**(1): p. 016427.